

**Analysis and Algorithms for Parametrization,  
Optimization and Customization of Sled Hockey  
Equipment and Other Dynamical Systems**

by

Youzhi Liang

Submitted to the Department of Mechanical Engineering  
in partial fulfillment of the requirements for the degree of

Doctor of Philosophy in Mechanical Engineering

at the

MASSACHUSETTS INSTITUTE OF TECHNOLOGY

February 2020

© Massachusetts Institute of Technology 2020. All rights reserved.

**Signature redacted**

Author .....

Department of Mechanical Engineering

November 15, 2019

**Signature redacted**

Certified by .....

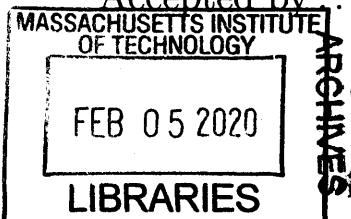
A.E. Hosoi

Professor/Associate Dean of Engineering

Thesis Supervisor

**Signature redacted**

Accepted by .....



Nicolas Hadjiconstantinou

Chairman, Department Committee on Graduate Thesis



77 Massachusetts Avenue  
Cambridge, MA 02139  
<http://libraries.mit.edu/ask>

## **DISCLAIMER NOTICE**

Due to the condition of the original material, there are unavoidable flaws in this reproduction. We have made every effort possible to provide you with the best copy available.

Thank you.

**The images contained in this document are of the best quality available.**



# Analysis and Algorithms for Parametrization, Optimization and Customization of Sled Hockey Equipment and Other Dynamical Systems

by

Youzhi Liang

Submitted to the Department of Mechanical Engineering  
on November 15, 2019, in partial fulfillment of the  
requirements for the degree of  
Doctor of Philosophy in Mechanical Engineering

## Abstract

A dynamical system, an ensemble of particles, states of which evolve over time, can be described using a system of ordinary/partial differential equations (ODEs/PDEs). This dissertation presents fundamental investigations of the analysis and algorithms for the study of dynamical systems, by parametrizing, optimizing and customizing. We develop and/or implement numerical algorithms, for solving ODEs/PDEs, and statistical/machine-learning algorithms based on data, for physical inference and prediction. We further apply the methodologies on sled hockey, an adaptation of stand-up hockey, allows people with physical disabilities to participate in the game of ice hockey.

First, we develop and implement numerical algorithms to study the nonlinear dynamics described by 4th-order nonlinear PDEs. The non-linear solvers apply multi-dimensional Newton's method with a Jacobian-free approach and a generalized conjugate residual (GCR) approach. Applying the algorithms on the study of elastic systems, we investigate dynamics of hockey sticks as in a striking implement. We develop a mathematical model using an Euler-Lagrange equation to characterize the behavior of a hockey stick in the linear regime, and then apply this model to investigate the dynamic response of the stick throughout slap shots and wrist shots. We apply a modal decomposition method and decouple the resultant dynamics into kinetic and potential components. We further optimize the structures based on the dynamical analysis. Throughout testing with both elite and amateur sled hockey players, we find that final puck velocities with our prototype stick are on average over 10% higher compared to those achieved with commercially available sticks.

Second, we investigate the dynamics of rigid system as in an over-constrained implement. We propose two sets of dynamical modelling for the hockey sled using a trajectory-based modelling method and a state-space-based modelling method, which are used to study the dynamics of the propulsion for linear motion and of the tip-over and reset. We further propose a constrained optimization problem to optimize the

parameters of sled design and driving strategy to maximize the performance of sled hockey players based on the dynamics.

Third, we develop and implement statistical and machine learning algorithms based on data, including algorithms of clustering for physical inference, algorithms of regression for Stribeck curve and algorithms of forecasting for wear rate. In the context of tribology of ice-metal contact, we design an experimental system to mimic the ice rink environment and to expand the experimental study of the friction coefficient in an extensive range of Hersey number from  $10^{-13}$  to  $10^{-4}$ . To build the understanding of the physics of friction, we perform a dimensional analysis and an asymptotic analysis for three regimes of friction - boundary friction regime, mixed friction regime, and hydrodynamic lubrication regime. We further develop a pipeline for creating the modified Stribeck curve based on data, after feature extraction, the regime of each experimental result is identified via clustering, followed by the regression constrained by the asymptotic analysis. Finally, we propose a methodology and algorithm to predict the wear rate subject to geometric constraints.

Thesis Supervisor: A.E. Hosoi

Title: Professor/Associate Dean of Engineering

# Acknowledgments

I would like to express my greatest appreciation to my adviser, Professor Peko Hosoi, for her invaluable guidance, mentorship and inspiration, throughout my PhD program over the past four years. This dissertation has benefited greatly by her profound knowledge, in the areas of, amongst many others, structural dynamics, fluid dynamics, sports technology, algorithms and data science.

I thank my thesis committee members for their insightful feedback and guidance. I thank Professor Winter for his expertise on design for highly constrained environments, machine and product design, and engineering global development; I thank Professor Yang for her expertise on system-level design for complex engineering systems, early stage design process for products and systems, and design representation, including visual, physical and linguistic. Their advice and suggestions are extremely helpful and valuable for me.

I thank Mr. and Mrs. Greenberg for providing me with the opportunity of this research. I thank Wheelchair Sports Federation (WSF) New York Sled Rangers for their support on the surveys, interviews, experiments and insightful feedback for my research. WSF New York Sled Rangers are the Wheelchair Sports Federation New York Sled Rangers, serving as a sled hockey program for physically disabled youth with ages from five through twenty-one. They are one of the very few outlets for physically disabled kids to play competitive sports in New York City.

I thank Jordan Malone, a member of US Olympic Team for the 2010 Olympics, achieving numerous World titles including 2009 Men's Relay GOLD, for his insight of speed skating and design of skate blades and for his feedback on our study of the physics of ice friction.

I thank Josh and Max for the collaboration on the investigation of slap shots in sled hockey, especially for the co-authorship on the relevant publication. Thank Sarah for the collaboration on the investigation of wrist shots and for the co-authorship on the relevant publication. Thank Andrew for the collaboration on the development of numerical solvers for the dynamics of the Euler-Bernoulli beam and the relevant

publication. Thank Jose for the collaboration on the study of magnetorheological fluids and the relevant publication. Thank Bavand for his insightful input on the study of the friction coefficient between skate blades and ice and the relevant publication. I thank Yuanzheng, Kanghong, Zeyu and Jennifer for their review and feedback on this dissertation.

I thank all my teammates and alumni in Team Peko. The culture of Team Peko is dynamic, collaborative and inclusive. I thank Jose, Josh, Ben, Nathan, Alice, Jennifer, Juncal, Jean, Sarah, Kaitlyn, Audrey, Charlotte, Will and all the teammates and alumni not listed here. I thank Jose for his guidance on my study of fluid mechanics; I thank Kaitlyn for her help on the analysis of partial differential equations; I thank Nathan for his help on the electronics and control theory; I thank Josh and Ben for their help on the study of dynamics of systems; I thank Juncal for her help on the optimization methods. In particular, I thank Susan for always helping me out when I was in need.

I thank all the HML professors and labmates. The Hatsopoulos Microfluids laboratory (HML) focuses on the research on the dynamics of microstructures and microfluidics, consisting of a single open-plan 6300 ft<sup>2</sup> laboratory. The configuration of the lab encourages collaboration between students with diverse backgrounds and expertise. During my MS and PhD program, I've received much help and support from the professors and labmates. I thank Professor McKinley for his expertise on extensional rheology of complex fluids and Non-Newtonian fluid dynamics; I thank Professor Bischofberger for her expertise on pattern formation and soft condensed matter. I thank Anoop and Jianyi for their instruction on the rheology measurement and the corresponding customized devices. I thank Sean and Cakky for their service on the lab.

I thank my friends Yuanzheng, Kanghong, Hongyi, Qing, Jianyi. They are extremely important to me. I very much value our friendship. I thank my friends for all their support and care for me. I thank Zhi, Shurui, Yongbin and Xiaoyu, Akira and Wenjun, Affi, Avani, Anthea, Borrelli, Liz, Shayan, Adam, Morgan, Sri, Tianshi, Xi-angming, Yulin, Dixia, Dayang, Yu, Bo, Yingyi, Ming, Shawn, Yili, Qingjun, Qifang,

Lei, Leixin, Lin, Chu, Haizheng, Quntao, Xiang, Wolski, Urmi, Morgan, Rachel, Ben, Caitlin, Thanasi, Jonathan, Sang, JiuHong, Jianping, Jiheng, Lu and all the other friends not mentioned here.

I thank my parents and other relatives for their love, sacrifice and understanding, on the other side of the earth, for which I am forever grateful and more than I could ever hope to repay.





# Contents

<b>1</b>	<b>Introduction</b>	<b>29</b>
1.1	What is Parametrization, Optimization and Customization . . . . .	29
1.2	What is Dynamical System . . . . .	30
1.3	Scope of Study . . . . .	31
1.3.1	Scope Identification . . . . .	32
1.3.2	Outline of the Dissertation . . . . .	35
<b>2</b>	<b>Algorithms of Numerical Methods for Non-Linear PDEs</b>	<b>41</b>
2.1	Background and Introduction . . . . .	41
2.2	Algorithms of Numerical Methods . . . . .	42
2.2.1	Algorithms of Numerical Solvers for Linear PDEs . . . . .	43
2.2.2	Algorithms for Numerical Solvers for Non-Linear PDEs . . . . .	47
2.2.3	Algorithms for Reduced-Order Methods . . . . .	49
2.3	Experiments, Results and Discussion . . . . .	52
<b>3</b>	<b>Dynamics of Elastic Systems - Slap Shots</b>	<b>57</b>
3.1	What is Slap Shot . . . . .	58
3.2	Dynamical Modelling and Parametric Optimization . . . . .	60
3.2.1	Continuous Euler-Bernoulli Beam Model . . . . .	60
3.2.2	Discrete Mass-Spring-Damper Model . . . . .	68
3.3	Conclusion and Future Work . . . . .	70
<b>4</b>	<b>Dynamics of Elastic Systems - Wrist Shots</b>	<b>73</b>

4.1	What is Wrist Shot . . . . .	74
4.2	Dynamical Modelling and Parametric Optimization . . . . .	75
4.3	Experiments, Results and Discussion . . . . .	79
4.4	Conclusion and Future Work . . . . .	83
<b>5</b>	<b>Dynamics of Rigid Systems</b>	<b>85</b>
5.1	Dynamical Modelling of Hockey Sled . . . . .	86
5.1.1	Method 1: Trajectory-Based Modelling . . . . .	86
5.1.2	Method 2: State-Space-Based Modelling . . . . .	93
5.2	Propulsion for Linear Motion . . . . .	97
5.2.1	Kinematics and Dynamics of Propulsion . . . . .	97
5.2.2	Parametric Optimization . . . . .	102
5.3	Tip-Over and Reset . . . . .	104
5.3.1	Dynamical Modelling of Tip-Over and Reset . . . . .	104
5.3.2	Parametric Optimization . . . . .	106
<b>6</b>	<b>Tribology in Ice-Metal Contact</b>	<b>111</b>
6.1	Background and Introduction . . . . .	112
6.1.1	What is Tribology in Ice Friction . . . . .	112
6.1.2	Stribeck Curve . . . . .	114
6.1.3	Kinetic Friction of Ice . . . . .	115
6.2	Dimensional Analysis . . . . .	117
6.3	Experimental System . . . . .	118
6.4	Asymptotic Analysis . . . . .	120
6.4.1	Asymptotic Analysis for Elastohydrodynamic Contacts . . . . .	120
6.4.2	Asymptotic Analysis for Mixed Contacts . . . . .	121
6.4.3	Asymptotic Analysis for Boundary Contacts . . . . .	122
6.5	Modified Stribeck Curve for Friction Coefficient . . . . .	125
<b>7</b>	<b>Algorithms of Clustering for Physical Inference in Tribology</b>	<b>127</b>
7.1	Feature Extraction and Feature Selection . . . . .	127

7.2	Algorithms for Clustering Model . . . . .	129
7.2.1	K-Means Clustering . . . . .	129
7.2.2	Gaussian Mixture Clustering . . . . .	130
7.3	Clustering for Physical Inference in Tribology . . . . .	131
<b>8</b>	<b>Algorithms of Regression for Stribeck Curve in Tribology</b>	<b>133</b>
8.1	Background and Introduction . . . . .	133
8.2	Algorithms for Statistical Model . . . . .	134
8.2.1	Multi-Linear Regression . . . . .	134
8.3	Algorithms for Machine Learning Model . . . . .	137
8.3.1	Random Forest Regression . . . . .	137
8.3.2	Neural Network Regression . . . . .	142
8.4	Regression for Stribeck Curve . . . . .	143
<b>A</b>	<b>Approval Letters from the MIT Committee on the Use of Humans as Experimental Subjects (COUHES)</b>	<b>147</b>
<b>B</b>	<b>Figures for Experimental Results in the Regime of Boundary Fric- tion</b>	<b>151</b>
<b>C</b>	<b>Figures for Experimental Results and Models in the Regime of Mixed Friction and Hydrodynamic Lubrication</b>	<b>153</b>



# List of Figures

1-1	Survey results with 27 subjects, among which ten subjects are players, ten are parents, four are coaches and three are others. This survey is conducted to identify the stakeholder’s needs and their priorities. (Inset) Results only for coaches. . . . .	34
1-2	Quality Function Deployment (QFD) analysis for the sled hockey project. The customer requirements and technical requirements serve as the attributes and design parameters in QFD analysis, respectively. According to the results from the interview and survey, we consider eight attributes and ten design parameters. The attributes are prioritized from 1 (top priority) to 8 (bottom priority), based on the evaluation results for the relationships between the customer requirements and technical requirements. . . . .	36
2-1	(a) Cantilevered Euler-Bernoulli beam fixed at (0,0) with a Gaussian distributive load as function of space and time, $f(x, t) = G_1(x)G_2(t)$ . We select the diamond point as the output point for the deflection of the beam. (b) Deflection of the loaded beam under external load as a function of space and time. . . . .	42
2-2	Transverse deflection of the beam in the form of discrete representation. (a) Free body diagram of each discrete element; (b) Discrete representation of a beam with $N$ nodes. . . . .	43

2-3	Deflection $y$ (m) as a function of position $x$ (m) for time $t = 0.1$ ms, $t = 5$ ms, $t = 250$ ms. The external load is a Gaussian distributive force in space, of which the center is located at $x = 0.4$ m. Trapezoidal integration method with a dynamically adjusted time step is applied.	44
2-4	Deflection at the center of the beam as a function of position $x$ (m) subject to an impulse input force. The impulse force is modelled as a Gaussian distributive force with respect to time. The internal friction term in Eqn. 2.1 is taken into account in this simulation. . . . .	46
2-5	Deflection of a sled hockey stick under external load. (a) FEA simulation results using Solidworks with 289,959 DOF; (b) Simulation results using our 1D model. . . . .	46
2-6	Transverse deflection $y$ (m) of the beam as a function of the position $x$ (m) for the beam equation with/without the non-linear term. (a) Beam subject to a uniform distributed load. The external force $b(x)$ is a constant. (b) Beam subject to a Gaussian distributed load. The external force $b(x)$ is centered at $x = 0.1$ . . . . .	48
2-7	Comparison of Bode plots of the transfer functions, using original system $N = 500$ and using reduced system with $q = 2$ and $10$ respectively (from left to right). The phase diagram appears to be shifted by $360$ at some frequencies due to the plot setting using MATLAB by default.	51
2-8	Comparison of deflections of a sinusoidal response of the Euler-Bernoulli beam as a function of time, using original system $N = 500$ and using reduced system with $q = 2$ and $10$ respectively (from left to right). .	51
2-9	(a) Bode plot for the original system and reduced system using moment matching method. (b) Impulse response for original system and reduced system. . . . .	52

2-10	Histograms of the puck velocity for the rigid and flexible sled hockey sticks. Each histogram bar is normalized by the total number data points. (Inset) Percentage increase in puck velocity for each subject when using the flexible sled hockey stick. The dashed line indicates the average increase, 13.07 %. Subjects are shown in order of ascending percentage increase. . . . .	54
2-11	Puck velocity versus measured stick force for each subject. Linear curves of best fit are shown as solid lines. The puck velocity for each point corresponds to the mean value across three trials, and the peak force for each players corresponds to the mean of five measurements. .	56
3-1	(a) Schematic of a stand-up hockey slap shot. (b) Schematic of a sled hockey slap shot using our prototype sled hockey stick. The flexibility is increased by using ABS plastic in place of wood. (c) Photograph of a sled hockey player using the conventional wooden sled hockey stick [1]. (Photograph credit John Freidah) The puck is highlighted in green. <i>i</i> : Backswing/Downswing; <i>ii</i> : Stick preload; <i>iii</i> : Puck impact; <i>iv</i> : Puck release. . . . .	59
3-2	Schematic of our Euler-Bernoulli beam model of a sled hockey slap shot. (a) Stick preload; (b) Puck impact; (c) Puck release. . . . .	60
3-3	(a) $\beta$ plotted as a function of the Young's modulus of the beam material, $E$ . (Inset) The contribution of the first five mode shapes to the net value of $\beta$ . (b) Puck velocity $V_p$ plotted as a function of the Young's modulus of the beam material. Solid and dash-dot lines correspond to the continuous and discrete models respectively. The colored dashed and dotted lines plot the contributions of the elastic and kinetic energy to the overall puck velocity ( $V_{pot}$ and $V_{kin}$ respectively). The shaded area highlights conditions where the stick deflection is large and our linear model may not be valid. . . . .	64



- 3-4 (a) We compare the predicted puck speed,  $V_p$  (m/s) of our model with experimental data on stand-up slapshots over a range of stick stiffness values. Data is sourced from [2]. Within the the experimental data, the loading force varies significantly between shots. The shaded region corresponds to predicted puck speeds  $V_p$  for the range of forces observed in [2]. (Inset)  $V_{kin}$  (m/s) plotted as a function of the stiffness (N/m).  $V_{kin}$  is calculated by removing  $V_{pot}$  from both the model and experimental puck velocities. (b) Time  $t$  (s) to perform a slap shot as a function of the puck speed  $V_p$  (m/s). Arrows indicate directions of decreasing Young's modulus  $E$ . The diamond markers delineate the optimal conditions labelled with the corresponding optimal Young's modulus  $E$ . . . . . 65
- 3-5 The ratio of the optimal Young's modulus of the stick material to the available Young's modulus,  $E_{opt}/E_{avail}$  for sled hockey sticks (a) and for stand-up hockey sticks (b). The color map is in logarithmic scale. The ranges of the peak force  $F_0$  for sled hockey and stand-up hockey are 15 N to 60 N and 230 N to 400 N respectively [2]; the ranges of the angular speed  $\omega_L$  are 4.5 rad/s to 9 rad/s and 8.5 rad/s to 13 rad/s respectively [3]. . . . . 67
- 3-6 The ratio of the optimal Young's modulus of the stick material to the available Young's modulus,  $E_{opt}/E_{avail}$  for sled hockey sticks (a) and for stand-up hockey sticks (b). The color map is in logarithmic scale. The ranges of peak force  $F_0$  for the sled hockey and stand-up hockey are 15 N to 60 N and 230 N to 400 N respectively [2]; the ranges of the angular speed  $\omega_L$  are 4.5 rad/s to 9 rad/s and 8.5 rad/s to 13 rad/s respectively [3]. . . . . 68
- 3-7 (a) Discrete model. (b) Experimental setup. (c) Discrete model for three stages of a slap shot.  $dy_p/dt$  at  $t = t_c^-$  and  $t = t_c^+$  are denoted as  $v_0$  and  $v_1$  respectively;  $dy_s/dt$  at  $t = t_c^-$  and  $t = t_c^+$  as  $u_0$  and  $u_1$  respectively. . . . . 69

3-8 Comparison of theoretical and experimental mass displacements for our discrete collision model. (Inset) Theoretical results for the case of zero energy loss. . . . . 71

4-1 Schematic of the Euler-Bernoulli beam model for a sled hockey stick and a rigid body model for a puck.(a) Preload stage; (b) Release; (c) Post-Release stage. . . . . 75

4-2 Modal decomposition of initial deflection of the beam under static load. The first five eigenmodes are included in the figure. (Inset) Mode shapes of the first five eigen modes. . . . . 78

4-3 The magnitude of the puck velocity and the flexural rigidity as a function of Young’s modulus of the material of the beam respectively. . . 79

4-4 (a) Prototype of a more flexible sled hoceky stick; (b) A commercially-available sled hockey stick. . . . . 80

4-5 Histograms for the magnitude of the velocity of the puck using two types of sled hockey sticks. The histogram is normalized by the discrete probability density function (PDF). (Inset) The increase in percentage of the magnitude of the puck velocity in ascendant order for each individual subject using flexible sled hockey sticks compared to that using rigid sticks. The dashed line indicates the average increase which is 11.48%. . . . . 81

4-6 The magnitude of the puck velocity versus the peak force that players can exert with two lines indicating the linear regressions using the two types of sled hockey sticks respectively. . . . . 83

5-1 Schematic of the frames and the trajectories for the motion of hockey sled. Point A is the contact point between the skate blade and ice surface.  $S_A$  is the trajectory of A.  $S_{COC}$  is the trajectory of the center of curvature of  $S_A$ .  $X_I Y_I Z_I$  is the inertial frame. Frame  $xyz$  is fixed on the sled along the principal axis of the sled, of which the coordinates  $y$  and  $z$  locate in plane  $P_2$  and coordinate  $x$  in  $P_1$ . Frame  $XYZ$  is an intermediate frame, of which the coordinate  $y$  directs towards point A.  $P_1$  and  $P_2$  are virtual planes which are parallel and perpendicular to the curve  $S_A$  respectively. . . . . 88

5-2 Schematic of the back view of hockey sled and free body diagram.  $N_1$  is the normal reaction force for the foot support of the hockey sled. Point A is the contact point between one hockey blade and the ice surface.  $N_2$  is the normal reaction force for skate blades at point A.  $b_x'$  and  $b_x$  are distances between the center of mass and the foot support of the sled and point A respectively.  $F_{||}$  is the frictional force acted on the skate blade.  $P_2$  is the virtual plane as shown in Fig. 5-1, which is parallel to the trajectory of A. . . . . 89

5-3 Schematic of the back view of hockey sled and free body diagram. Point A is the contact point between one hockey skate blade and the ice surface.  $\theta(t)$  is the lean angle of the sled,  $N_2$  is the normal reaction force for the foot support and skate blade respectively.  $F_{\perp}$  is the frictional reaction force between ice and the skate blade at point A.  $H_c$ ,  $H_b$  and  $b_y$  are dimensions of the hockey sled with respect to the center of mass. 89

5-4 Schematic of the back view of hockey sled and free body diagram.  $L_1$  is the length of the player’s upper arm,  $L_2$  is the length of the player’s forearm,  $L_3$  is the effective length of the hockey stick, i.e. the distance from the position where a player holds the stick to the end of the stick,  $L_s$  is the distance from the ground to the bottom of the sled bucket, and  $L_p$  is the distance from the bottom of the bucket to the player’s shoulder. Point P is the contact point between a hockey stick and the ice surface. . . . . 98

5-5 Experimental results for  $\alpha(t) - \alpha_0$  as a function of time  $t$ .  $\alpha_0$  is the initial angle at time  $t_0$  between the hockey stick and the forearm. A parabolic model, indicated in the dashed line, was fit for the experimental results compared with our hypothesis model. . . . . 99

5-6 Simulation results for the ratio of  $F_M/F_0$  as a function of  $\dot{\Phi}(T)/\dot{\Phi}_0$ . The coefficient of shortening heat  $a_{min} = 0.2F_0$ ,  $a_{max} = 0.3F_0$  and  $a = 0.48F_0$  are illustrated in the figure. . . . . 99

5-7 Simulation results of the angular velocity  $\dot{\Phi}_1$ ,  $\dot{\Phi}_2$ ,  $\dot{\Phi}_3$  and  $V$  for a non-optimal condition and an optimal condition. The  $T_1$  and  $T_2$  cycle indicate the non-optimal and optimal condition, respectively. . . . . 101

5-8 Simulation results for the upper arm (blue), the forearm (blue) and hockey stick (brown) during the first cycle of propulsion. At  $t_0$ , the hockey player places arms and the hockey stick at the optimal position. At  $t_{end}$ , the first propulsion ends due to the violation of at least one of the constraints. During this first cycle, the player attempts his/her best effort which is governed by the muscle’s Hill model. . . . . 101

5-9 Simulation results for the dimensionless average velocity  $V$  during the first cycle of propulsion for  $\Phi_s$  ranging from 0 rad to 1.5 rad and  $\Phi_{2s}$  ranging from -0.5 rad to 1.5 rad. The upper-left white triangle area indicates no results from simulation due to the constraint  $\Phi_{1s} > \Phi_{2s}$ . . . . . 103

5-10	Minimum required force $F_{req}^{min}$ to reset after a tip-over occurs and stable range $\theta^*$ as a function of $\gamma_{yw}$ and $\gamma_{hw}$ . $\gamma_{yw}$ and $\gamma_{hw}$ both range from 0.01 to 0.5. . . . .	106
5-11	Maximum and minimum of the required force for reset as a function of the lean angle $\theta$ for $\gamma_{yw} = \gamma_{hw} = 0.5$ and $\gamma_{yw} = \gamma_{hw} = 1$ . $ \Delta_{min} $ represents the minimum range of the required force during the process of reset. . . . .	109
5-12	Effective ranges of required force for parameters of hockey sled, for $\gamma_{yw}$ and $\gamma_{hw}$ both ranging from 0.05 to 0.5. The stable range $\theta^*$ is overlaid. The grey area indicates the stable range where no force is required to reset. . . . .	109
6-1	Experimental setup used to measure the friction coefficient $C_f$ . (a) The geometry is a rectangular plate used to measure the friction coefficient $C_f^\perp$ , where the frictional force $F_f$ is perpendicular to the moving direction of the geometry. (b) The geometry is a thin-walled circular cylinder used to measure the friction coefficient $C_f^\parallel$ , where the frictional force $F_f$ is parallel to the moving direction of the geometry. . . . .	119
6-2	$\tau/L^2$ versus $F_N/WL$ for thickness $W = 0.2032\text{mm}$ . (Inset) Torque ( $\text{N} \cdot \text{m}$ ) as a function of normal force ( $\text{N}$ ) for three lengths, $L$ ( $\text{mm}$ ) and for three angular velocities, $\Omega$ ( $\text{rad/s}$ ). Dashed lines are linear regression lines. The slope of the linear regression line is 0.96. . . . .	123
6-3	$4\tau/L(N)$ versus $F_N(N)$ for thickness $W = 0.2032\text{mm}$ for three lengths, $L$ ( $\text{mm}$ ) and for three angular velocities, $\Omega$ ( $\text{rad/s}$ ). Dashed lines are linear regression lines. The slope of the linear regression line is $0.22 \pm 0.02$ . . . . .	125

7-1 (a) Predicted friction coefficient  $\ln \hat{C}_f^{\parallel}$  versus experimental friction coefficient  $\ln C_f^{\parallel}$  using linear regression for Hersey number ranging from  $10^{-9}$  to  $10^{-7}$ . Three dimensionless groups are taken into account:  $\mathbf{X} = [\ln \Pi_1, \ln \Pi_2, \ln \Pi_3]$ . The diagonal blue line indicates the perfect prediction of  $\ln C_f^{\parallel}$ . The  $R^2$  of this model is 0.97. (b) Probability density as a function of the residual between the prediction and experimental results of friction coefficient  $\ln C_f^{\parallel} - \ln \hat{C}_f^{\parallel}$  using linear regression for Hersey number ranging from  $10^{-9}$  to  $10^{-7}$ . The orange line indicates a kernel density estimation (KDE). The standard deviation  $\sigma = 0.08$ . (c) Predicted friction coefficient  $\ln \hat{C}_f^{\parallel}$  versus experimental friction coefficient  $\ln C_f^{\parallel}$  using linear regression for Hersey number ranging from  $10^{-7}$  to  $10^{-4}$ . Three dimensionless groups are taken into account:  $\mathbf{X} = [\ln \Pi_1, \ln \Pi_2, \ln \Pi_3]$ . The diagonal blue line indicates the perfect prediction of  $\ln C_f^{\parallel}$ . The  $R^2$  of this model is 0.97. (d) Probability density as a function of the residual between the prediction and experimental results of friction coefficient  $\ln C_f^{\parallel} - \ln \hat{C}_f^{\parallel}$  using linear regression for Hersey number ranging from  $10^{-7}$  to  $10^{-4}$ . The orange line indicates a kernel density estimation (KDE). The standard deviation  $\sigma = 0.06$ . . . . . 132

8-1 (a) Predicted friction coefficient  $\hat{C}_f^{\parallel}$  versus experimental friction coefficient  $C_f^{\parallel}$  using linear regression for Hersey number ranging from  $10^{-9}$  to  $10^{-5}$ . All the seven variables are taken into account:  $\mathbf{X} = [\mathbf{L}, \mathbf{W}, \mathbf{U}, \mathbf{F}, \Pi_1, \Pi_2, \Pi_3]$ . The diagonal blue line indicates the perfect prediction of  $C_f^{\parallel}$ . The  $R^2$  of the model is 0.57. (b) Probability density as a function of the residual between the prediction and experimental results of friction coefficient  $C_f^{\parallel} - \hat{C}_f^{\parallel}$  using linear regression for Hersey number ranging from  $10^{-9}$  to  $10^{-5}$ . The orange line indicates a kernel density estimation (KDE). The standard deviation of the residual is 0.015. . . . . 136

8-2 (a) Predicted friction coefficient  $\ln \hat{C}_f^{\parallel}$  versus experimental friction coefficient  $\ln C_f^{\parallel}$  using linear regression for Hersey number ranging from  $10^{-9}$  to  $10^{-7}$ . Three dimensionless groups are taken into account:  $\mathbf{X} = [\ln \Pi_1, \ln \Pi_2, \ln \Pi_3]$ . The diagonal blue line indicates the perfect prediction of  $\ln C_f^{\parallel}$ . The  $R^2$  of this model is 0.97. (b) Probability density as a function of the residual between the prediction and experimental results of friction coefficient  $\ln C_f^{\parallel} - \ln \hat{C}_f^{\parallel}$  using linear regression for Hersey number ranging from  $10^{-9}$  to  $10^{-7}$ . The orange line indicates a kernel density estimation (KDE). The standard deviation  $\sigma = 0.08$ . (c) Predicted friction coefficient  $\ln \hat{C}_f^{\parallel}$  versus experimental friction coefficient  $\ln C_f^{\parallel}$  using linear regression for Hersey number ranging from  $10^{-7}$  to  $10^{-4}$ . Three dimensionless groups are taken into account:  $\mathbf{X} = [\ln \Pi_1, \ln \Pi_2, \ln \Pi_3]$ . The diagonal blue line indicates the perfect prediction of  $\ln C_f^{\parallel}$ . The  $R^2$  of this model is 0.97. (d) Probability density as a function of the residual between the prediction and experimental results of friction coefficient  $\ln C_f^{\parallel} - \ln \hat{C}_f^{\parallel}$  using linear regression for Hersey number ranging from  $10^{-7}$  to  $10^{-4}$ . The orange line indicates a kernel density estimation (KDE). The standard deviation  $\sigma = 0.06$ . . . . . 138

8-3 Predicted friction coefficient  $\hat{C}_f^{\parallel}$  versus experimental friction coefficient  $C_f^{\parallel}$  using Random Forest regression. (a) Regression results using original experimental variables, where  $\mathbf{X} = [\mathbf{L}, \mathbf{W}, \mathbf{U}, \mathbf{F}]$ . The diagonal blue line indicates the perfect prediction of  $C_f$ . The  $R^2$  of the model is 0.972. (b) Regression results using dimensionless groups, where  $\mathbf{X} = [\ln \Pi_1, \ln \Pi_2, \ln \Pi_3]$ . The diagonal blue line indicates the perfect prediction of  $C_f$ . The  $R^2$  of the model is 0.976. . . . . 140

8-4	Probability density as a function of $C_f - \hat{C}_f$ using Random Forest regression. (a) Regression results using original experimental variables, where $\mathbf{X} = [\mathbf{L}, \mathbf{W}, \mathbf{U}, \mathbf{F}]$ ; (b) Probability density as a function of the residual between the prediction and experimental results of friction coefficient $C_f^{\parallel} - \hat{C}_f^{\parallel}$ using dimensionless groups, where $\mathbf{X} = [\ln \Pi_1, \ln \Pi_2, \ln \Pi_3]$ . . . . .	141
8-5	(a) Predicted friction coefficient $\ln \hat{C}_f^{\parallel}$ versus experimental friction coefficient $\ln C_f^{\parallel}$ using neural network regression for Hersey number ranging from $10^{-9}$ to $10^{-7}$ . Three dimensionless groups are taken into account: $\mathbf{X} = [\ln \Pi_1, \ln \Pi_2, \ln \Pi_3]$ . The diagonal blue line indicates the perfect prediction of $\ln C_f^{\parallel}$ . The $R^2$ of this model is 0.97. (b) Probability density as a function of the residual between the prediction and experimental results of friction coefficient $\ln C_f^{\parallel} - \ln \hat{C}_f^{\parallel}$ using linear regression for Hersey number ranging from $10^{-9}$ to $10^{-7}$ . The orange line indicates a kernel density estimation (KDE). . . . .	144
A-1	Approval letter for the study titled Customer Needs Identification of Sled Hockey Players. Exemption granted on 30-August-2017. . . . .	148
A-2	Non HSR letter for the study titled Test of a More Flexible Sled Hockey Stick. Exemption granted on 20-Feb-2017. . . . .	149
A-3	Non HSR letter for the study titled Test of a More Flexible Sled Hockey Stick. Exemption granted on 22-March-2017. . . . .	150
B-1	$\tau/L^2$ versus $F_N/WL$ for thickness $W = 0.4064\text{mm}$ . (Inset) Torque ( $\text{N} \cdot \text{m}$ ) as a function of normal force (N) for three lengths, L (mm) and for three angular velocities, $\Omega$ (rad/s). Dashed lines are linear regression lines. . . . .	152
B-2	$4\tau/L(N)$ versus $F_N(N)$ for thickness $W = 0.4064\text{mm}$ for three lengths, L (mm) and for three angular velocities, $\Omega$ (rad/s). Dashed lines are linear regression lines. The slope of the linear regression line is $0.22 \pm 0.03$ .	152



C-1 (a) Predicted friction coefficient  $\hat{C}_f^{\parallel}$  versus experimental friction coefficient  $C_f^{\parallel}$  using multi-linear regression for Hersey number ranging from  $10^{-9}$  to  $10^{-7}$ .  $\mathbf{X} = [\mathbf{L}, \mathbf{W}, \mathbf{U}, \mathbf{F}, \mathbf{\Pi}_1, \mathbf{\Pi}_2, \mathbf{\Pi}_3]$ . The diagonal blue line indicates the perfect prediction of  $C_f$ . The  $R^2$  of the model is 0.68. (b) Probability density as a function of the residual between the prediction and experimental results of friction coefficient  $C_f^{\parallel} - \hat{C}_f^{\parallel}$  using linear regression for Hersey number ranging from  $10^{-9}$  to  $10^{-7}$ . The orange line indicates a kernel density estimation (KDE). The standard deviation of the residual is 0.015. . . . . 154

C-2 (a) Predicted friction coefficient  $\hat{C}_f^{\parallel}$  versus experimental friction coefficient  $C_f^{\parallel}$  using multi-linear regression for Hersey number ranging from  $10^{-9}$  to  $10^{-7}$ .  $\mathbf{X} = [\ln \mathbf{L}, \ln \mathbf{W}, \ln \mathbf{U}, \ln \mathbf{F}, \ln \mathbf{\Pi}_1, \ln \mathbf{\Pi}_2, \ln \mathbf{\Pi}_3]$ . The diagonal blue line indicates the perfect prediction of  $C_f$ . The  $R^2$  of the model is 0.97. (b) Probability density as a function of the residual between the prediction and experimental results of friction coefficient  $C_f^{\parallel} - \hat{C}_f^{\parallel}$  using linear regression for Hersey number ranging from  $10^{-9}$  to  $10^{-7}$ . The orange line indicates a kernel density estimation (KDE). The standard deviation of the residual is 0.08. . . . . 154

C-3 (a) Predicted friction coefficient  $\hat{C}_f^{\parallel}$  versus experimental friction coefficient  $C_f^{\parallel}$  using random forest regression for Hersey number ranging from  $10^{-9}$  to  $10^{-7}$ .  $\mathbf{X} = [\mathbf{L}, \mathbf{W}, \mathbf{U}, \mathbf{F}, \mathbf{\Pi}_1, \mathbf{\Pi}_2, \mathbf{\Pi}_3]$ . The diagonal blue line indicates the perfect prediction of  $C_f$ . The  $R^2$  of the model is 0.975. (b) Probability density as a function of the residual between the prediction and experimental results of friction coefficient  $C_f^{\parallel} - \hat{C}_f^{\parallel}$  using linear regression for Hersey number ranging from  $10^{-9}$  to  $10^{-7}$ . The orange line indicates a kernel density estimation (KDE). . . . . 155

C-4 (a) Predicted friction coefficient  $\hat{C}_f^{\parallel}$  versus experimental friction coefficient  $C_f^{\parallel}$  using random forest regression for Hersey number ranging from  $10^{-9}$  to  $10^{-7}$ .  $\mathbf{X} = [\ln \mathbf{L}, \ln \mathbf{W}, \ln \mathbf{U}, \ln \mathbf{F}, \ln \mathbf{\Pi}_1, \ln \mathbf{\Pi}_2, \ln \mathbf{\Pi}_3]$ . The diagonal blue line indicates the perfect prediction of  $C_f$ . The  $R^2$  of the model is 0.987. (b) Probability density as a function of the residual between the prediction and experimental results of friction coefficient  $C_f^{\parallel} - \hat{C}_f^{\parallel}$  using linear regression for Hersey number ranging from  $10^{-9}$  to  $10^{-7}$ . The orange line indicates a kernel density estimation (KDE). 155



# List of Tables

- 2.1 CPU Time and Memory using Reduced-Order Modelling . . . . . 52
- 2.2 Diagram of stiffness value for the flexible and rigid sled hockey sticks 54
- 4.1 Stiffness of the flexible and rigid sled hockey sticks . . . . . 81



# Chapter 1

## Introduction

In complex physical systems, the governing physics and its parameters may encounter difficulties to identify and investigate. In this dissertation, we parametrize and optimize the physical systems, applying the methodologies in the field of structural/fluid dynamics, robotics, statistics and data science. We further develop and implement algorithms, for optimizing the governing parameters of the systems, for solving non-linear partial differential equations (PDEs), for modelling the governing physics and for forecasting and predicting the dynamics in complex dynamical systems.

### 1.1 What is Parametrization, Optimization and Customization

Parametrization, in this dissertation, is adapted from the terminology used in the field of mathematics, where used as the process of finding the parametric equations of curves, surfaces, manifolds or varieties [4]. Hereby, parametrization is defined as the process of identifying the governing equations and its parameters, used to characterize the dynamical systems. More broadly, parametrization also includes the process of physical inference, in particular for the study of tribology in this dissertation. We develop the methodologies and algorithms of parametrization for dynamical systems and physical inferences.

Optimization is widely used in many engineering fields, serving as a process to determine the optimal selection from a set of available space [5]. Hereby, optimization, in particular, is applied in finding the optimal parameters and hyper-parameters, in ODEs/PDEs and in statistical/machine-learning algorithms, respectively.

Customization, also known as personalization, is described as the process of tailoring services and/or products to accommodate individuals and/or groups [6]. Customization, hereby, is limited to the scope of the methodology used to tailor the parameters of the structural optimization, tied to groups of individuals.

## 1.2 What is Dynamical System

A dynamical system, in mathematics, is a manifold endowed with a family of smooth evolution functions, which map a point of the phase space back into the phase space [7, 8]; A dynamical system, in physics, refers particle(s) whose state evolves over time and thus obeys differential equations involving time derivatives [9].

In complex physical systems, the parameters and governing physics are difficult to identify and investigate. In this thesis, we analyze and parametrize the physical systems, applying the methodologies in the field of structural/fluid dynamics and robotics. We further design and implement algorithms for optimizing the governing parameters of the systems, for solving non-linear partial differential equations (PDEs), for modelling the governing physics and for forecasting and predicting the dynamics in complex systems. Further, we apply the methodology of analysis and algorithms on ice hockey equipment. Ice hockey, referred to as stand-up hockey in this dissertation, is a contact sport invented in 1800s, in which two teams play against each other using hockey sticks to manoeuvre a puck into the opponent's net to score points [10, 11]. Characterized by the high intensity intermittent skating and frequent body contact, stand-up hockey sustains its popularity in many countries and was adopted in the Olympic games in 1920 [12, 13, 14].

Sled hockey, an adaptation of stand-up hockey, allows people with physical disabilities to participate in the game of ice hockey [15, 16]. Sled hockey, also known

as sledge hockey outside the US, is a much newer sport than stand-up hockey. It was invented in 1960s in Sweden and adopted as a sport in Paralympic games in 1994 [17, 18]. Sled hockey allows participants with mobility limitations, such as leg or hip injuries, amputees and able-bodied people with knee to play, requiring greater upper-body strength and capability of balance [19, 20].

In terms of the concept and rules, sled hockey is very similar to stand-up hockey. The primary difference is that sled hockey deploys an adaptive equipment, known as hockey sled, for sled hockey players to sit in and drive themselves with a pair of hockey sticks, instead of skating as in stand-up hockey.

The equipment in sled hockey primarily consists of a hockey sled and a pair of hockey sticks. The hockey sled includes a sled bucket, two skate blades affixed to the sled bucket, a leg support, a foot support and a suspension system to secure all the components. Hockey sticks are utilized for two primary functions: one for sled hockey players to drive the hockey sled in the ice rink, the other for sled hockey players to maneuver and shoot a puck to score points, referred to as driving mode and shooting mode, respectively. Therefore, sled hockey sticks are designed with a ratchet anchored on one end for driving and with a tapered curvature on the other end for maneuvering and shooting.

### **1.3 Scope of Study**

In this project, we collaborated with the Wheelchair Sports Federation New York Sled Rangers. The Wheelchair Sports Federation is a national non-profit organization that provides opportunities for disabled adults and youths to play sports recreationally and competitively [1]. The WSF is one of the earliest organizations to provide adaptive athletes with opportunities to participate in a multitude of adaptive sports [1]. The WSF can trace its birth to the adaptive sports program created at the Eastern Paralyzed Veterans Association in NYC. The WSF sponsors adaptive sports such as: Archery, Billiards, Bowling, Boxing, Fencing, Fishing, Flying, Handcycling, Hunting, Mountain Biking, Powerlifting, Rugby, Swimming, Team Handball, Track & Field,



Water Skiing, Wheelchair Basketball, Wheelchair Football, Wheelchair Tennis, Winter Skiing [1].

This project lies at the intersection of multiple interdisciplinary fields, including the techniques in structural dynamics, fluid dynamics, algorithms, data science, heat transfer, product design and machine design with optimization methods. This dissertation presents fundamental investigations of the dynamics and mechanics in the game of sled hockey, by parametrizing, optimizing and customizing the sled hockey equipment, primarily consisting of hockey sticks and hockey sleds.

Research on the study of sled hockey in prior arts is very rare [21]. We hope our study can serve as a fundamental work for this field, in particular for the community of designers of sled hockey and junior sled hockey players with ages from five through twenty-one. To determine the scope of our study, we perform systematic procedures of customer needs identification through interviews and surveys. Based on the results, we further apply a quality function deployment (QFD) analysis to prioritize the customer needs. (Approvals for all the interviews, surveys and experiments were obtained from the MIT Committee on the Use of Humans as Experimental Subjects (COUHES) prior to any human experimentation. Please see Appendix for the approvals.)

### **1.3.1 Scope Identification**

We conducted an online survey based on the responses we received from sled hockey players in 2016 summer. We also used information from interviews in 2016 October discussing a series of more open-ended questions. The answers from players, their parents and coaches were extremely valuable to us and we attempted to categorize them into a few reoccurring themes. The questions in the survey were based on those themes. There were ten players, ten parents, four coaches and three others who participated this online survey during one month. Fig. 1-1 summarizes the priority of customer needs for different features of sled hockey. The top one indicates the highest priority. The survey results suggest that "Customization of hockey sled based on the physical condition" plays the most important role. In the survey, we summarize 10

customer needs based on our interview results:

1. The sled is more customizable based on player's physical condition and playing ability.
2. The sled allows players to maneuver better.
3. The bucket is more comfortable to sit in.
4. The hockey stick allows players to make a more powerful shot.
5. The sled allows players to drive faster.
6. The foot support restrains feet better and allows more control.
7. The sled is easier to carry and takes less space to store.
8. The leg support is more comfortable.
9. The sled can be driven by someone with use of one hand.
10. Other suggestion(s).

In addition, Fig. 1-1 (Inset) shows the survey results from the coaches. From the perspective of coaches, the feature for the comfort of the bucket is less important than the feature for the hockey stick and the speed of the sled.

We applied a Quality Function Deployment (QFD) analysis to define customer requirements, translate the requirements into specific plans, and prioritize the requirements to facilitate decision-making and design.

QFD was developed by Oshiumi of the Kurume Mant plant of Bridgestone Tire in Japan in the late 1960s and spread to the US in the 1980s [22]. QFD was initially introduced to design and manufacturing, providing these fields with the planned quality control chart [22]. Fifteen years after it was developed, QFD was integrated with other improvement tools and introduced to other fields, including product development, course/curriculums development, model-change products and reliability test methods [23, 24, 25, 26, 27].

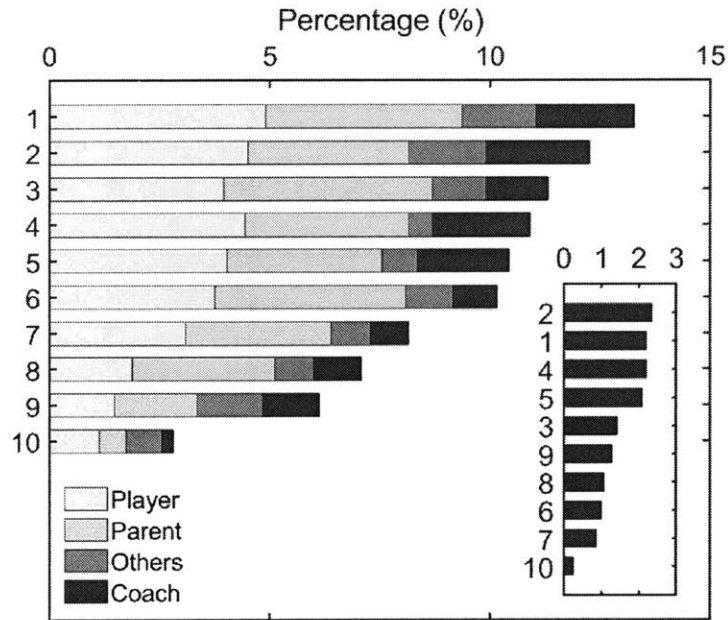


Figure 1-1: Survey results with 27 subjects, among which ten subjects are players, ten are parents, four are coaches and three are others. This survey is conducted to identify the stakeholder’s needs and their priorities. (Inset) Results only for coaches.

Fig. 1-2 shows our QFD analysis and its evaluation results for the customers’ priorities. The attributes and design parameters are set by the results of the survey and interview. The customers’ requirements, serving as attributes in QFD, can be divided into two categories: usability and performance. In the category of usability we have five requirements: customization of hockey sleds and hockey sticks, comfort of the bucket, restraint on the foot support, feasibility of carrying and storing and the comfort of leg support; in the category of performance, we have three requirement: maneuverability of the hockey sled, capability of a powerful shot for hockey sticks and capability of a faster drive for hockey sled. In the other dimension, we have ten technical requirements (design parameters): meeting the US standards, the weight of sleds, the stiffness of hockey sticks, the customization of the sled bucket form, the sled bucket material, the customization of the sled structure, the type and form of the skate blades, the restraints of the design, the suspension system and the sled dynamic reconfiguration. In the roof of the QFD house, we analyze the correlation of each pair of technical requirements and in the body of the QFD house, we analyze

the correlation between each pair of customer requirement and technical requirement. For each customer requirement, we can determine its priority based on the relative score.

As shown in Fig. 1-2, the priority of customer needs can be identified. The top four customer needs are: (1) To improve the customization of hockey sleds and hockey sticks. (2) To increase the maneuverability of the hockey sled. (3) To improve the comfort of the sled bucket. (4) To design hockey sticks with a more powerful shot.

The scope of the study is primarily determined by the survey results and the QFD results. We value the feedback and the survey results from coaches in particular. This dissertation covers the study of No.1, No.2, No.4, and No.5 of the ten summarized features aforementioned. To fulfill the study of the four features, we can perform investigation from three aspects: the dynamics of sled hockey sticks, the dynamics of sled hockey sleds and the physics of friction between ice and skate blades.

### **1.3.2 Outline of the Dissertation**

This dissertation presents fundamental investigations of the analysis and algorithms for the study of dynamical systems, by parametrizing, optimizing and customizing. We develop and/or implement numerical algorithms, for solving ODEs/PDEs, and statistical/machine-learning algorithms based on data, for physical inference and prediction. We further apply the methodologies on sled hockey, an adaptation of stand-up hockey, allows people with physical disabilities to participate in the game of ice hockey.

In Chapter 2, we develop and implement numerical algorithms for solving non-linear PDEs; in particular, we apply the algorithms on the study of the nonlinear dynamics described by 4th-order nonlinear PDEs. The non-linear solvers apply multi-dimensional Newton's method with a Jacobian-free approach and a generalized conjugate residual (GCR) approach. Applying the algorithms on the study of elastic systems, we investigate dynamics of hockey sticks as in a striking implement. We develop a mathematical model using an Euler-Lagrange equation to characterize the behavior of a hockey stick in the linear regime, and then apply this model to inves-

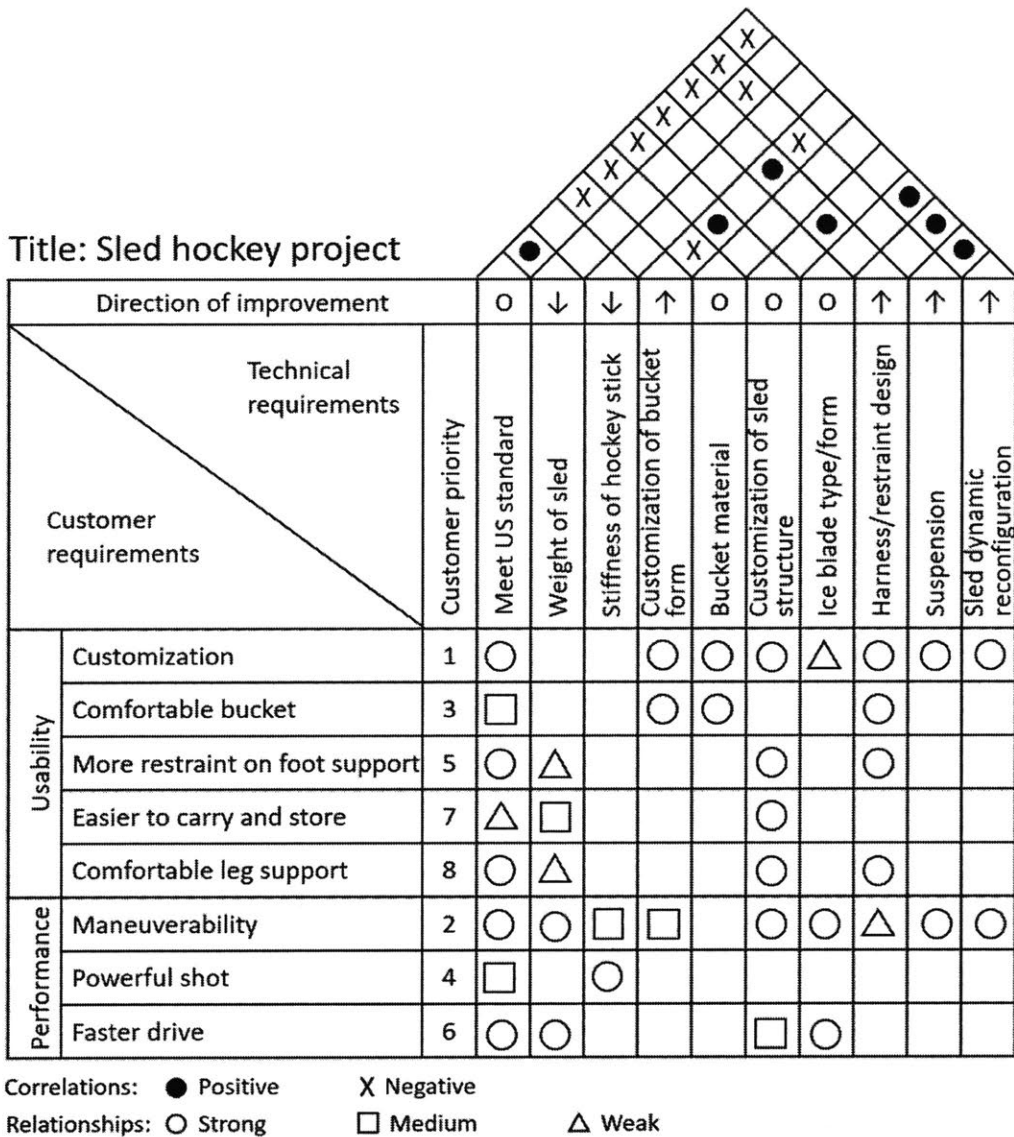


Figure 1-2: Quality Function Deployment (QFD) analysis for the sled hockey project. The customer requirements and technical requirements serve as the attributes and design parameters in QFD analysis, respectively. According to the results from the interview and survey, we consider eight attributes and ten design parameters. The attributes are prioritized from 1 (top priority) to 8 (bottom priority), based on the evaluation results for the relationships between the customer requirements and technical requirements.

tigate the dynamic response of the stick throughout slap shots and wrist shots. We numerically investigate the dynamic response of a hockey stick in the process of a 'slap shot', whereby a hockey stick traveling with a high velocity makes contact with a static puck on a low friction surface. The results of this study will be used to optimize the structure of the hockey beam with the goal to maximize the energy-transfer efficiency between the hockey stick and hockey puck.

In Chapter 3, to investigate the dynamics of a sled hockey stick as it impacts the puck, we use an Euler-Bernoulli beam to model the elastic response of the striking implement. We develop a mathematical model using an Euler-Lagrange equation to characterize the behavior of a hockey stick in the linear regime, and then apply this model to investigate the dynamic response of the stick throughout slap shots. We apply a modal decomposition method and decouple the resultant dynamics into kinetic and potential components. In addition, we implement numerical solvers to expand the study into the nonlinear regime described by a 4th-order nonlinear PDE. The non-linear solver applies multi-dimensional Newton's method with a Jacobian-free approach and a generalized conjugate residual (GCR) approach. Throughout testing with both elite and amateur sled hockey players, we found that final puck velocities with our prototype stick were on average over 10% higher compared to those achieved with commercially available sticks.

In Chapter 4, we investigate a dynamical model to simulate the dynamics of a wrist shot and explore the optimal flexural rigidity of a sled hockey stick. In our simulation, we model the dynamics of a wrist shot by utilizing an Euler-Bernoulli cantilevered beam model with a cylindrical rigid body attached to its distal end. This dynamic system is governed by a 4th-order PDE. We solve for the transverse deflection of the beam and the puck motion applying a modal decomposition method. Based on the simulation results and the constraint in shooting mode and driving mode, a more flexible sled hockey stick is proposed and verified. In particular, the optimal flexural rigidity can be determined by the compromise of maximizing the magnitude of the puck velocity in the shooting mode and maximizing the feasibility of propulsion in the driving mode.

In Chapter 5, to investigate the dynamics of the hockey sled, we propose two sets of dynamical modelling for the hockey sled using a trajectory-based modelling method and a state-space-based modelling method. Conservation laws of linear momentum and angular momentum are applied to obtain the governing equations, which are used to study the dynamics of the propulsion for linear motion and of the tip-over and reset. We further propose a constrained optimization problem to optimize the parameters of sled design and driving strategy to maximize the performance of sled hockey players based on the dynamics.

In Chapter 6, we investigate the tribology in the game of sled ice hockey. Sled hockey is a competitive sport taking place on ice. The friction between ice surface and skate blades affects the performance of the hockey stop, the hockey turn, the propulsion for linear motion and the process of reset after tip-over, which are discussed in previous chapters. The physics of ice friction is still under debate in previous research [28]. We first attempt to design an experimental system to mimic the realistic ice rink environment. We also expand the experimental study of the friction coefficient in an extensive range of Hersey number from  $10^{-13}$  to  $10^{-4}$  with the reference to the Stribeck curve. To build the understanding of the physics of the ice friction, we perform a dimensional analysis and an asymptotic analysis for different regimes of friction - boundary friction regime, mixed friction regime and hydrodynamic lubrication regime. In addition, we provide a parametric model - multi-linear regression and a non-parametric model - random forest regression to study relationship between the friction coefficient and the Hersey number varying eight orders of magnitude .

In Chapter 7, to infer the physical regime with respect to the modified Stribeck curve, we developed a pipeline using clustering methodologies adapted from the field of data science. This chapter starts with the restate of the results from dimensional analysis and asymptotic analysis. We present the algorithms for clustering models using K-means clustering and Gaussian mixture clustering, followed by the clustering results based on our experimental data.

In Chapter 8, we develop and/or implement statistical algorithms and machine learning algorithms for the friction coefficient between ice and skate blades. Our

experiments measuring the friction coefficient using rheometers are designed to mimic the real environment of ice rink, where the ice is made by a Peltier plate exposed to an ambient room temperature. Based on our experimental data, we propose a set of parametric and non-parametric models for the friction coefficient using machine learning techniques in an extensive range of Hersey number from  $10^{-12}$  to  $10^{-5}$ . For each regression technique, we propose two models for the friction coefficient  $C_f (= \Pi_1)$ . The first one uses the original set of parameters, i.e. the blade length  $L$ , the blade thickness  $W$ , the water viscosity  $\mu$ , the Young's modulus of ice  $E$ , the relative velocity of blade with respect to ice  $v$ , and the normal force exerted on ice by the blade  $F_n$ ; the second one uses the dimensionless groups, i.e. the aspect ratio of skate blades  $\Pi_2 = L/W$ , the Hersey number  $\Pi_3 = \mu v L / F_n$ , and the ratio of pressure on ice to the Young's modulus of ice  $\Pi_4 = F / ELW$ . The first model applies all of the four experimental variables as features; the second model applies three dimensionless groups as features in the reduced form.

In terms of the future work, there are a number of avenues which could be explored. Our investigation serves as a fundamental study in the field of sled hockey, in particular for the community of young sled hockey players with ages from five to twenty-one. We focus on the dynamical modelling of hockey sleds and hockey sticks and the physics of the friction between ice and skate blades. We believe a fruitful of further investigations can be performed based on our study.





# Chapter 2

## Algorithms of Numerical Methods for Non-Linear PDEs

### 2.1 Background and Introduction

In this chapter, we develop and implement numerical algorithms for solving non-linear PDEs; in particular, we apply the algorithms on the study of the nonlinear dynamics described by 4th-order nonlinear PDEs. The non-linear solvers apply multi-dimensional Newton's method with a Jacobian-free approach and a generalized conjugate residual (GCR) approach.

Applying the algorithms on the study of elastic systems, we investigate dynamics of hockey sticks as in a striking implement. We develop a mathematical model using an Euler-Lagrange equation to characterize the behavior of a hockey stick in the linear regime, and then apply this model to investigate the dynamic response of the stick throughout slap shots and wrist shots. We numerically investigate the dynamic response of a hockey stick in the process of a 'slap shot', whereby a hockey stick traveling with a high velocity makes contact with a static puck on a low friction surface. The results of this study will be used to optimize the structure of the hockey beam with the goal to maximize the energy-transfer efficiency between the hockey stick and hockey puck.

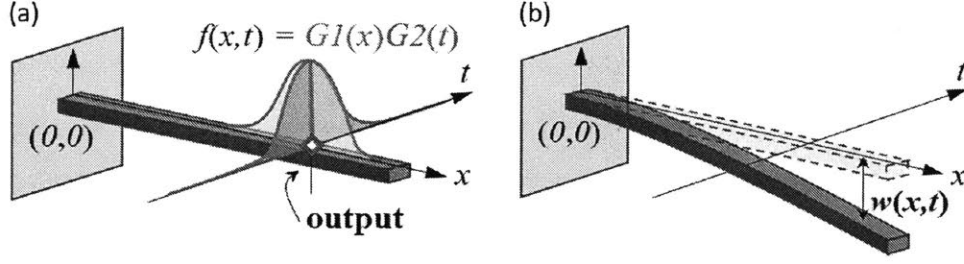


Figure 2-1: (a) Cantilevered Euler-Bernoulli beam fixed at  $(0,0)$  with a Gaussian distributive load as function of space and time,  $f(x,t) = G_1(x)G_2(t)$ . We select the diamond point as the output point for the deflection of the beam. (b) Deflection of the loaded beam under external load as a function of space and time.

## 2.2 Algorithms of Numerical Methods

To emphasize the development of numerical solver, the process of a 'slap shot' is simplified. The hockey stick is modelled as a cantilevered Euler-Bernoulli beam. Impact between the puck and hockey stick is modelled as a Gaussian force distribution applied to the hockey stick in space  $G_1(x)$  and in time  $G_2(t)$  (see Fig. 2-1 (a)). We simulate the dynamics of the beam characterized by the transverse deflection  $w(x,t)$ , as shown in Fig. 2-1 (b). The governing equation for the transient dynamics of an Euler-Bernoulli beam is the 4th-order non-linear and non-homogeneous PDE shown in Eqn. 2.1,

$$\begin{aligned}
 & \underbrace{\rho A_0 \frac{\partial^2 w(x,t)}{\partial t^2}}_{\text{Inertia}} + \underbrace{EI \frac{\partial^4 w(x,t)}{\partial x^4}}_{\text{Bending Stiffness (linear)}} + \underbrace{b \frac{\partial^5 w(x,t)}{\partial t \partial x^4}}_{\text{Internal Friction}} \\
 & + \underbrace{\left( -\frac{3}{2} EA_0 \right) \left( \frac{\partial w(x,t)}{\partial x} \right)^2 \left( \frac{\partial^2 w(x,t)}{\partial x^2} \right)}_{\text{Bending Stiffness (nonlinear)}} = \underbrace{f(x,t)}_{\text{External Force}}
 \end{aligned} \tag{2.1}$$

where  $w(x,t)$  is the transverse deflection of the beam,  $EI$  is the rigidity of the beam,  $\rho A_0$  represents the mass distribution of the beam,  $b$  represent the internal friction

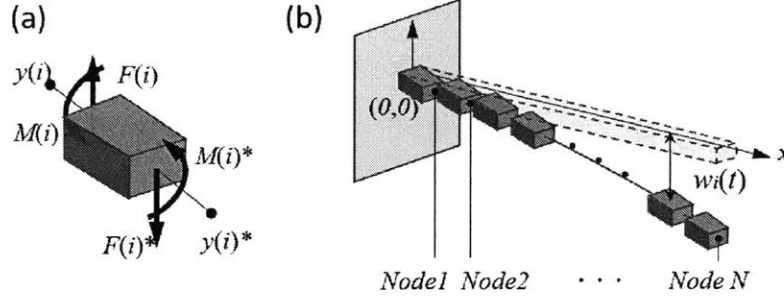


Figure 2-2: Transverse deflection of the beam in the form of discrete representation. (a) Free body diagram of each discrete element; (b) Discrete representation of a beam with  $N$  nodes.

coefficient (damping coefficient) and  $f(x, t)$  represents the spatial and temporal distribution of the force applied [3, 29].

## 2.2.1 Algorithms of Numerical Solvers for Linear PDEs

For simplicity and illustration on the numerical methods, we linearize the governing equation Eqn. 2.1 by neglecting the non-linear term. In addition, we also ignore the internal friction term to further simply the equation. The numerical methods for non-linear bending stiffness and the internal friction will be discussed in the following sections. The simplified PDE has the form:

$$\rho A \frac{\partial^2 y}{\partial t^2} + EI \frac{\partial^4 y}{\partial x^4} = b(x, t), \quad (2.2)$$

where  $y(x, t)$  is the transverse deflection of the beam,  $EI$  is the rigidity of the beam,  $\rho A$  represents the mass distribution of the beam, and  $b(x, t)$  represents the spatial and temporal distribution of the force applied [29].

In the spatial domain, we apply a central finite difference method to numerically approximate the partial derivative with respect to  $x$ :

$$\frac{\partial^4 y_i}{\partial x^4} \approx \frac{y_{i-2} - 4y_{i-1} + 6y_i - 4y_{i+1} + y_{i+2}}{\Delta x^4}. \quad (2.3)$$

Physically,  $y_i$  represents the transverse deflection of the  $i$ -th node as shown in Fig. 2-2

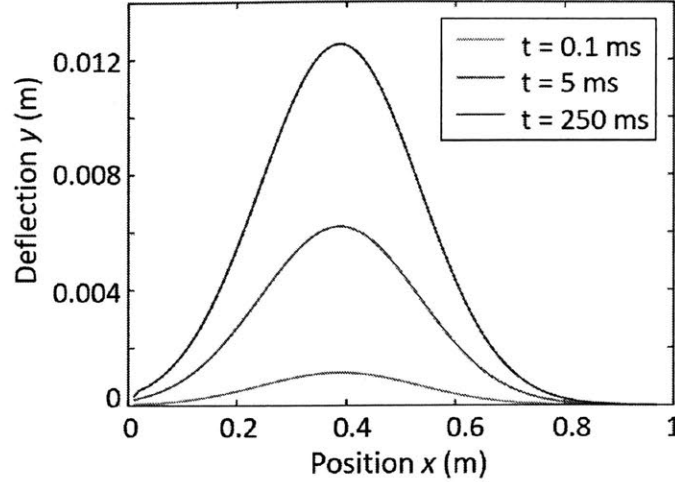


Figure 2-3: Deflection  $y$  (m) as a function of position  $x$  (m) for time  $t = 0.1$  ms,  $t = 5$  ms,  $t = 250$  ms. The external load is a Gaussian distributive force in space, of which the center is located at  $x = 0.4$  m. Trapezoidal integration method with a dynamically adjusted time step is applied.

(b). To convert the discrete representation equivalent to the continuous system, shear force and bending torque on the cross-sections are required. (see Fig. 2-2 (a))

In the temporal domain, we apply a forward Euler method and a trapezoidal integration method. Using the forward Euler method, the partial derivative with respect to time  $t$  can be approximated:

$$\frac{\partial y^k}{\partial t} \approx \frac{y^{k+1} - y^k}{\Delta t}. \quad (2.4)$$

Applying the trapezoidal rule to the temporal integration, the approximation of the derivative can be implicitly approximated as:

$$\frac{1}{2} \left( \frac{\partial y^{k+1}}{\partial t} + \frac{\partial y^k}{\partial t} \right) \approx \frac{y^{k+1} - y^k}{\Delta t} \quad (2.5)$$

By define  $y_0 = y$ ,  $y_1 = \partial y_0 / \partial t$ , we decompose Eqn. 2.2 into two PDEs with only first order temporal derivatives. We then apply the discretization methods mentioned above on the system of PDEs. For clarity, we put the discretized PDE in matrix

form. Using the forward Euler method, we have

$$\begin{bmatrix} \mathbf{y}_0^{k+1} \\ \mathbf{y}_1^{k+1} \end{bmatrix} = \begin{bmatrix} \mathbb{I} & \Delta t \mathbb{I} \\ \lambda_1 \Delta t \mathbb{D} & \mathbb{I} \end{bmatrix} \begin{bmatrix} \mathbf{y}_0^k \\ \mathbf{y}_1^k \end{bmatrix} + \begin{bmatrix} \mathbf{0} \\ \Delta t \lambda_2 \mathbf{b}^k \end{bmatrix}, \quad (2.6)$$

where  $\mathbf{y}_0^k = [y_{0,1}^k, y_{0,2}^k, \dots, y_{0,N}^k]^T$  and  $\mathbf{y}_1^k = [y_{1,1}^k, y_{1,2}^k, \dots, y_{1,N}^k]^T$ ,  $\mathbb{I}$  is a identity matrix,  $\lambda_1$  and  $\lambda_2$  are constants with lumped parameters of the beam:

$$\lambda_1 = -\frac{EI}{\rho A}, \quad \lambda_2 = \frac{1}{\rho A}, \quad (2.7)$$

and matrix  $\mathbb{D}$  is the matrix of coefficients using a central finite difference method to approximate a 4-th order derivative:

$$\mathbb{D} = \begin{bmatrix} 6 & -4 & 1 & \dots & 0 \\ -4 & 6 & -4 & \dots & 0 \\ 1 & -4 & 6 & \dots & 0 \\ \vdots & \vdots & \vdots & \ddots & \vdots \\ 0 & 0 & 0 & \dots & 6 \end{bmatrix}. \quad (2.8)$$

Similarly, using the trapezoidal integration method, the PDE can be discretized as:

$$\begin{bmatrix} \mathbb{I} & -\frac{1}{2} \Delta t \mathbb{I} \\ -\frac{1}{2} \lambda_1 \Delta t \mathbb{D} & \mathbb{I} \end{bmatrix} \begin{bmatrix} \mathbf{y}_0^{k+1} \\ \mathbf{y}_1^{k+1} \end{bmatrix} = \begin{bmatrix} \mathbb{I} & \frac{1}{2} \Delta t \mathbb{I} \\ \frac{1}{2} \lambda_1 \Delta t \mathbb{D} & \mathbb{I} \end{bmatrix} \begin{bmatrix} \mathbf{y}_0^k \\ \mathbf{y}_1^k \end{bmatrix} + \begin{bmatrix} \mathbf{0} \\ \frac{1}{2} \Delta t \lambda_2 (\mathbf{b}^k + \mathbf{b}^{k+1}) \end{bmatrix} \quad (2.9)$$

We implement the forward Euler and the trapezoidal integration methods to simulate the transient response of a Euler-Bernoulli beam with both ends clamped. Two different loads are applied to the beam: one is a Gaussian distributive load  $b(x)$  with respect to space centered at  $x = 0.4$  m; the other is an impulse force, which has the Gaussian distribution with respect to time. Fig. 2-3 shows the temporal evolution of the beam deflection at three time snapshots with the Gaussian distributive load and Fig. 2-4 shows the temporal evolution of the center point of the beam with the impulse force. In these two examples, it is preferable to apply the trapezoidal method

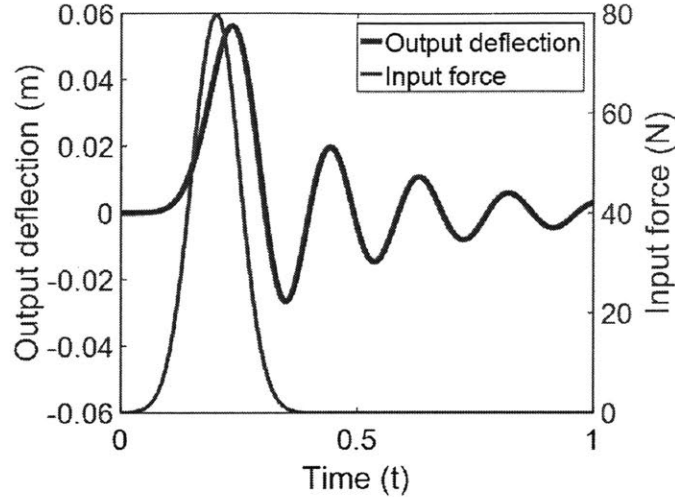


Figure 2-4: Deflection at the center of the beam as a function of position  $x$  (m) subject to an impulse input force. The impulse force is modelled as a Gaussian distributive force with respect to time. The internal friction term in Eqn. 2.1 is taken into account in this simulation.

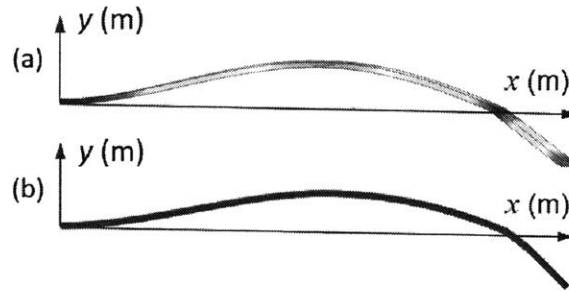


Figure 2-5: Deflection of a sled hockey stick under external load. (a) FEA simulation results using Solidworks with 289,959 DOF; (b) Simulation results using our 1D model.

other than forward Euler method considering the computational efficiency. For the implementation using forward Euler method, the maximal time step is  $\Delta t = 0.1 \mu s$  in order to guarantee the sufficient accuracy, while the largest time step for Trapezoidal integration method is  $\Delta t = 1 \mu s$ . It indicates that a total computation time required in the trapezoidal method is one-order smaller than that in the forward Euler method.

In order to verify our 1D finite difference model, we applied a finite element simulation using SolidWorks with 289,959 degrees of freedom. The result is presented and compared with our finite difference simulation result in Fig. 2-5. We observe

that these two methods generate similar results. A third eigenmode of  $\lambda = 20$  Hz is observed in the finite element simulation, and a third eigenmode of  $\lambda = 18$  Hz is obtained in our finite difference simulation. This agreement validates the correctness of our 1D finite difference model. Moreover, the computation time is 48s in the finite element simulation, while it only takes 0.017s using our 1D finite difference mode. Therefore, the computational efficiency of our 1D model is 2000 times better compared with that in the finite element simulation by SolidWorks.

### 2.2.2 Algorithms for Numerical Solvers for Non-Linear PDEs

In this chapter, we use numerical simulation to investigate the non-linear dynamics of the sled hockey stick. We simplify the governing equation in Eqn. 2.1 for the sled hockey stick by neglecting the inertia and internal friction terms but keeping the non-linear bending stiffness term. The simplified non-linear governing equation is:

$$EI \frac{\partial^4 y}{\partial x^4} - \frac{3}{2} EA \left( \frac{dy}{dx} \right)^2 \left( \frac{d^2 y}{dx^2} \right) = b(x), \quad (2.10)$$

where  $y(x)$  is the transverse deflection of the beam. In this section, we apply a finite difference method for discretization with three different techniques to handle the non-linear term, including Newton's method [30, 31], Jacobian-free Newton's method and Newton's method with generalized conjugate residual (GCR) method.

Using the finite difference method to solve for the nonlinear Eqn. 2.10 on an  $N$ -node grid, we have the discretized equation  $F(y) = 0$ :

$$F(y) = EI \frac{y_{i-2} - 4y_{i-1} + 6y_i - 4y_{i+1} + y_{i+2}}{\Delta x^4} - \frac{3}{2} EA \left( \frac{y_{i+1} - y_i}{\Delta x} \right)^2 \left( \frac{y_{i-1} - 2y_i + y_{i+1}}{\Delta x^2} \right) - b(x) = 0, \quad (2.11)$$

for the  $i$ -th node, where  $i \neq 1, 2, N-1, N$ . For the Newton's method, the Jacobian matrix can be obtained by taking the partial derivative with respect to each discretized  $y_i$ . Taylor expansion to the first order is used as an approximation for the non-linear function  $F(y)$  to construct the rooting finding formula. Newton's method using



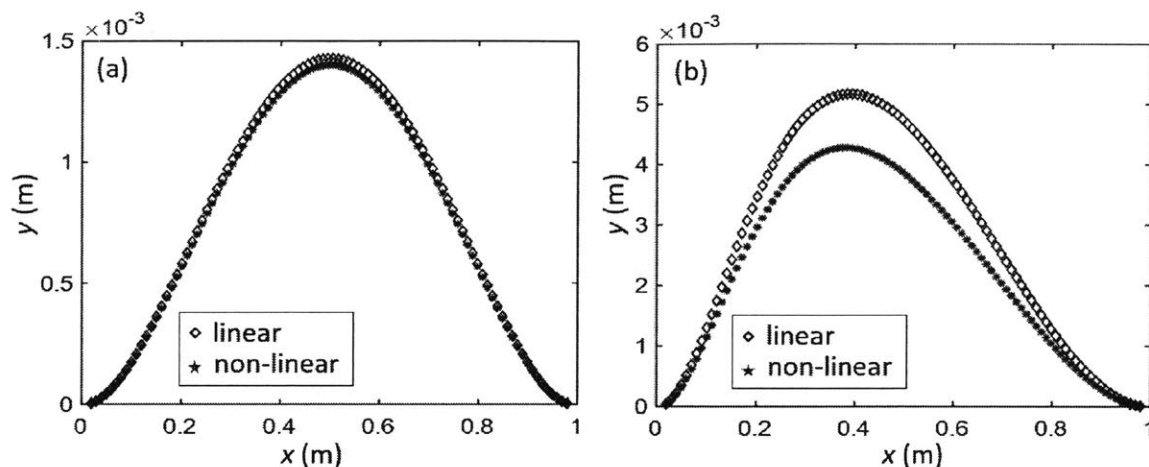


Figure 2-6: Transverse deflection  $y$  (m) of the beam as a function of the position  $x$  (m) for the beam equation with/without the non-linear term. (a) Beam subject to a uniform distributed load. The external force  $b(x)$  is a constant. (b) Beam subject to a Gaussian distributed load. The external force  $b(x)$  is centered at  $x = 0.1$ .

Jacobian matrix can be described as in Algorithm 1. For the Jacobian-free Newton's method, the product of Jacobian matrix and the residual vector can be approximated by a small perturbation on  $\mathbf{y}$  with  $\epsilon \mathbf{r}$  [32, 33, 34]:

$$\mathbb{J}_F(\mathbf{y}^k) \mathbf{r}_j \approx \frac{1}{\epsilon} [F(\mathbf{y}^k + \epsilon \mathbf{r}_j) - F(\mathbf{y}^k)]. \quad (2.12)$$

We also apply a generalized conjugate residual (GCR) method to solve the linearized equation in each iteration. GCR method is an iterative numerical method based on Krylov subspace, which is commonly used for solving systems of linear equations (see Algorithm. 2) [35, 36, 37].

---

**Algorithm 1** Pseudocode for Multi-Dimensional Newton's Method

---

- 1:  $k \leftarrow 0, \mathbf{y} \leftarrow \mathbf{y}_0$
  - 2: **procedure** ITERATION
  - 3:   Compute  $F(\mathbf{y}^k, \mathbb{J}_F(\mathbf{y}^k))$
  - 4:   Solve  $\mathbb{J}_F(\mathbf{y}^k) \Delta \mathbf{y}^{k+1} = -F(\mathbf{y}^k)$  for  $\Delta \mathbf{y}^{k+1}$
  - 5:    $\mathbf{y}_{k+1} \leftarrow \mathbf{y}^k + \Delta \mathbf{y}^{k+1}$
  - 6:    $k \leftarrow k + 1$
- 

We implement two examples to test the numerical methods. In the first example, we apply a uniform load on the beam; in the second example, we apply a Gaussian

---

**Algorithm 2** Pseudocode for GCR

---

```
1:  $k \leftarrow 0, \mathbf{y} \leftarrow \mathbf{0}, \mathbf{r}_k = \mathbf{b}$ 
2: procedure ITERATION
3:    $\mathbf{p}_k \leftarrow \mathbf{r}_k, \mathbf{A}\mathbf{p}_k \leftarrow \mathbb{A}\mathbf{p}_k$ 
4:    $\beta_{k,k-1} \leftarrow \langle \mathbf{A}\mathbf{p}_k, \mathbf{A}\mathbf{p}_{k-1} \rangle$ 
5:    $\mathbf{A}\mathbf{p}_k \leftarrow \mathbf{A}\mathbf{p}_k - \beta_{k,k-1}\mathbf{A}\mathbf{p}_{k-1}, \mathbf{p}_k \leftarrow \mathbf{p}_k - \beta_{k,k-1}\mathbf{p}_{k-1}$ 
6:    $\mathbf{A}\mathbf{p}_k \leftarrow \frac{\mathbf{A}\mathbf{p}_k}{\|\mathbf{A}\mathbf{p}_k\|}, \mathbf{p}_k \leftarrow \frac{\mathbf{p}_k}{\|\mathbf{p}_k\|}$ 
7:    $\alpha_k \leftarrow \langle \mathbf{r}_k, \mathbf{A}\mathbf{p}_k \rangle$ 
8:    $\mathbf{y}_{k+1} \leftarrow \mathbf{y}_k - \alpha_k\mathbf{p}_k, \mathbf{r}_{k+1} \leftarrow \mathbf{r}_k - \alpha_k\mathbf{A}\mathbf{p}_k$ 
9:    $k \leftarrow k + 1$ 
```

---

distributed load centered at  $x = 1$  on the beam. In both examples, the beam is subject to a clamped boundary condition for both ends. As shown in Fig. 2-6, we compare the results accounting for the non-linear term with those neglecting the non-linear term. In Fig. 2-6 (a), the non-linear deflection is small, resulting in a fast convergence rate. In Fig. 2-6 (b), the non-linear deflection is much larger. The convergence rate is significantly slower, which takes 25 iterations to converge.

### 2.2.3 Algorithms for Reduced-Order Methods

In this section, we use reduced-order modelling to further reduce the number of degrees of freedom in the dynamic system of the beam. We apply a eigenmode truncation method and a moment matching method, respectively, to select a suitable reduced-order basis to represent the original system. We consider the dynamics of the beam governed by the following liner PDE:

$$\rho A \frac{\partial^2 y}{\partial t^2} + EI \frac{\partial^4 y}{\partial x^4} = b(x, t), \quad (2.13)$$

where  $y$  is the transverse deflection of the beam,  $EI$  is the rigidity of the beam,  $\rho A$  represents the mass distribution of the beam, and  $b(x, t)$  represents the spatial and temporal distribution of the force applied [29].

In the spatial domain, we apply a central finite difference method to numerically approximate the partial derivative with respect to  $x$ . In the temporal domain, we apply a trapezoidal rule to integrate the equation in time. The discretized PDE can

be written in the following matrix form:

$$\begin{bmatrix} \mathbb{I} & -\frac{1}{2}\Delta t\mathbb{I} \\ -\frac{1}{2}\lambda_1\Delta t\mathbb{D} & \mathbb{I} \end{bmatrix} \begin{bmatrix} \mathbf{y}_0^{k+1} \\ \mathbf{y}_1^{k+1} \end{bmatrix} = \begin{bmatrix} \mathbb{I} & \frac{1}{2}\Delta t\mathbb{I} \\ \frac{1}{2}\lambda_1\Delta t\mathbb{D} & \mathbb{I} \end{bmatrix} \begin{bmatrix} \mathbf{y}_0^k \\ \mathbf{y}_1^k \end{bmatrix} + \begin{bmatrix} \mathbf{0} \\ \frac{1}{2}\Delta t\lambda_2(\mathbf{b}^k + \mathbf{b}^{k+1}) \end{bmatrix} \quad (2.14)$$

where  $\mathbf{y}_0^k = [y_{0,1}^k, y_{0,2}^k, \dots, y_{0,N}^k]^T$  and  $\mathbf{y}_1^k = [y_{1,1}^k, y_{1,2}^k, \dots, y_{1,N}^k]^T$ ,  $\mathbb{I}$  is a identity matrix,  $\lambda_1$  and  $\lambda_2$  are constants with lumped parameters of the beam.

We apply the eigenmode truncation method for the system [38, 39, 40]. We truncate the subdominant eigenvalues/poles by three metrics: (1) Certain modes are not affected by the input, indicating  $b_{q+1}, \dots, b_N$  are all small; (2) Certain modes do not affect the output, indicating  $c_{q+1}, \dots, c_N$  are all small; (3) Keep least negative eigenvalues (slowest modes) when we look at the response to a constant unit input [41, 42, 43].

To compare the frequency-domain response of the reduced models to the original non-reduced models, we produced the Bode plots as shown in Fig. 2-7. It shows that the reduced-order models agree with the original model with  $N = 500$  very well for low frequency ( $< 500$  Hz). It suggests that as more states are kept in the reduced model, it achieves better agreement with the original model as shown by the magnitude and phase in Bode plots.

In order to compare the time-domain step response of the reduced models to the original non-reduced models, we plotted the output deflection at  $x = 1$  as a function of time, using original system  $N = 500$  and using reduced system with  $q = 2$  and  $q = 10$  respectively as shown in Fig. 2-8. It shows that using a reduced model with  $q = 2$ , the error will be about 10%; using reduced models with  $q = 10$ , the errors will be smaller than 1%.

Table 2.1 compares the CPU time and memory required to execute the simulation using different models. We observe that even in the most time-consuming reduced model with  $q = 10$ , the CPU time is reduced to 2% of that for the original model. Meanwhile, all reduced models require significantly less memory than the original model.

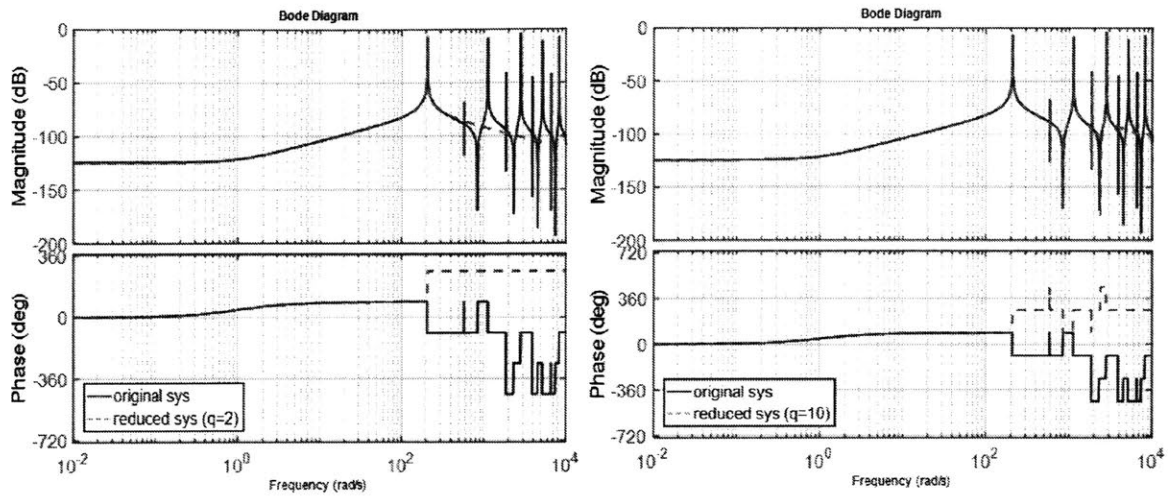


Figure 2-7: Comparison of Bode plots of the transfer functions, using original system  $N = 500$  and using reduced system with  $q = 2$  and  $10$  respectively (from left to right). The phase diagram appears to be shifted by  $360$  at some frequencies due to the plot setting using MATLAB by default.

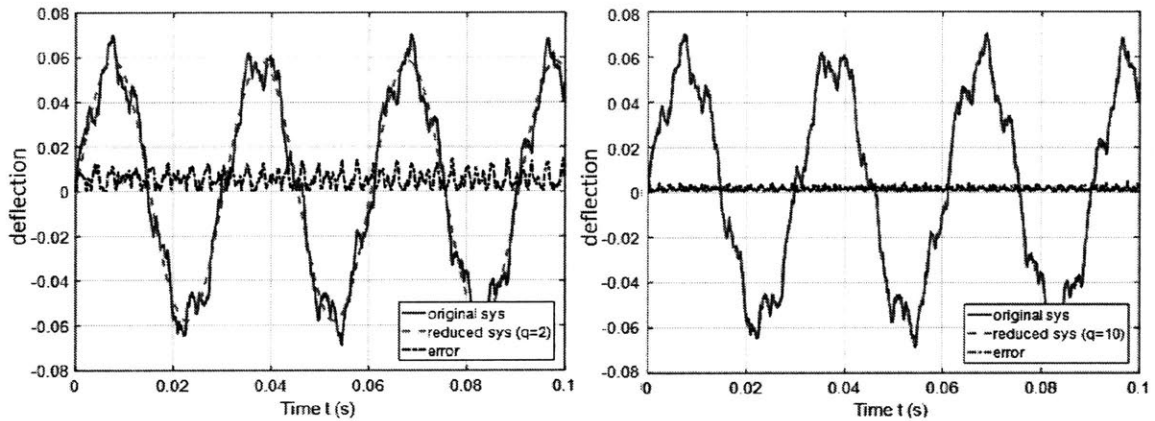


Figure 2-8: Comparison of deflections of a sinusoidal response of the Euler-Bernoulli beam as a function of time, using original system  $N = 500$  and using reduced system with  $q = 2$  and  $10$  respectively (from left to right).

Table 2.1: CPU Time and Memory using Reduced-Order Modelling

System	Executing Time (s)	Memory (M)
Original System $N = 100$	10.02	998
Reduced System $q = 2$	0.109	856
Reduced System $q = 5$	0.111	809
Reduced System $q = 10$	0.191	819

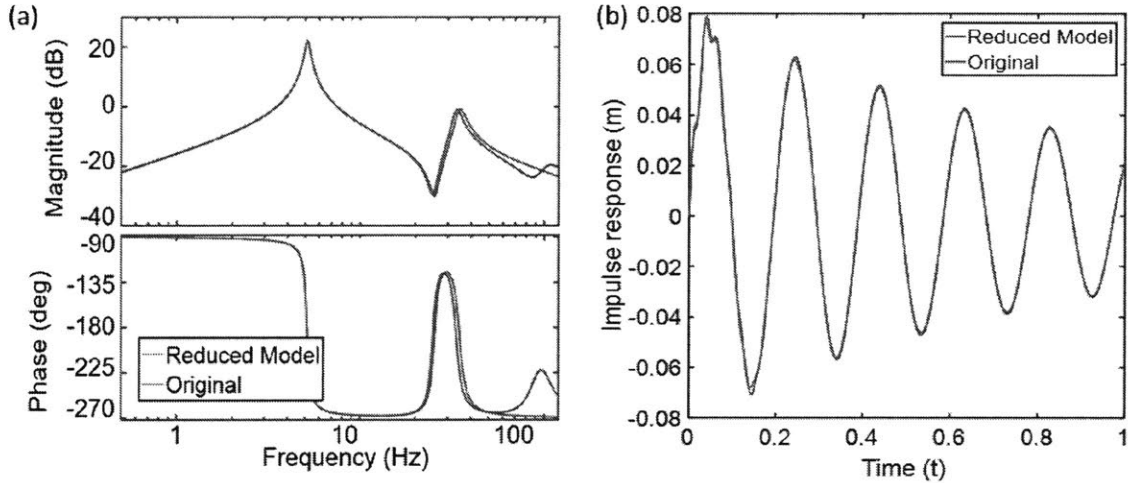


Figure 2-9: (a) Bode plot for the original system and reduced system using moment matching method. (b) Impulse response for original system and reduced system.

We also apply a moment matching approach to construct the reduced model by using Krylov subspace method specifically [44, 45, 46]. The first column of the projection matrix  $V_q$  is constructed using the normalized version of vector  $\mathbb{A}^{-1}b$ ; the second column is constructed by  $\mathbb{A}^{-1}$  multiplied by the first column above as right-hand-side, and then orthogonalized and normalized [47, 48, 49]. Since the solution span the space  $\mathbb{A}^{-1}b$ , we construct vector  $V_q$  by selecting the first  $q$  vectors in the Krylov subspace. Fig. 2-9 shows that a third-order reduced system can capture the dominant dynamics of the original system from both the frequency domain and temporal domain.

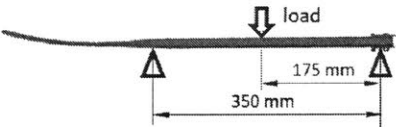
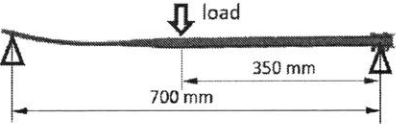
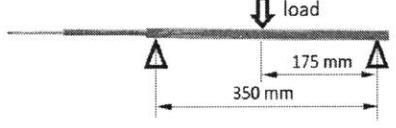
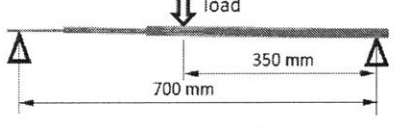
## 2.3 Experiments, Results and Discussion

Based on the simulation results presented in Fig. 3-6, the optimal stiffness for sled hockey sticks lies between  $E = 2.1 \text{ GPa}$  and  $E = 2.7 \text{ GPa}$ . To test this result, we

constructed a prototype sled hockey stick using ABS plastic (acrylonitrile butadiene styrene), which has a Young's modulus between 2.0 GPa to 2.6 GPa. As shown in Fig. 3-2, our prototype stick is made from five laminated layers of plastic. To manufacture the stick, each layer is cut from a large plastic sheet using a waterjet, and the layers are then bonded together using a flexible adhesive (Loctite 4851). Since players only use the shaft of the sled hockey sticks to drive the sled on ice, we tapered the blade part of the sticks to further reduce its flexural rigidity while shooting. In order to characterize the stiffness of the two types of sled hockey sticks, they were subjected to a three-point bend test. Since the shaft stiffness is much larger than that of the blade, we performed two types of loading, as shown in Table. 4.1, to measure the stiffness of the shaft and stiffness of the overall sled hockey stick. Testing was performed using an Instron Universal Testing Instrument (Model 1125). Each stick was loosely strapped at the middle and upper end of the shaft to two cylindrical supports [2, 50]. The maximum force was set to be 50 N, to simulate the load encountered on the stick during use [2, 50]. The load was applied by the platform using a cylindrical head. Stiffness was calculated as the slope of the linear regression of the force deformation curve during the entire loading cycle.

To test the sticks, eighteen subjects were recruited to perform slap shots with each of the two sticks. Among the subjects, five subjects were female and thirteen subjects were male. Fourteen of the subjects (age =  $26.3 \pm 2.3$ ) were recreational players with relatively little sled hockey experience; the other four subjects were elite players from the WSF New York Sled Rangers. For the recreational group, tests were performed in a laboratory setting where the subjects performed a slapshot and shot the puck off of a high density polymer ethylene shooting pad. The subjects were required to sit in a hockey sled while taking the shot, in order to simulate on-ice conditions. Each subject performed three slapshots with each of the two sticks. The subjects were required to wait a minimum of 30 s between each shot and a shot was only considered valid if the subject was satisfied that they had produced a maximal effort. Testing

Table 2.2: Diagram of stiffness value for the flexible and rigid sled hockey sticks

Material	Loading	Stiffness (kN/m)
Wood		$(1.85 \pm 0.09) \times 10^2$
Wood		$(1.79 \pm 0.09) \times 10$
ABS		$(1.61 \pm 0.08) \times 10$
ABS		$(1.2 \pm 0.1)$

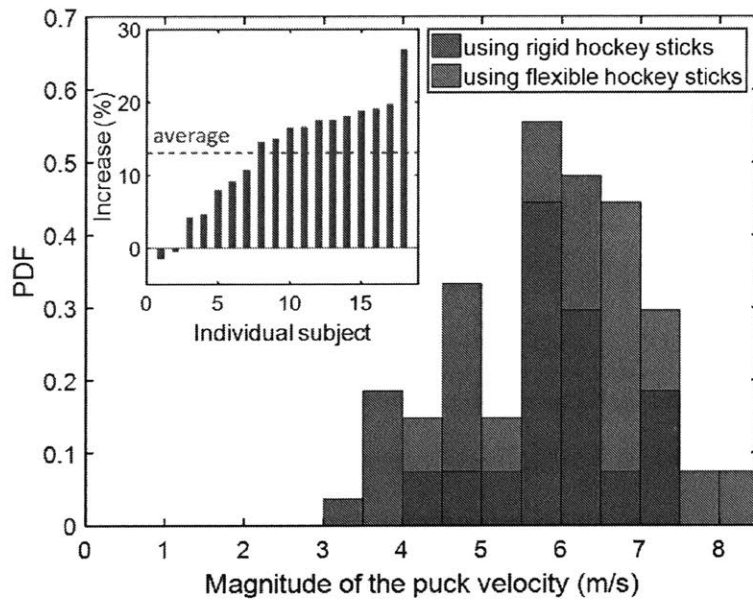


Figure 2-10: Histograms of the puck velocity for the rigid and flexible sled hockey sticks. Each histogram bar is normalized by the total number data points. (Inset) Percentage increase in puck velocity for each subject when using the flexible sled hockey stick. The dashed line indicates the average increase, 13.07 %. Subjects are shown in order of ascending percentage increase.

for the elite subjects were identical, however the tests were performed on a synthetic ice rink, with the subjects sitting in their personal hockey sleds, which they use for competitive events.

Prior to testing, each subject was given time ( $9.4 \pm 1.2$ ) min to get used to the experimental setting and the two types of sled hockey sticks. Especially for the flexible stick, players needed time to get used to and to take full advantage of its flexibility. The shooting pace was self-monitored by the subjects to minimize any fatigue effects. Seated rest periods and water breaks were provided whenever necessary. We used a camera (Canon EOS Rebel T6 Digital SLR) to videotape the shots, and the motion of the puck was then extracted using a custom MatLab script.

In Fig. 2-10, the puck velocities produced during the tests are plotted as a histogram. From the resulting distributions we see that the flexible stick provides a significant speed advantage. The average puck speed increase across all subjects is 13.07 %. For a very small number of subjects, the increase in puck speed is trivial or negative. One possible reason for this is that the increased flexibility sticks require players to modify their shooting strategy and some of the more experienced subjects may have had difficulty adapting to this.

Our model predicts that the puck speed  $V_p$  is linearly proportional to the peak force  $F_0$  that a player can produce. To test this, we used a force plate to roughly measure the force that each subject could produce after the subject finished the slap shots. Subjects were required to hold the sled hockey sticks at the same position as when they performed a slap shot to exert force on the plate using each type of sled hockey stick. This process was repeated five times for each subject.

In Fig. 2-11, we plot the shot speed of each subject against the average value of their measured force output. The resulting points are consistent with the predicted positive linear relationship. Using linear regression to fit lines to the data, we find correlation coefficients of 0.641 and 0.706 for the rigid and flexible sticks respectively.



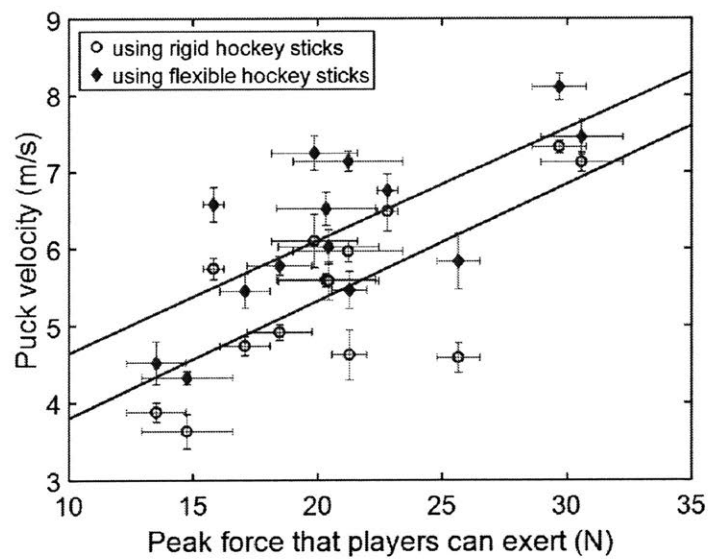


Figure 2-11: Puck velocity versus measured stick force for each subject. Linear curves of best fit are shown as solid lines. The puck velocity for each point corresponds to the mean value across three trials, and the peak force for each players corresponds to the mean of five measurements.

# Chapter 3

## Dynamics of Elastic Systems - Slap Shots

Hockey players decide how to shoot based on the circumstances surrounding the shot. If time is of the essence, a player may go for a quick wrist shot; however, if more power is required, a slapshot - wherein the player swings the stick down to strike the puck with as much force as possible — may be more ideal. In such a shot, the elasticity of the stick plays a crucial role in determining the final velocity of the puck. The physics of this process as it occurs in Olympic ice hockey has been studied experimentally, but no similar corpus of work exists for its adaptive, Paralympic counterpart, sled hockey. Furthermore, there has been no analytic work to describe the dynamics of the bending hockey stick in either context. The change in position, from stand-up on skates to sitting on a sled, drastically alters the shooting process. Shots in sled hockey are performed one-handed and consequently involve significantly lower swing forces. Despite this, current sled hockey sticks are designed with flexural stiffness values in the same range as standard hockey sticks. This makes it impossible to perform a proper slapshot, as the stick does not deflect sufficiently during the shooting motion. In the following study, we address this problem by developing a dynamic model to predict the optimal rigidity for performing a slapshot in both stand-up and sled hockey. Through experimental trials with amateur and elite sled hockey players, we find that our stick design provides an average shot speed increase of 10 % as compared

to commercially available options.

In Section 3.1, we introduce the concept of a slap shot in sled hockey and the relevant research in prior arts. In Section 3.2, we build two sets of dynamical models: one is based on the Euler-Bernoulli beam model in the continuous domain; the other is based on a 1-DOF mass-spring-damper system in the discrete domain. We find the optimal Young's modulus of the stick material and conduct experiments elaborated in Section 2.3. In Section 2.2, we propose numerical solvers for the continuous model accounting for the non-linear dynamics.

### 3.1 What is Slap Shot

Hockey players choose their techniques based on the timing, intent, and position of the shot in question [51, 52]. Generally speaking, players tend to opt for the 'slapshot' if they seek to impart the most velocity onto the puck. The slapshot motion typically involves raising the stick up behind the head and then swinging it down to strike the puck with as much force as possible [3, 53]. Using this technique, elite athletes can produce puck velocities in excess of 80 mph (35 m/s) [3, 53]. The highest recorded slapshot speed is that of Zdeno Chara, who achieved a puck velocity of 108.8 mph (48.9 m/s) during the 2012 NHL All-Star Skills Competition [54].

In general, a stand-up slap shot can be broken down into five distinct stages: backswing, downswing, stick preload, puck impact and puck release [51, 52] (see Fig. 3-1). During the backswing and downswing stages, the player raises the stick backwards to wind up for the shot and then rapidly swings it forwards towards the puck. The preload stage begins when the stick impacts the ice; during this stage, the player flexes the stick into the ice, imbuing it with the elastic energy. During the puck impact stage, the blade of the stick contacts the puck and transfers its stored energy to the puck. Finally, during the puck release stage, the puck leaves the stick's blade and travels away at a near-constant velocity [51, 52].

In the following study, we develop a dynamical model of the slap shot process. Through comparison with experimental data, we show that our model is capable of

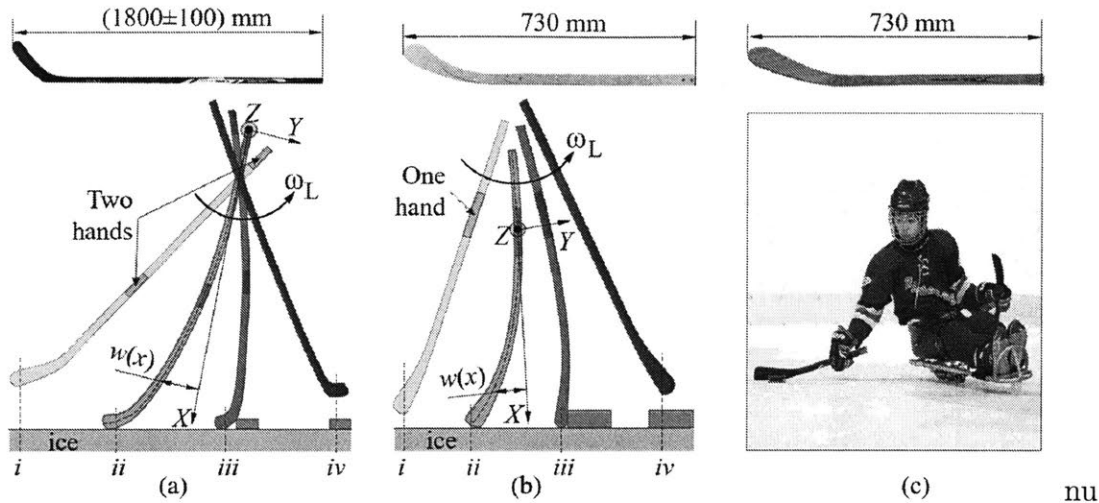


Figure 3-1: (a) Schematic of a stand-up hockey slap shot. (b) Schematic of a sled hockey slap shot using our prototype sled hockey stick. The flexibility is increased by using ABS plastic in place of wood. (c) Photograph of a sled hockey player using the conventional wooden sled hockey stick [1]. (Photograph credit John Freidah) The puck is highlighted in green. *i*: Backswing/Downswing; *ii*: Stick preload; *iii*: Puck impact; *iv*: Puck release.

predicting puck velocity from swing speed and stick rigidity. We then apply our model to design improved hockey sticks for a popular ice hockey variant, known as sled hockey. Sled hockey is a hockey alternative for people with limited leg mobility. In sled hockey, players sit on a sled outfitted with narrow blades underneath and propel themselves along the ice using a pair of half-length sticks [55, 20], as shown in Fig. 3-1 (c). Each stick has a metal cleat on one end, to grab the ice while pushing the sled, and a wooden blade on the other end, for handling the puck. This difference in form dramatically changes the physics involved in making a shot, as they are performed with only one arm and therefore tend to be significantly less powerful. Despite this, sled hockey sticks are currently designed with flexural stiffness values in the same range as those of standard hockey sticks. This makes it near-impossible to perform a proper slapshot, as the stick does not deflect to a sufficient degree during the shooting process. We address this problem by applying our model to design an improved sled hockey stick with optimal stiffness properties. Through experimental trials with amateur and elite sled hockey players, we find that our stick design provides an average shot speed increase of 10 % relative to the designs currently in use.

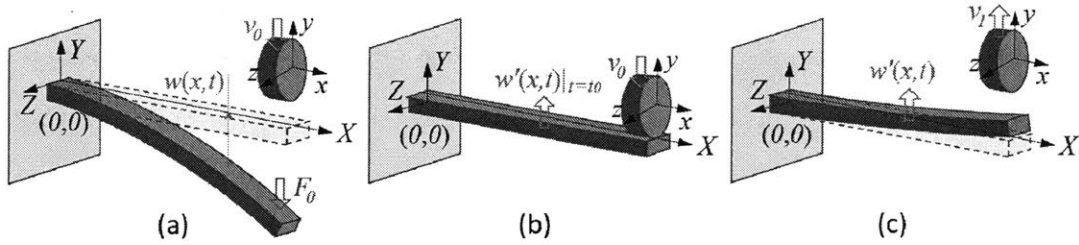


Figure 3-2: Schematic of our Euler-Bernoulli beam model of a sled hockey slap shot. (a) Stick preload; (b) Puck impact; (c) Puck release.

In terms of previous work, there are relatively few studies specific to sled hockey. However, there are a great number of experimental studies on the role of stick stiffness in stand-up hockey shots [51, 52, 3, 53, 2, 50, 56, 57, 58, 59, 60, 61, 62, 63]. Interestingly, there's relatively little consensus in this literature on the exact relationship between stick stiffness and shooting performance. For instance, Pearsall *et. al* reported that low stiffness sticks produce the fastest slapshot puck speeds for elite players [3], whereas Wu *et. al* found that puck speed and stick stiffness exhibit no clear relationship [51], and Worobets *et. al* found that stick stiffness can influence puck speed for wrist shots, but not for slap shots [2].

To the best of our knowledge, there is no previous work analytically modelling slapshot mechanics from a theoretical perspective [64, 65]. In view of this, the model developed here represents a first attempt to tackle the problem from a more fundamental perspective. We apply the insights afforded by our analytic approach to potentially offer greater insight as to the contradictory conclusions of previous works.

## 3.2 Dynamical Modelling and Parametric Optimization

### 3.2.1 Continuous Euler-Bernoulli Beam Model

In previous work on sports such as badminton [66, 67], baseball [68, 69, 70], and tennis [71, 72, 73, 74, 75], an Euler-Bernoulli beam model is widely used to model the

elastic response of the striking implement [76]. We adopt a similar approach here, developing a mathematical model to characterize the behavior of a hockey stick as it impacts the puck, and then applying this model to investigate the dynamic response of the stick throughout a slapshot.

As shown in Fig. 3-2, we approximated the hockey stick as a cantilevered EB beam. The shape of the beam is described by the function  $w(x, t)$ , defined within a non-inertial coordinate system  $XYZ$ , which is fixed at the beam's supported end. We used this dynamical model for the last three distinct stages of the shooting process (stick preload, puck impact, and puck release). As shown in Fig. 3-2, the stick begins the preload stage in a deflected position, where the deflection of the beam is induced by a point load at its free end. This load represents the force of the ice on the stick prior to the puck impact. The shape of the preloaded beam is determined as follows [77]:

$$-EI_{zz}(x)\frac{\partial^2 w(x)}{\partial x^2} = -F_0L + F_0x, \quad (3.1)$$

where  $E$  is the Young's modulus of stick,  $I_{zz}(x)$  is the second moment of inertia of the stick cross-section,  $F_0$  is the point load, and  $L$  is the stick's length. To model the movement of the stick during this stage, we considered the problem in a reference frame  $XYZ$  such that the beam is static and the puck moves towards the beam with a velocity  $\bar{v}_0 = \bar{\omega}_L \times \bar{x}_0$ , defined as the cross product of the angular velocity at which the player swings the stick,  $\bar{\omega}_L$ , and the location of the puck impact,  $\bar{x}_0$ .

The impact phase is initiated by removing the preloading force  $F_0$ , causing the beam to snap forwards and strike the puck. During the stick-puck collision, the puck is modelled as a cylindrical rigid body, and the impulse force between the puck and the beam is modelled as a Gaussian pulse in space,  $x$ , and time,  $t$ . Based on this, the dynamic response of the beam is modelled as follows [78, 77, 79, 80, 81, 82, 83]:

$$\rho A(x)\frac{\partial^2 w(x, t)}{\partial t^2} + \frac{\partial^2}{\partial x^2}(EI_{zz}(x)\frac{\partial^2 w(x, t)}{\partial x^2}) = Q\frac{e^{-\frac{(x-x_0)^2}{2\sigma_x^2}}}{\sqrt{2\pi\sigma_x^2}}\frac{e^{-\frac{(t-t_0)^2}{2\sigma_t^2}}}{\sqrt{2\pi\sigma_t^2}}, \quad (3.2)$$

where  $\rho$  is the density of the material of the beam,  $A(x)$  is the cross-sectional area

of the beam as a function of  $x$ ,  $Q$  is the magnitude of the Gaussian force,  $x_0$  and  $t_0$  are the position and time of the collision respectively, and  $\sigma_x$  and  $\sigma_t$  are the standard deviations of the Gaussian force in the spatial domain and in the temporal domain respectively.

During the collision, the change in the momentum of the puck is given by the double integral of the Gaussian force over  $x$  and  $t$ . Based on the conservation of momentum, this gives us the following equation:

$$M_p v_1 - M_p v_0 = \iint Q \frac{e^{-\frac{(x-x_0)^2}{2\sigma_x^2}} e^{-\frac{(t-t_0)^2}{2\sigma_t^2}}}{\sqrt{2\pi\sigma_x^2} \sqrt{2\pi\sigma_t^2}} dx dt, \quad (3.3)$$

where  $M_p$  is the mass of the puck, and  $v_0$  and  $v_1$  are the velocity of the puck before and after the collision respectively. The double integral can be shown to be equal to  $Q$ , the magnitude of the Gaussian distributive force.

To complete our system of equations, we consider the conservation of energy before and after the puck impacts the stick. Before the impact, the total energy in the system is given by the potential energy associated with the preloaded deflection of the stick and the kinetic energy of the puck travelling at velocity  $v_0$ . In the moment after the collision, we assume that the transverse deflection of the beam is approximately zero such that total energy of the system is given by the sum of the kinetic energies of the beam and of the puck, now travelling at velocity  $v_1$ , as shown in Fig. 3-2 (b). This yields the following energy conservation equation [84, 85, 86, 86]:

$$\begin{aligned} & \frac{1}{2} M_p v_0^2 + \int_0^L \left[ \frac{1}{2} E I_{zz}(x) \left( \frac{\partial^2 w(x, t)}{\partial x^2} \right)^2 \right]_{t=-\infty} dx \\ & = \frac{1}{2} M_p v_1^2 + \int_0^L \left[ \frac{1}{2} \rho A(x) \left( \frac{\partial w(x, t)}{\partial t} \right)^2 \right]_{t=3\sigma_t} dx, \end{aligned} \quad (3.4)$$

where the beam's boundary conditions are given as:

$$\begin{aligned}
w(0, t) &= 0, \\
w'(0, t) &= 0, \\
-EI_{zz}w''(L, t) &= 0, \\
-EI_{zz}w'''(L, t) &= 0.
\end{aligned} \tag{3.5}$$

To solve this system of four differential equations presented above, we performed a modal decomposition. Since the distributed-parameter system has infinitely many vibrational modes, the general response is a superposition of the response from all modes [86, 86]. Thus, the response of the beam during the collision stage can be expressed as:

$$w(x, t) = \sum_{j=1}^{\infty} \phi_j(x)u_j(t), \tag{3.6}$$

with  $\phi_j$  and  $u_j$  being given respectively as:

$$\phi_j(x) = (\sin(\lambda_j x) - \sinh(\lambda_j x)) - \frac{\sin(\lambda_j L) + \sinh(\lambda_j L)}{\cosh(\lambda_j L)} (\cos(\lambda_j x) - \cosh(\lambda_j x)), \tag{3.7}$$

$$u_j(t) = \frac{Q\phi_j(x)}{\omega_j \rho A \int_0^L \phi_j^2(x) dx} \int_0^L a_j(x) \frac{e^{-\frac{(x-x_0)^2}{2\sigma_x^2}}}{\sqrt{2\pi\sigma_x^2}} dx \psi_j(t), \tag{3.8}$$

where  $\omega_j$  is the natural frequency of the  $j$ -th mode,  $a_j(x)$  is the mode shape of the  $j$ -th mode, and  $\psi_j(t)$  is denoted as the following for brevity:

$$\psi_j(t) = \sin(\omega_j t) \int_0^t \cos(\omega_j t) \frac{e^{-\frac{(t-t_0)^2}{2\sigma_t^2}}}{\sqrt{2\pi\sigma_t^2}} dt + \cos(\omega_j t) \int_0^t \sin(\omega_j t) \frac{e^{-\frac{(t-t_0)^2}{2\sigma_t^2}}}{\sqrt{2\pi\sigma_t^2}} dt. \tag{3.9}$$

The puck velocity after the collision,  $v_1$ , is solved for by combining the momentum and energy conservation equations. The resulting puck velocity in the inertial frame  $V_p$  is equal to the sum of  $v_1$  and  $v_0$ .  $V_p$  can be decomposed into two parts: the component  $V_{kin}$ , resulting from the kinetic energy of the swinging beam, and an elastic component,  $V_{pot}$ , resulting from the potential energy stored in the beam during the



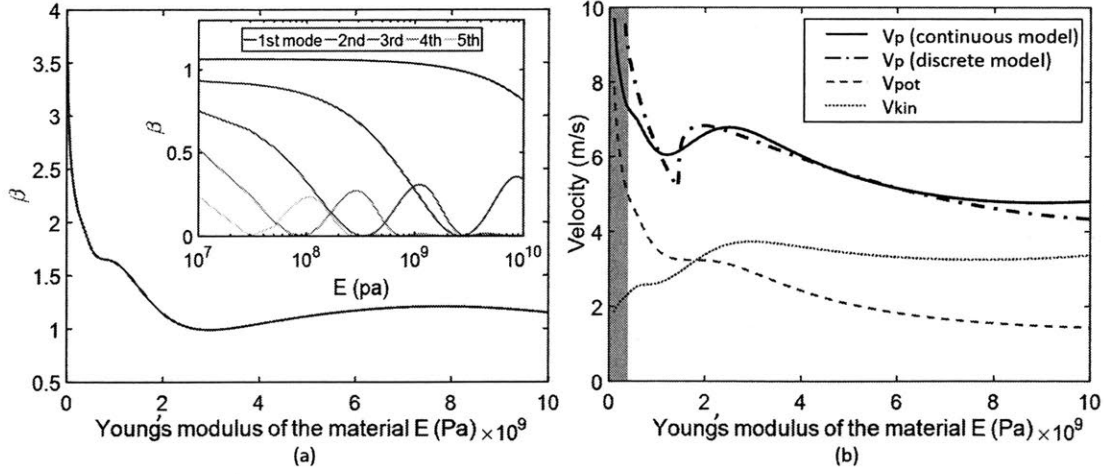


Figure 3-3: (a)  $\beta$  plotted as a function of the Young's modulus of the beam material,  $E$ . (Inset) The contribution of the first five mode shapes to the net value of  $\beta$ . (b) Puck velocity  $V_p$  plotted as a function of the Young's modulus of the beam material. Solid and dash-dot lines correspond to the continuous and discrete models respectively. The colored dashed and dotted lines plot the contributions of the elastic and kinetic energy to the overall puck velocity ( $V_{pot}$  and  $V_{kin}$  respectively). The shaded area highlights conditions where the stick deflection is large and our linear model may not be valid.

preload stage:

$$V_p = \underbrace{\frac{2}{1+2\beta}\Omega_L x_0}_{V_{kin}} + \underbrace{\frac{2}{1+2\beta}\frac{\partial w(x,t)}{\partial t}\bigg|_{t=t_0, x=x_0}}_{V_{pot}}. \quad (3.10)$$

$V_{pot}$  is calculated by using the modal decomposition method to determine the natural response of the beam given its initial deflection at  $x = x_0$  and  $t = t_0$ . The dimensionless coefficient  $\beta$  is given by:

$$\beta = \frac{M_p}{2\rho A} \sum_{j=0}^{\infty} \left\{ \frac{1}{\int_0^L \phi_j^2(x) dx} \left[ \int_0^L \phi_j(x) \frac{e^{-\frac{(x-x_0)^2}{2\sigma_x^2}}}{\sqrt{2\pi\sigma_x^2}} dx \right]^2 \psi_j^2(t)\bigg|_{t=3\sigma_t} \right\}. \quad (3.11)$$

Physically,  $\beta$  may be interpreted as the ratio of the total energy stored in the beam to the total energy transferred to the puck. In the case of an infinitely large, completely rigid beam, the velocity of the puck is twice that of the beam, given that the puck is initially stationary.

In Fig. 3-3, we simulate slap-shots with sticks of varying stiffness. The dimensions

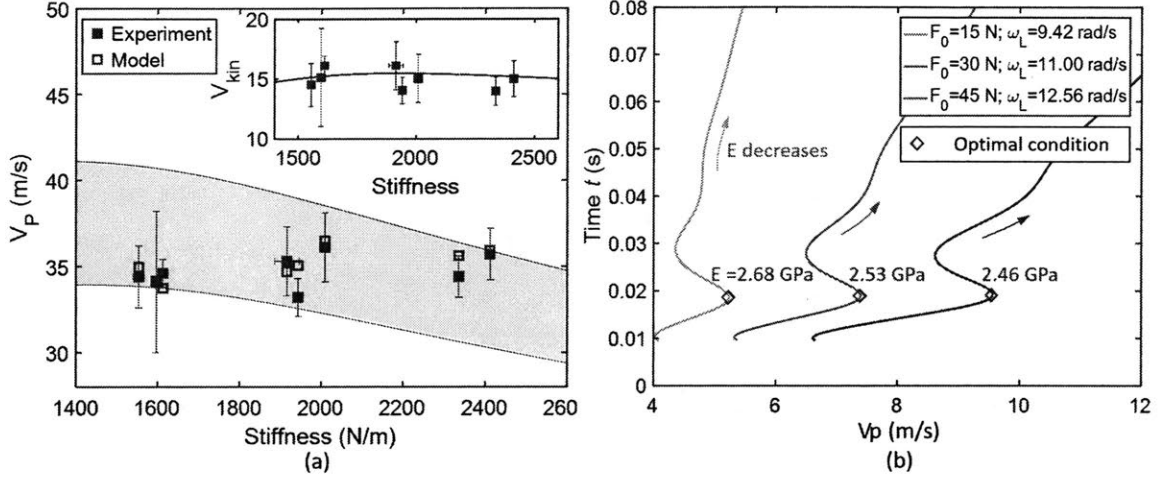


Figure 3-4: (a) We compare the predicted puck speed,  $V_p$  (m/s) of our model with experimental data on stand-up slapshots over a range of stick stiffness values. Data is sourced from [2]. Within the the experimental data, the loading force varies significantly between shots. The shaded region corresponds to predicted puck speeds  $V_p$  for the range of forces observed in [2]. (Inset)  $V_{kin}$  (m/s) plotted as a function of the stiffness (N/m).  $V_{kin}$  is calculated by removing  $V_{pot}$  from both the model and experimental puck velocities. (b) Time  $t$  (s) to perform a slap shot as a function of the puck speed  $V_p$  (m/s). Arrows indicate directions of decreasing Young's modulus  $E$ . The diamond markers delineate the optimal conditions labelled with the corresponding optimal Young's modulus  $E$ .

of the stick are assumed to be constant and the stiffness is controlled by varying the Young's modulus of the stick material. We include the first forty eigenmodes in our simulation of the stick's response. As shown in Fig. 3-3, as the Young's modulus of the material decreases,  $\beta$  generally increases, indicating that more vibrational energy is stored in the beam instead of transferring to the puck during the collision stage.  $\beta$  does not increase monotonically; this is because certain eigenmodes are depressed or excited during the collision, depending on the stiffness of the beam relative to the timescale and spatial distribution of the impact force.

As shown in Fig. 3-3 (b), as the Young's modulus decreases, the magnitude of the velocity of the puck increases, with a local maximum around  $E = 2.3$  GPa. The two components of the puck velocity,  $V_{kin}$  and  $V_{pot}$ , explain this tendency. Given that  $\Omega_L \times L$  is constant,  $V_{kin}$  is inversely proportional to  $\beta$ , so as  $E$  decreases,  $V_{kin}$  decreases with a maximum around 2.3 GPa where  $\beta$  has a local minimum.  $V_{pot}$  is also inversely

proportional to  $\beta$ , but as  $E$  decreases there will be more energy stored in the beam during the preload stage. The increased potential energy exceeds the influence of  $\beta$ , so as  $E$  decreases,  $V_{pot}$  increases. As  $E$  further decreases below around 0.5 GPa, the deflection of the beam becomes large and our Euler-Bernoulli beam may no longer be valid. This region is highlighted by the shaded area in Fig. 3-3.

To test our model, we compared it with experimental data on stand-up hockey slapshots. In stand-up hockey, players use two hands to perform a slapshot, a detail not represented within our model. However, data on single-handed sled hockey slapshots is not available, meaning we must use stand-up data to provide a rough comparison. In Fig. 3-4 (a), we plot the puck speeds predicted by our model alongside experimentally observed puck speeds from a previous study [2]. Despite the model's significant simplifications, we find that the predicted puck velocities show good agreement with experimental results. For each data point, the stick stiffness and loading force reported in [2] are used as inputs to our model. The angular speed of the stick,  $\omega_L$ , is required as a third input to our model, but is not reported in [2]. Based on this, we applied constant nominal values across all data points. We find that the predicted and observed velocities are closest for  $\omega_L = 14.14$  rad/s, which is consistent within swing speeds observed in the previous work [3].

Within the experimental data, the loading force on the stick varies substantially between shots, ranging from 284 N to 390 N [2]. As shown by the shaded region in Fig. 3-4, this variation in force can strongly influence the final speed of the puck and must be accounted for to accurately predict shot speed. Variations in loading force may contribute to the conflicting results of previous studies on the relationship between stick stiffness and shot speed [3, 2]. If the stick force is not accounted for, variations in its value can significantly impact the observed stiffness-speed relationship.

To further investigate the relationship between the stick stiffness and the slap-shot performance, we consider a second metric: the time used to perform the shot,  $t$ . In Fig. 3-4 (b), we evaluate  $t$  and  $V_p$  over a range of stick stiffness for three combinations of force  $F_0$  and stick speed  $\omega_L$ . As shown by the resulting curves, as  $E$  decreases,  $V_p$

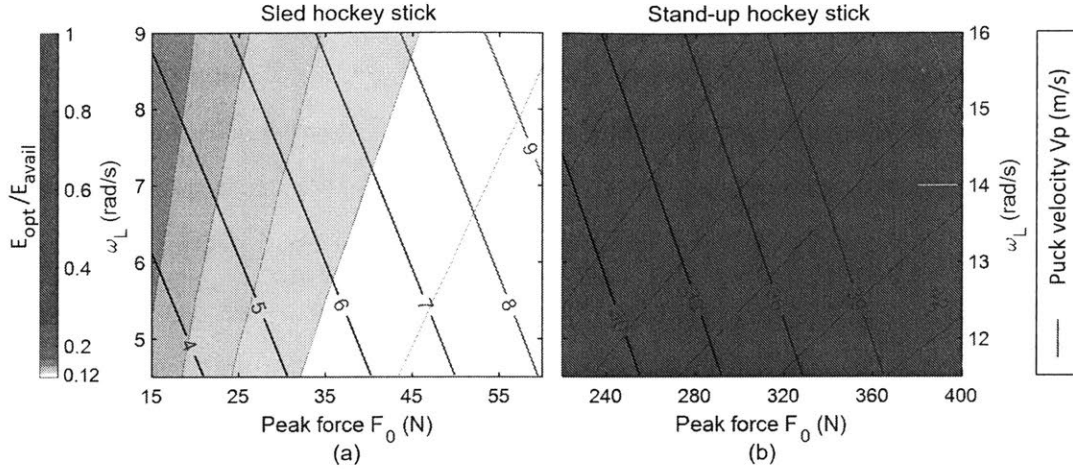


Figure 3-5: The ratio of the optimal Young’s modulus of the stick material to the available Young’s modulus,  $E_{opt}/E_{avail}$  for sled hockey sticks (a) and for stand-up hockey sticks (b). The color map is in logarithmic scale. The ranges of the peak force  $F_0$  for sled hockey and stand-up hockey are 15 N to 60 N and 230 N to 400 N respectively [2]; the ranges of the angular speed  $\omega_L$  are 4.5 rad/s to 9 rad/s and 8.5 rad/s to 13 rad/s respectively [3].

reaches a local maximum at time  $t \approx 0.02$  s and a local minimum at  $t \approx 0.03$  s; as  $E$  decreases further,  $V_p$  slowly increases but  $t$  increases dramatically. Based on this, for each combination of the force and the stick speed, optimal values of the stick stiffness,  $E$ , are delineated by diamond markers within the figure.

Optimal stick stiffness varies based on the peak force  $F_0$  and the swing speed  $\omega_L$ . These variables are both a function of a given player’s physical condition, and consequently players will perform best with a stick stiffness tuned to their own personal capabilities. In Fig. 3-6, we plot the optimal Young’s modulus of the stick material,  $E$  for  $F_0$  and  $\omega_L$  ranges relevant to both sled hockey and stand-up hockey. As shown in Fig. 3-6, the optimal stick stiffness decreases as the peak force increases. Physically, this means that if a player can exert a higher force, they can impart a greater velocity to the puck through the elastic velocity component  $V_{pot}$ . In addition to this, the results presented within the plots highlight the need to reconsider the design of conventional sled hockey sticks. In practice, the range of stiffness for commercially available hockey sticks is roughly the same for the stand-up and sled versions of the sport. In contrast to this, the plots show that the optimal stick stiffness for sled

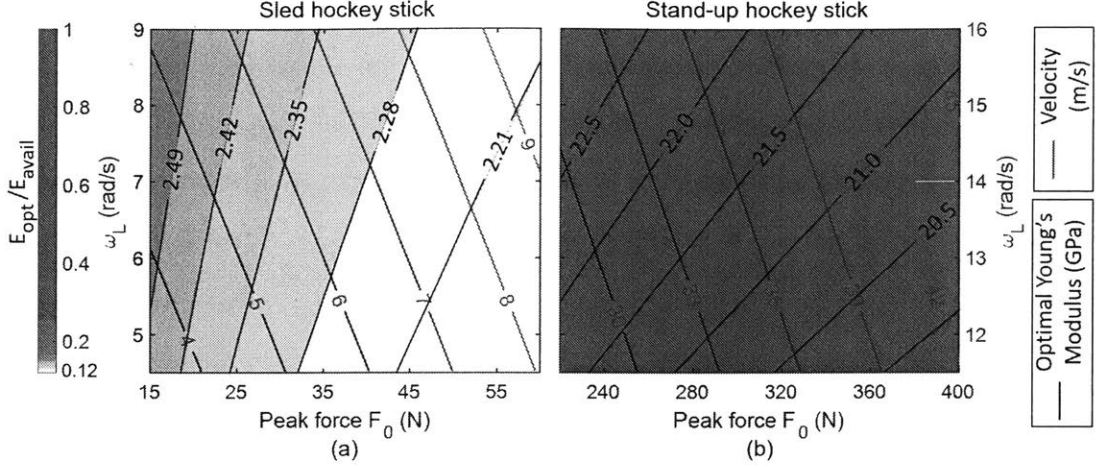


Figure 3-6: The ratio of the optimal Young’s modulus of the stick material to the available Young’s modulus,  $E_{opt}/E_{avail}$  for sled hockey sticks (a) and for stand-up hockey sticks (b). The color map is in logarithmic scale. The ranges of peak force  $F_0$  for the sled hockey and stand-up hockey are 15 N to 60 N and 230 N to 400 N respectively [2]; the ranges of the angular speed  $\omega_L$  are 4.5 rad/s to 9 rad/s and 8.5 rad/s to 13 rad/s respectively [3].

hockey is roughly an order of magnitude lower than that of stand-up hockey.

### 3.2.2 Discrete Mass-Spring-Damper Model

In the following section, we develop a discrete representation of the beam-puck system. This simplified approach reduces the continuous beam system to a more tractable model with one degree of freedom [76]. As shown in Fig. 3-7, the puck and the hockey stick are modelled as rigid bodies with a linear spring attached to the ‘stick’ body. The potential energy stored in the continuous Euler-Bernoulli model is represented by the elastic energy stored in this spring.

We utilize the same three stages to describe a slap shot in the discrete model. During the preload stage, a force  $F_0$  is applied to the stick and compresses the linear spring. The stored potential energy is given as  $F_0^2/(2k)$ . After the preload stage, the governing equation for the motion of the stick mass can be expressed by a non-homogeneous second-order ODE:

$$M_s \frac{d^2 y_s}{dt^2} + c \frac{dy_s}{dt} + k y_s = \text{sgn}\left(-\frac{dy_s}{dt}\right) \mu_s M_s g, \quad (3.12)$$

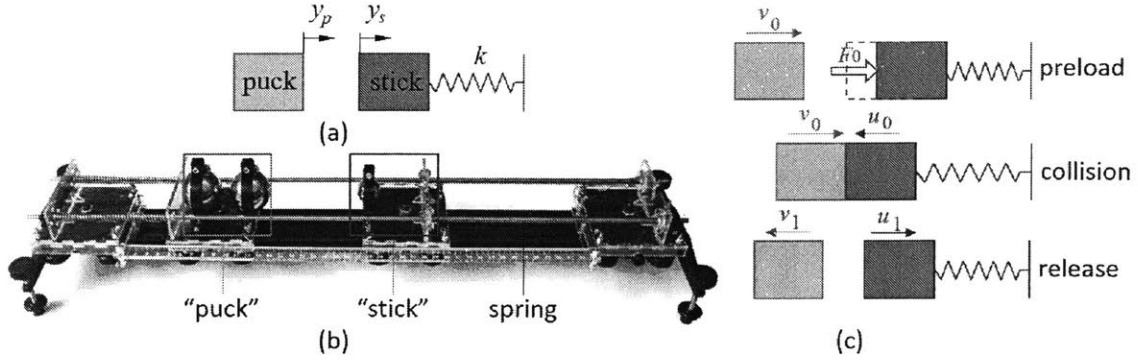


Figure 3-7: (a) Discrete model. (b) Experimental setup. (c) Discrete model for three stages of a slap shot.  $dy_p/dt$  at  $t = t_c^-$  and  $t = t_c^+$  are denoted as  $v_0$  and  $v_1$  respectively;  $dy_s/dt$  at  $t = t_c^-$  and  $t = t_c^+$  as  $u_0$  and  $u_1$  respectively.

where  $y_s$  is the displacement of the stick,  $M_s$  is the effective mass of the stick,  $c$  is the damping ratio,  $k$  is the stiffness of the spring, and  $\mu_s$  is the coefficient of friction, which characterizes frictional energy loss between the stick and the slider.

During the collision stage, the energy conservation is described by the following equation [87, 88]:

$$(1 - e) \left( \frac{1}{2} M_s \left( \frac{dy_s}{dt} \right)^2 + \frac{1}{2} M_p \left( \frac{dy_p}{dt} \right)^2 \right) \Big|_{t=t_c^-} = \left( \frac{1}{2} M_s \left( \frac{dy_s}{dt} \right)^2 + \frac{1}{2} M_p \left( \frac{dy_p}{dt} \right)^2 \right) \Big|_{t=t_c^+}, \quad (3.13)$$

where  $e$  represents the coefficient of energy loss during the collision, and  $t_c^-$  and  $t_c^+$  represent instants in time immediately before and after the collision occurs respectively.

During the release stage, the dynamics of the puck can be simply described by the conservation of linear momentum:

$$M_p \frac{d^2 y_p}{dt^2} = \text{sgn} \left( -\frac{dy_p}{dt} \right) \mu_p M_p g, \quad (3.14)$$

where  $y_p$  is the displacement of the puck,  $M_p$  is the mass of the puck, and  $\mu_p$  is the Coulomb friction coefficient between the puck and the slider.

To test our discrete model, we built an experimental setup, as shown in Fig. 3-7. The setup consists of two steel spheres which serve as a 'puck' body ( $M_p = 0.71 \text{ kg}$ ),

and a 'stick' body ( $M_s = 0.29 \text{ kg}$ ). The movement of the spheres is constrained by a low-friction linear rail and a linear spring is used to connect the stick mass to a fixed end of the rail. We used a high-speed camera (Phantom Miro M320S; resolution:  $768 \times 576$ ; sample rate: 1000 pps; exposure time:  $990 \mu\text{s}$ ) and a custom MatLab script to record the motion of the masses throughout a collision event.

To simulate a slapshot, the linear spring is compressed with a constant load  $F_0$  and the 'puck' and 'stick' masses are then launched towards one another. The initial conditions of the launch are chosen such that puck-stick collision coincides with the instant when the stick spring reaches its unloaded length. In Fig. 3-8 we compare the output of our discrete model with an example collision, recorded using our experimental setup. From the resulting curves we see that the experiment and theoretical model agree closely with one another.

To explore the optimal stiffness of the linear spring, we assume the 'puck' mass and the 'stick' mass to be constant, and then calculate the resulting puck velocity for a range of different spring stiffness values. These stiffness values can be converted to an effective Young's modulus for the continuous model  $E = kx_0^3/(3I_{zz})$ . In Fig. 3-3, we compare the stiffness-speed relationship of our discrete model with that of the full continuous model.

### 3.3 Conclusion and Future Work

Through our analysis, we have shown that it is possible to capture the basic dynamics of a sled hockey slapshot using a reduced dynamic model of the stick-puck collision process. We applied this model to study the relationships between the swing speed, stick loading force, stick elasticity, and the resultant puck speed. Based on our investigation, we found that the stiffness of commercially-available sticks for stand-up hockey sticks is consistent with the optimal range predicted by our model, while that of commercially-available sled hockey sticks is roughly one-order of magnitude above its optimal value. Based on this, we designed and tested a prototype of sled hockey stick with optimal stiffness properties. Throughout testing with both elite and ama-

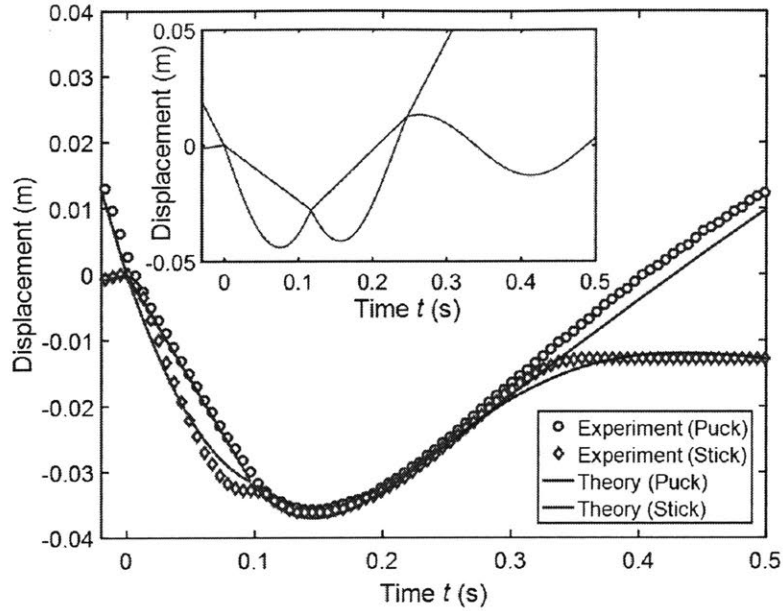


Figure 3-8: Comparison of theoretical and experimental mass displacements for our discrete collision model. (Inset) Theoretical results for the case of zero energy loss.

teur sled hockey players, we found that final puck velocities with our prototype stick were on average 13.07% higher as compared to those achieved with commercially available sticks. In terms of the future work, there are a number of avenues which could be explored. It may be possible to further improve the performance by varying the stick's cross-sectional shape and material properties along its length. In addition, it could also prove fruitful to consider blade and stick curvature effects, which are not accounted for in the present model.





# Chapter 4

## Dynamics of Elastic Systems - Wrist Shots

The increasing popularity of sled hockey in the community of people with physical disabilities requires an improvement in the safety and performance of sled hockey. In particular, wrist shots serve as one of the most widely performed shots. Understanding the mechanism of sled hockey sticks in wrist shot is significant for the design and manufacturing of more reliable sled hockey sticks, and thereby improving the performance and experience of sled hockey for people with physical disabilities.

In this chapter, we investigate a dynamical model to simulate the dynamics of a wrist shot and explore the optimal flexural rigidity of a sled hockey stick. In our simulation, we model the dynamics of a wrist shot by utilizing an Euler-Bernoulli cantilevered beam model with a cylindrical rigid body attached to its distal end. This dynamic system is governed by a 4th-order PDE. We solve for the transverse deflection of the beam and the puck motion applying a modal decomposition method. Based on the simulation results and the constraint in shooting mode and driving mode respectively, a more flexible sled hockey stick is proposed and verified. In particular, the optimal flexural rigidity can be determined by the compromise of maximizing the magnitude of the puck velocity in the shooting mode and maximizing the feasibility of propulsion in the driving mode.

Remarkably, a significant improvement is achieved in terms of the magnitude of

the puck velocity with the improved hockey stick; our experiments show an average of 11.48% increase in the puck speed. we also find a moderate positive linear relationship between the peak force that players can exert and the magnitude of the puck velocity.

## 4.1 What is Wrist Shot

Sled hockey, also known as para ice hockey, is a newer sport than standing hockey. Sled hockey was invented in the 1960s in Sweden, which is designed for people with physical disabilities, and it became an official event in Paralympic games in 1994 [89, 17]. Athletes sit in a sled and use a pair of sled hockey sticks to drive themselves in the ice rink. The sticks are applied for two essential functions. First, athletes drive the sled by pushing off the ice with the sticks. Second, athletes use the sticks to make contact with the puck, maneuvering it and shooting it. These two uses of sled hockey sticks will be referred to as the shooting mode and the driving mode respectively.

The most common shot in sled hockey is the wrist shot, where the stick is preloaded (forced to bend by the ice) and unloaded in constant contact with the puck. Given the important role of sticks, a careful design and selection on the stiffness of sled hockey sticks is required. Indeed, the stiffness of standing hockey sticks has been studied in a wide range of research [56, 3]. However, to the best of our knowledge, rare study has been done on the stiffness of sled hockey sticks [2]. For standing hockey, the literature suggests that more flexible hockey sticks produce higher puck speeds in wrist shots. An optimal stiffness for standing hockey sticks based on athlete weight has been proposed and is quite commonly used in stick selection [2, 60].

Nonetheless, the stiffness designed for standing hockey sticks is not feasible in sled hockey stick selection. At first, the wrist shot is less powerful than shots seen in standing hockey [2]. Two primary reasons may account for this: (i) in sled hockey, only one hand is used to apply a force and a torque to the stick, transmitting less power to the shot; (ii) the overall flexural rigidity of sled hockey sticks are much higher than that of standing hockey sticks. Less flexible sticks are unable to store and transmit as much elastic potential energy as more flexible sticks, making sled

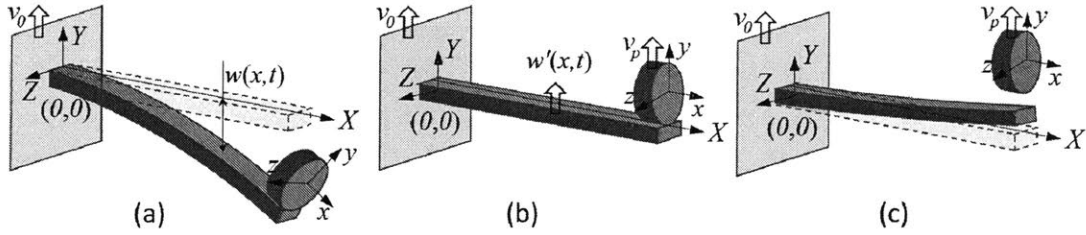


Figure 4-1: Schematic of the Euler-Bernoulli beam model for a sled hockey stick and a rigid body model for a puck. (a) Preload stage; (b) Release; (c) Post-Release stage.

hockey sticks less powerful. In addition, because sled hockey sticks are also used for driving the sled in the ice rink, the stiffness of the stick should not solely be based on its performance in shooting. Finally, the materials and methods used to make standing hockey sticks are easily adapted to the design and manufacturing of sled hockey sticks, though these processes are not optimal for sled hockey. Given these conditions, manufacturers make very rigid sled hockey sticks, with a typical stiffness around 150 kN/m. In order to provide guidance to the design and manufacture of sled hockey sticks, and also to help players in stick selection, we employ a dynamical model to simulate the wrist shot and probe the optimal flexural rigidity of the sled hockey stick.

## 4.2 Dynamical Modelling and Parametric Optimization

Slender rigid body and Euler-Bernoulli beam model are extensively used to study the dynamics of racket sports, like badminton [66], baseball [68, 76] and tennis [71]. This model describes the potential energy stored in the sled hockey stick, we propose an Euler-Bernoulli beam model to investigate the dynamic behavior of a sled hockey stick in the wrist shot. The hockey stick is modelled as a cantilevered Euler-Bernoulli beam with travelling speed  $v_0$  at its cantilevered end. After the sled hockey stick contacting with the puck, the system is modelled as a cantilevered Euler-Bernoulli beam with a cylindrical rigid body attached to its distal end as shown in Fig. 4-1.

The current commercially-available sled hockey stick is about 800 mm in length with a rectangular cross-section (30 mm by 18 mm) and we also can observe a curved, thin region at the end. In the simplified model, we neglect the detailed variation and assume the stick is rectangular beam with a uniform cross-section of these dimensions. Since both a force and a torque are exerted on the sled hockey sticks at the same time, the beam is modelled to be cantilevered. As shown in Fig. 4-1 (a), the wrist shot requires the sled hockey stick to be preloaded by a force, while the sled hockey stick and the puck remain static and contact. Potential energy is stored in the sled hockey stick during this stage. When the sled hockey player releases the hockey stick, the stick accelerates and the puck remains contact with the stick and accelerate at the same velocity as that of the distal end of the sled hockey stick. Once the stick starts to decelerate due to its bending, the puck will detach the stick (Fig. 4-1 (b)) and remain the velocity until the friction between the puck and ice decelerate it during stage (Fig. 4-1 (c)). The governing equation for the transient dynamics of an Euler-Bernoulli beam is the 4th-order non-homogeneous PDE [71, 77]:

$$\rho A \frac{\partial^2 w(x, t)}{\partial t^2} + \frac{\partial^2}{\partial x^2} \left( EI_{zz}(x) \frac{\partial^2 w(x, t)}{\partial x^2} \right) + b \frac{\partial^5 w(x, t)}{\partial x^4 \partial t} = q(x, t), \quad (4.1)$$

where  $w(x, t)$  is the transverse deflection of the beam,  $E$  is the Young's modulus of the material,  $I_{zz}(x)$  is the second moment of inertia of the cross-section of the beam with respect to  $Z$ -axis, the cross-section of which is constant in this model,  $\rho$  represents the density of the material,  $A$  is the cross-sectional area of the beam,  $b$  represents the damping ratio and the  $q(x, t)$  represents the spatial and temporal distribution of the force applied, which will be zero in our model. The four boundary conditions for this beam are:

$$\begin{aligned} w(0, t) &= 0, \\ w'(0, t) &= 0, \\ -EI_{zz}w''(L, t) &= I_p \frac{\partial^3 w}{\partial t^2 \partial x}, \\ -EI_{zz}w'''(L, t) &= M_p \frac{\partial^2 w}{\partial t^2}, \end{aligned} \quad (4.2)$$

where  $I_p = I_{p_{zz}} + M_p L^2$  represents the moment of inertia of the puck with respect to  $Z$ -axis,  $M_p$  is the mass of the puck and  $L$  is the length of the beam.

A modal decomposition method is applied to solve the PDE in Equation 4.1.  $\lambda_j$  for each eigenmode can be obtained by solving by the following equation according to the boundary conditions:

$$1 + \cos \lambda_j \cosh \lambda_j + \frac{M_p \lambda_j}{\rho A L} (\cos \lambda_j \sinh \lambda_j - \sin \lambda_j \cosh \lambda_j) - \frac{L \lambda_j^3}{\rho A L^3} (\cosh \lambda_j \sin \lambda_j + \sinh \lambda_j \cos \lambda_j) + \frac{M_p I_p \lambda_j^4}{\rho^2 A^2 L^4} (1 - \cos \lambda_j \cosh \lambda_j) = 0 \quad (4.3)$$

Since the distributed-parameter system has infinite vibrational modes, the general response is the superposition of the responses from all of the vibrational modes:

$$w(x, t) = \sum_{j=1}^{\infty} \phi_j(x) u_j(t), \quad (4.4)$$

where

$$\phi_j(x) = \cos \left( \frac{\lambda_j}{L} x \right) - \cosh \left( \frac{\lambda_j}{L} x \right) + \frac{\sin \lambda_j - \sinh \lambda_j + \frac{\lambda_j M_p}{\rho A L} (\cos \lambda_j - \cosh \lambda_j)}{\cos \lambda_j + \cosh \lambda_j - \frac{\lambda_j M_p}{\rho A L} (\sin \lambda_j - \sinh \lambda_j)} \left( \sin \left( \frac{\lambda_j}{L} x \right) - \sinh \left( \frac{\lambda_j}{L} x \right) \right), \quad (4.5)$$

and

$$u_j(t) = (C_{1j} \cos(\omega_j t) + C_{2j} \sin(\omega_j t)) e^{-b \frac{\omega_j^2}{EI_{zz}} t}, \quad (4.6)$$

where  $C_{1j}$  and  $C_{2j}$  are constants depending on the mode.

In the simulation, despite only the first twenty eigenmodes included, the error is merely 1% more than that including the first two hundred eigenmodes. Therefore, we only adopt the first twenty eigenmodes in our simulation. Then, the initial shape of static beam is projected to the twenty mode shapes, as shown in Fig. 4-2. While the stick unloads, it carries the puck with it until it begins to decelerate, at which point

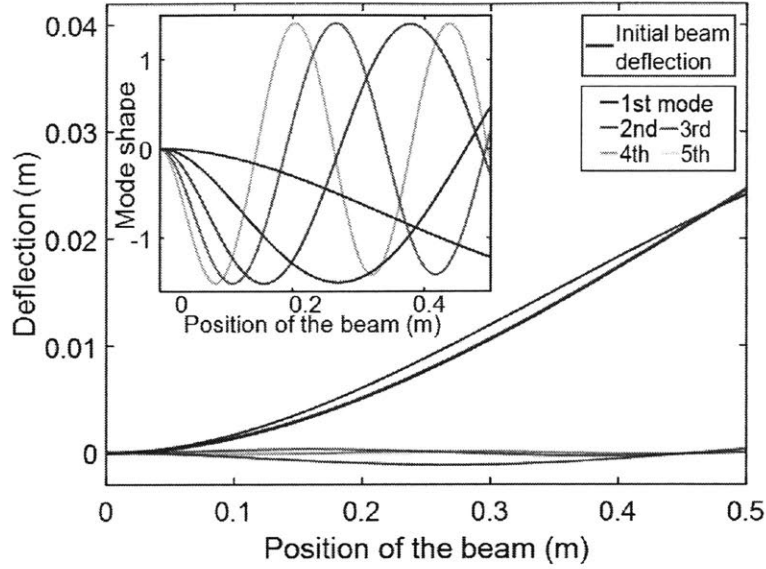


Figure 4-2: Modal decomposition of initial deflection of the beam under static load. The first five eigenmodes are included in the figure. (Inset) Mode shapes of the first five eigen modes.

the puck will continue moving at its exit velocity which is equal to the maximum velocity of the distal end of the stick. This process is shown in Fig. 4-1 (c). We obtain the velocity of the puck by calculating the maximum velocity of the stick's end over the first period of oscillation according to the first eigenmode.

$$v_p = \max \left( \frac{\partial w(x, t)}{\partial t} \Big|_{x=L, t \in T_1} \right), \quad (4.7)$$

where  $T_1$  is the first period of oscillation for the first eigenmode.

The magnitude of the puck velocity monotonically increases as the Young's modulus of the beam decreases, as shown in Fig. 4-3. Despite having lower flexural rigidity, the beam can deflect more under the same initial load, allowing more potential energy to be stored in the beam and eventually transmitted to the puck. As the force that the player can exert on the sled hockey stick increases from 20 N to 60 N, the magnitude of the puck speed also increases for the same reason. The model suggests the flexural rigidity should be as low as possible to produce the highest puck speed. However, there must be a lower bound on the flexural rigidity for two reasons. At first, the rigidity should be enough to allow player move the sled across the ice rink in

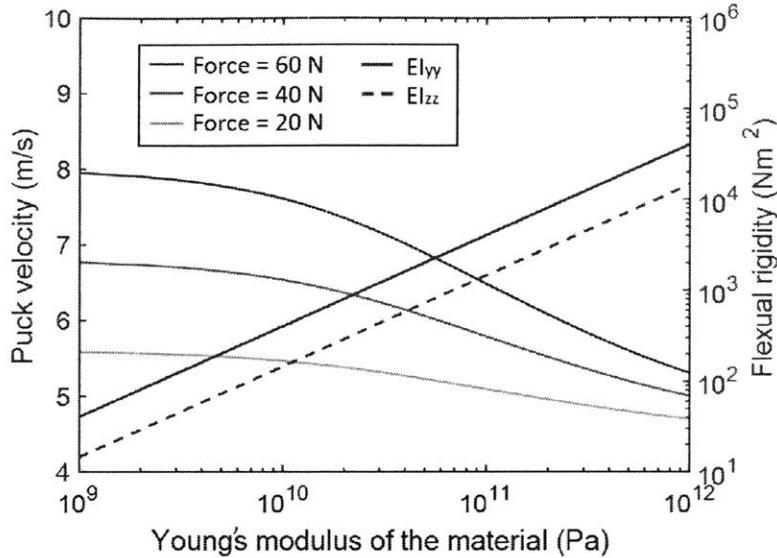


Figure 4-3: The magnitude of the puck velocity and the flexural rigidity as a function of Young's modulus of the material of the beam respectively.

the driving mode. Secondly, the Euler-Bernoulli beam model breaks down for large deformations, as would be observed in the infinitely flexible case.

In addition, we find that the flexural rigidity with respect to  $Z$ -axis in shooting mode is about 0.2 times of that with respect to  $Y$ -axis in driving mode. This opens up the design space to explore the Young's modulus of the material. In particular, we can maximize the puck speed by decreasing the flexural rigidity with respect to  $Y$ -axis in driving mode, and at the same time, satisfy the constraint limited by the minimum flexural rigidity in shooting mode at  $Z$ -axis.

### 4.3 Experiments, Results and Discussion

We built a prototype for a more flexible sled hockey stick made of acrylonitrile butadiene styrene (ABS). The design of the stick and the Young's modulus of the material are determined and selected according to the simulation results discussed above. As shown in Fig. 4-4, our prototype of the more flexible stick is stacked by five laminated layers. Each layer was manufactured by waterjet machine and bonded together using adhesives (Loctite 4851) which can accommodate joint movement. Since players only use the shaft of the sled hockey sticks to drive the sled on ice, we tapered the blade



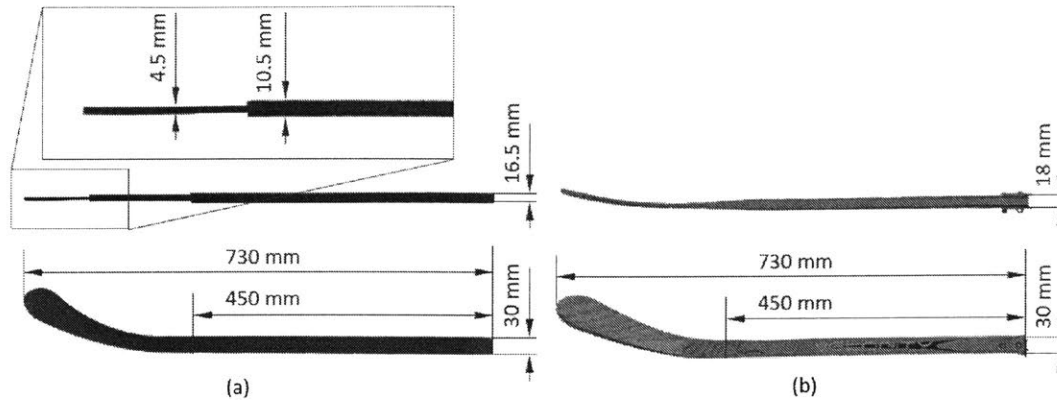


Figure 4-4: (a) Prototype of a more flexible sled hockey stick; (b) A commercially-available sled hockey stick.

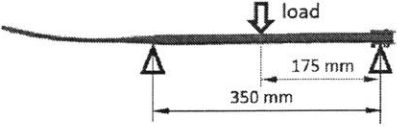
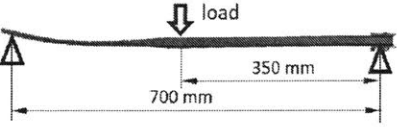
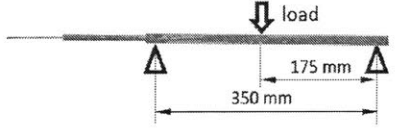
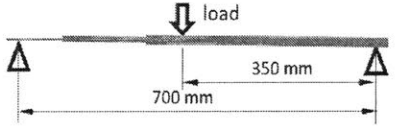
part of the sticks to further reduce its flexural rigidity considered in the shooting mode.

In order to characterize the stiffness of the two types of sled hockey sticks, we conducted the three-point bend test. Considering that the shaft stiffness is much larger than that of the blade, we performed two types of loading, as shown in Table 4.1, to measure the stiffness of the shaft and stiffness of the entire sled hockey stick. Testing was performed using an Instron Universal Testing Instrument (Model 1125). Each stick was loosely strapped at the middle and upper end of the shaft to two cylindrical supports. The maximum force was set to be 50 N, which was selected to simulate the load encountered on the stick during use. The load was applied by the platform using a cylindrical head. Stiffness was calculated as the slope of the linear regression of the force deformation curve during the entire loading cycle.

Eighteen subjects who provided the informed written consent were recruited to perform wrist shots with different sticks. Five subjects are female and thirteen subjects are male. Fourteen of the subjects ( $\text{age} = 26.3 \pm 2.3$ ) are recreational players with minor experience on sled hockey; the other four subjects are elite players from WSF New York Sled Rangers with more experience.

Experiments for recreational sled hockey players were conducted in a laboratory setting where the subjects performed a wrist shot and shot the puck off of a high

Table 4.1: Stiffness of the flexible and rigid sled hockey sticks

Material	Loading	Stiffness (kN/m)
Wood		$(1.85 \pm 0.09) \times 10^2$
Wood		$(1.79 \pm 0.09) \times 10$
ABS		$(1.61 \pm 0.08) \times 10$
ABS		$(1.2 \pm 0.1)$

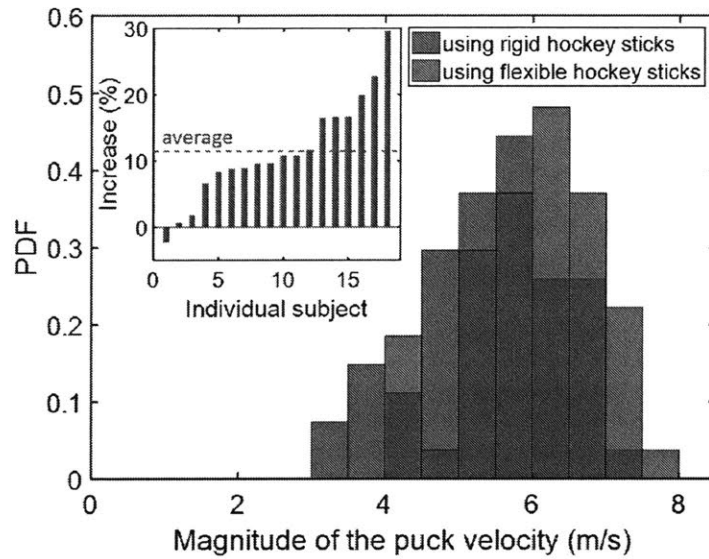


Figure 4-5: Histograms for the magnitude of the velocity of the puck using two types of sled hockey sticks. The histogram is normalized by the discrete probability density function (PDF). (Inset) The increase in percentage of the magnitude of the puck velocity in ascendant order for each individual subject using flexible sled hockey sticks compared to that using rigid sticks. The dashed line indicates the average increase which is 11.48%.

density polymer ethylene ‘synthetic ice’ shooting pad. Experiments for elite sled hockey players were conducted in an ice rink with “synthetic ice”. In both settings, subjects are required to sit on the hockey sled in order to simulate the environment in a real sled hockey game. Each subject performed three wrist shots with the two types of sled hockey sticks - rigid hockey sticks and flexible hockey sticks.

Each subject was assigned sufficient time ( $9.4 \text{ min} \pm 1.2 \text{ min}$ ) to get used to the experimental setting and the two types of sled hockey sticks. Especially for the flexible stick, players need more time to practice and to take the full advantage of its flexibility. The shooting pace was self-monitored by the subjects to minimize any fatigue effects by inserting seated rest periods and water breaks whenever necessary. We ensured a minimum of 30 s’ gap between different trials on the same stick in order to eliminate any residual stress from previous trails. A shot was considered a valid trial based on two criteria: 1) the subject was satisfied that the trial was a maximal effort; 2) the sled hockey stick remains on the ice and in contact with the puck during the wrist shot. We used a camera (Canon EOS Rebel T6 Digital SLR) to videotape the wrist shots. We used ImageJ to enhance the contrast and Matlab software to extract the data of the motion of the puck and calculate the velocity of the puck.

In Fig. 4-5, we compared the magnitudes of the puck velocity for two types of sled hockey sticks using histogram. It suggests a significant improvement for players using flexible hockey sticks in terms of the puck speed. The average increase for all subject is 11.48 %. For a very small amount of subjects, the increase in puck speed is trivial and there is even one outlier with negative increase. We think it was caused by the fact that the flexible sled hockey sticks require more adjustment in the shooting strategy from players’ habit. Therefore, some subjects are not able to take the advantage of its flexibility due to unsuccessful adjustment.

In addition, we investigated the relationship between the peak force that players can exert and the magnitude of the puck velocity for rigid hockey sticks and flexible hockey sticks respectively. We first need to evaluate the force that players can exert with sled hockey sticks approximately. Subjects were required to hold the sled hockey sticks at the same position as that when they perform a wrist shot. They repeated the

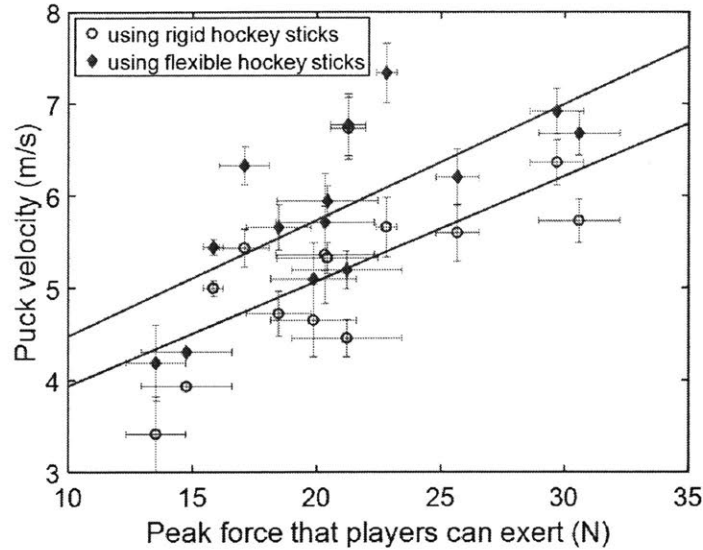


Figure 4-6: The magnitude of the puck velocity versus the peak force that players can exert with two lines indicating the linear regressions using the two types of sled hockey sticks respectively.

action five times for each type of sled hockey sticks, which gives us five measurements. In Fig. 4-6, the magnitude of the puck velocity is plotted versus the peak force that players can exert. The puck velocity shown in the figure represent the mean puck velocity from three tests and the mean peak force from five measurements respectively. The correlation coefficients between the magnitude of the puck velocity and the peak force that players can exert are 0.643 and 0.685 for rigid sled hockey sticks and flexible sled hockey sticks respectively. We also applied a linear regression method to fit the experimental data. The results clearly indicate that the flexible hockey sticks can generate larger puck velocities. Fig. 4-6 also graphically suggests a moderate positive linear association between peak force that players can exert and puck velocity for both types of sled hockey sticks.

## 4.4 Conclusion and Future Work

Cantilevered Euler-Bernoulli beam model with a cylindrical rigid body attached to its distal end captures the fundamental dynamic response of a wrist shot with flexible sled hockey sticks. We observe a significant increase on the magnitude of the puck

velocity by using our flexible prototype of sled hockey stick. The optimal flexural rigidity can be determined by maximizing the magnitude of the puck velocity in shooting mode with the constraint of minimum rigidity required in driving mode. We also discovered a moderate positive linear relationship between the peak force that players can exert and the magnitude of the puck velocity.

For the future work, we would further optimize the overall curvature of the sled hockey stick and the varied cross-sectional dimension of the sled hockey stick. In particular, the curvature within the blade of the stick and the smooth change of rigidity along the prototype should be considered which has not been introduced in our current fast prototype. In addition, a varied flexural rigidity may be worthwhile to be explored which can open a wider designing space to optimize the performance in both the shooting mode and the driving mode.

# Chapter 5

## Dynamics of Rigid Systems

Rigid system dynamics studies the dynamical behavior of a system, the elements of which, under the assumption, are treated as rigid bodies. In this Chapter, we propose two sets of dynamical modelling methods and apply the methodology on sled hockey equipment, further advancing the optimization and customization of the structures of the system.

Sled hockey, acting as the counterpart of standing ice hockey in Paralympic games, provides people with physical disabilities with the opportunity of participating in the game of ice hockey. Sled hockey players seating in hockey buckets propel the hockey sleds using one pair of hockey sticks. The investigation for the dynamics of the sled hockey advances the structural design for designers and strategic plan for players, aiming at the ultimate goal of optimizing the performance of sled hockey players.

In this chapter, we propose two sets of dynamical modelling for the hockey sled using a trajectory-based modelling method and a state-space-based modelling method. Conservation laws of linear momentum and angular momentum are applied to obtain the governing equations, which are used to study the dynamics of the propulsion for linear motion and of the tip-over and reset. We further propose a constrained optimization problem to optimize the parameters of sled design and driving strategy to maximize the performance of sled hockey players based on the dynamics.

## 5.1 Dynamical Modelling of Hockey Sled

We propose two sets of dynamical modelling for the hockey sled. The first set of model is obtained by considering the trajectory of the contact point between the hockey sled and the ice surface through three frames - an inertial frame, a local frame and an intermediate frame. The inertial frame is fixed on the ice ground, i.e., the reference frame of the observer at rest. The local frame is fixed on the hockey sled with the coordinates along with principal axis of the sled. The intermediate frame is build upon a virtual trajectory for the center of curvature of the local frame. The second set of model is obtained by considering the dynamics of the motion of vehicle with multiple constraints, which can be generalized for flights and other vehicles. The first model benefits in the interpretation of the coordinates for physical insights; the second model benefits in the generalization for other vehicles such as autos and flights.

### 5.1.1 Method 1: Trajectory-Based Modelling

The dynamics of hockey sled is significantly distinguished from that of autos and flights. The primary difference lies at the constraints of hockey sled, which, on one hand, allows for tip-over, compared with autos and, on the other hand, restrains one of the skate blades and foot support contacting the ice surface, compared with flights.

In the first dynamical model, we decompose the motions using three frames: an inertial frame fixed on the ice ground, an intermediate frame fixed on a virtual trajectory and a local frame fixed at the center of mass on the sled. Fig. 5-1 shows the schematic of the frames and the trajectories in our study of the hockey sled motion. Curve  $S_A$  is the trajectory of point A, which is the contact point between the skate blade and the ice surface. Curve  $S_{COC}$  is the trajectory of the center of curvature of curve  $S_A$ . Frame  $X_I Y_I Z_I$  is the inertial frame. Frame  $xyz$  is fixed on the sled along with the coordinates along with the principal axis of the sled, of which the coordinates  $y$  and  $z$  locate in plane  $P_2$  and coordinate  $x$  in  $P_1$ .  $P_1$  and  $P_2$  are virtual planes which are along the tangential and normal direction of the curve  $S_A$  respectively.

Frame  $XYZ$  is an intermediate frame with coordinate  $Y$  directing towards point A and coordinate  $Z$  consistent with  $Z_I$  in the inertial frame  $X_I Y_I Z_I$ .  $R(t)$  denotes the radius of the instantaneous curvature of curve  $S_A$ .  $\mathbf{r}_{AC}$  is the vector from point A to the center of mass as denoted in Fig. 5-2 and Fig. 5-3.

$$\mathbf{r}_{AC} = b_x \hat{\mathbf{e}}_x + b_y \hat{\mathbf{e}}_y + b_z \hat{\mathbf{e}}_z, \quad (5.1)$$

where  $b_x$ ,  $b_y$ ,  $b_z$  are distances from point A to the center of mass along the three principal axes of the hockey sled. Fig. 5-2 indicates  $b_x < 0$  to be consistent with the definition of the local frame  $xyz$ .

The intermediate frame  $XYZ$  is utilized to bridge the inertial frame  $X_I Y_I Z_I$  and the local frame  $xyz$ . The motion of the hockey sled is decomposed into the motion described by the lean angle  $\theta(t)$  and the planer motion of point A using the local frame  $xyz$ . The motion of point A is further decomposed into the planner motion of the origin of frame  $XYZ$  and the radius  $R(t)$  of the instantaneous curvature of curve  $S_A$  using the intermediate frame  $XYZ$ . The relationship between the local frame  $xyz$  and the intermediate frame  $XYZ$  can be expressed as:

$$\begin{aligned} \mathbf{e}_X &= \mathbf{e}_x, \\ \mathbf{e}_Y &= \mathbf{e}_y \cos \theta + \mathbf{e}_z (-\sin \theta), \\ \mathbf{e}_Z &= \mathbf{e}_y \sin \theta + \mathbf{e}_z \cos \theta, \end{aligned} \quad (5.2)$$

where  $\mathbf{e}_x$ ,  $\mathbf{e}_y$  and  $\mathbf{e}_z$  represent the unit vectors along with  $x$ -,  $y$ - and  $z$ -directions of the local frame  $xyz$  respectively,  $\mathbf{e}_X$ ,  $\mathbf{e}_Y$  and  $\mathbf{e}_Z$  represent the unit vectors along with  $X$ -,  $Y$ - and  $Z$ -directions of the local frame  $XYZ$  respectively. The relationship between the inertial frame  $X_I Y_I Z_I$  and the intermediate frame  $XYZ$  can be expressed as:

$$\begin{aligned} \mathbf{e}_{X_I} &= \mathbf{e}_X \cos \phi + \mathbf{e}_Y (-\sin \phi), \\ \mathbf{e}_{Y_I} &= \mathbf{e}_X \sin \phi + \mathbf{e}_Y \cos \phi, \\ \mathbf{e}_{Z_I} &= \mathbf{e}_Z, \end{aligned} \quad (5.3)$$



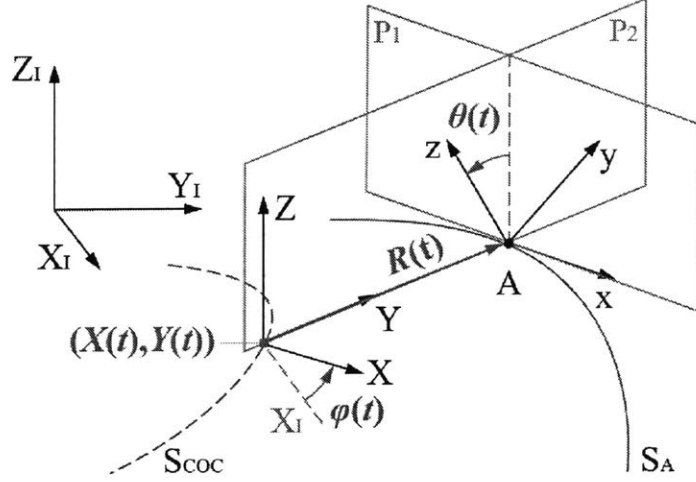


Figure 5-1: Schematic of the frames and the trajectories for the motion of hockey sled. Point A is the contact point between the skate blade and ice surface.  $S_A$  is the trajectory of A.  $S_{COC}$  is the trajectory of the center of curvature of  $S_A$ .  $X_I Y_I Z_I$  is the inertial frame. Frame  $xyz$  is fixed on the sled along the principal axis of the sled, of which the coordinates  $y$  and  $z$  locate in plane  $P_2$  and coordinate  $x$  in  $P_1$ . Frame  $XYZ$  is an intermediate frame, of which the coordinate  $y$  directs towards point A.  $P_1$  and  $P_2$  are virtual planes which are parallel and perpendicular to the curve  $S_A$  respectively.

where  $e_{X_I}$ ,  $e_{Y_I}$  and  $e_{Z_I}$  represent the unit vectors along with  $X_I$ -,  $Y_I$ - and  $Z_I$ -directions of the local frame  $X_I Y_I Z_I$  respectively.

The angular velocity of the sled can be decomposed into the angular speeds in  $e_x$  and  $e_z$ . Thus,  $\omega_{sled}$  is given by:

$$\omega_{sled} = \hat{e}_x \dot{\theta} + \hat{e}_z \dot{\phi} = \hat{e}_x \dot{\theta} + \hat{e}_y \dot{\phi} \sin \theta + \hat{e}_z \dot{\phi} \cos \theta. \quad (5.4)$$

The unit vectors  $\hat{e}_x$ ,  $\hat{e}_y$  and  $\hat{e}_z$  are fixed on a rotating frame  $xyz$  with the angular velocity  $\omega_{sled}$ . The partial derivatives of each unit vector with respect to time are:

$$\begin{aligned} \frac{\partial \hat{e}_x}{\partial t} &= \omega_{sled} \times \hat{e}_x = \hat{e}_y \dot{\phi} \cos \theta + \hat{e}_z (-\dot{\phi} \sin \theta), \\ \frac{\partial \hat{e}_y}{\partial t} &= \omega_{sled} \times \hat{e}_y = \hat{e}_x (-\dot{\phi} \cos \theta) + \hat{e}_z \dot{\theta}, \\ \frac{\partial \hat{e}_z}{\partial t} &= \omega_{sled} \times \hat{e}_z = \hat{e}_x \dot{\phi} \sin \theta + \hat{e}_y (-\dot{\theta}), \end{aligned} \quad (5.5)$$

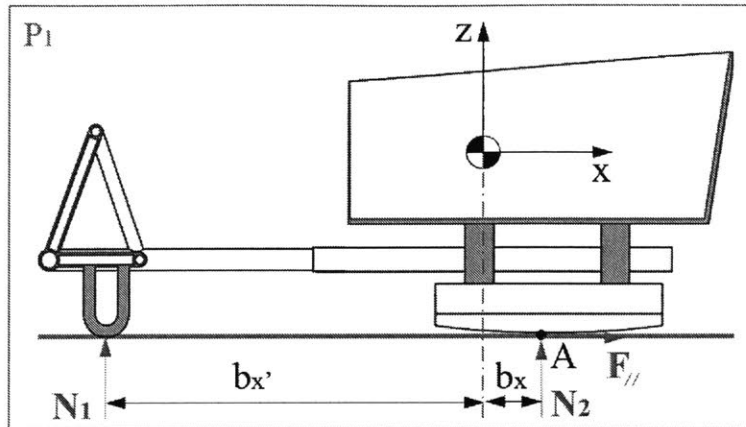


Figure 5-2: Schematic of the back view of hockey sled and free body diagram.  $N_1$  is the normal reaction force for the foot support of the hockey sled. Point A is the contact point between one hockey blade and the ice surface.  $N_2$  is the normal reaction force for skate blades at point A.  $b_{x'}$  and  $b_x$  are distances between the center of mass and the foot support of the sled and point A respectively.  $F_{\parallel}$  is the frictional force acted on the skate blade.  $P_2$  is the virtual plane as shown in Fig. 5-1, which is parallel to the trajectory of A.

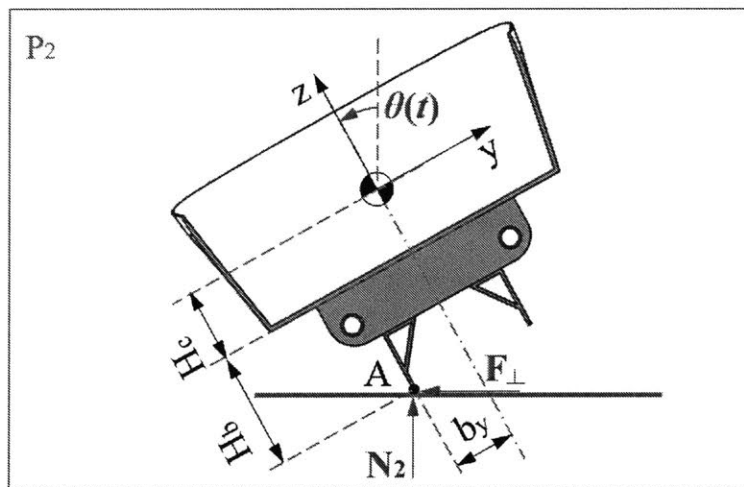


Figure 5-3: Schematic of the back view of hockey sled and free body diagram. Point A is the contact point between one hockey skate blade and the ice surface.  $\theta(t)$  is the lean angle of the sled,  $N_2$  is the normal reaction force for the foot support and skate blade respectively.  $F_{\perp}$  is the frictional reaction force between ice and the skate blade at point A.  $H_c$ ,  $H_b$  and  $b_y$  are dimensions of the hockey sled with respect to the center of mass.

The velocity of the origin of intermediate frame  $XYZ$  on curve  $S_{COC}$  is:

$$\begin{aligned}
\mathbf{v}_{COC} &= \hat{\mathbf{e}}_{X_I} \dot{X}(t) + \hat{\mathbf{e}}_{Y_I} \dot{Y}(t) \\
&= \hat{\mathbf{e}}_X [\dot{X} \cos \phi + \dot{Y} \sin \phi] + \hat{\mathbf{e}}_Y [-\dot{X} \sin \phi + \dot{Y} \cos \phi] \\
&= \hat{\mathbf{e}}_x [\dot{X} \cos \phi + \dot{Y} \sin \phi] + \hat{\mathbf{e}}_y [-\dot{X} \sin \phi \cos \theta + \dot{Y} \cos \phi \cos \theta] \\
&\quad + \hat{\mathbf{e}}_z [\dot{X} \sin \phi \sin \theta - \dot{Y} \cos \phi \sin \theta]
\end{aligned} \tag{5.6}$$

The hockey sled is symmetric with respect to the plane  $P_1$ . Thus, the second moment of inertia  $\mathbf{I}_{xy} = \mathbf{I}_{yx} = 0$ ,  $\mathbf{I}_{yz} = \mathbf{I}_{zy} = 0$ . Empirically, we take  $\mathbf{I}_{yz} = \mathbf{I}_{zy} \approx 0$  for simplicity. The angular momentum of the sled with respect to the center of mass  $\mathbf{H}_c$  is given by:

$$\begin{aligned}
\mathbf{H}_c &= \hat{\mathbf{e}}_x [\mathbf{I}_{xx} \dot{\theta} + \mathbf{I}_{xz} \dot{\phi} \cos \theta] + \hat{\mathbf{e}}_y \mathbf{I}_{yy} \dot{\phi} \sin \theta + \hat{\mathbf{e}}_z [\mathbf{I}_{zz} \dot{\phi} \cos \theta + \mathbf{I}_{xz} \dot{\theta}] \\
&\approx \hat{\mathbf{e}}_x \mathbf{I}_{xx} \dot{\theta} + \hat{\mathbf{e}}_y \mathbf{I}_{yy} \dot{\phi} \sin \theta + \hat{\mathbf{e}}_z \mathbf{I}_{zz} \dot{\phi} \cos \theta.
\end{aligned} \tag{5.7}$$

Using the approximated expression of  $\mathbf{H}_c$ , its first derivative with respect to time:

$$\begin{aligned}
\frac{d\mathbf{H}_c}{dt} &= \hat{\mathbf{e}}_x [\mathbf{I}_{xx} \ddot{\theta} + (\mathbf{I}_{zz} - \mathbf{I}_{yy}) \dot{\phi}^2 \sin \theta \cos \theta] \\
&\quad + \hat{\mathbf{e}}_y [(\mathbf{I}_{xx} + \mathbf{I}_{yy} - \mathbf{I}_{zz}) \dot{\phi} \dot{\theta} \cos \theta + \mathbf{I}_{yy} \ddot{\phi} \sin \theta] \\
&\quad + \hat{\mathbf{e}}_z [\mathbf{I}_{zz} (\ddot{\phi} \cos \theta - \dot{\phi} \dot{\theta} \sin \theta) + (\mathbf{I}_{yy} - \mathbf{I}_{xx}) \dot{\theta} \dot{\phi} \sin \theta].
\end{aligned} \tag{5.8}$$

The velocity of the center of mass is  $\mathbf{v}_c$ , given by:

$$\begin{aligned}
\mathbf{v}_c &= \mathbf{v}_A + \boldsymbol{\omega}_{sled} \times \mathbf{r}_{AC} \\
&= \mathbf{v}_{ICR} + \boldsymbol{\omega}_{XYZ} \times \mathbf{r}_{OA} + (\hat{\mathbf{e}}_x \dot{\theta} + \hat{\mathbf{e}}_y \dot{\phi} \sin \theta + \hat{\mathbf{e}}_z \dot{\phi} \cos \theta) \times (b_x \hat{\mathbf{e}}_x + b_y \hat{\mathbf{e}}_y + b_z \hat{\mathbf{e}}_z) \\
&= \hat{\mathbf{e}}_x [\dot{X} \cos \phi + \dot{Y} \sin \phi + (-1)R\dot{\phi} + b_z \dot{\phi} \sin \theta - b_y \dot{\phi} \cos \theta] \\
&\quad + \hat{\mathbf{e}}_y [-\dot{X} \sin \phi \cos \theta + \dot{Y} \cos \phi \cos \theta + b_x \dot{\phi} \cos \theta - b_z \dot{\theta}] \\
&\quad + \hat{\mathbf{e}}_z (-\sin \theta) [-\dot{X} \sin \phi + \dot{Y} \cos \phi] + (-b_x) \dot{\phi} \sin \theta + b_y \dot{\theta}.
\end{aligned} \tag{5.9}$$

Thus,

$$\begin{aligned} \frac{d\mathbf{v}_c}{dt} \cdot \hat{\mathbf{e}}_x &= \ddot{X} \cos \phi + \ddot{Y} \sin \phi + \ddot{\phi}[-R + b_z \sin \theta - b_y \cos \theta] + \dot{\phi}^2(-b_x) \\ &+ 2\dot{\theta}\dot{\phi}(b_z \cos \theta + b_y \sin \theta), \end{aligned} \quad (5.10)$$

$$\begin{aligned} \frac{d\mathbf{v}_c}{dt} \cdot \hat{\mathbf{e}}_y &= \ddot{X}(-\sin \phi \cos \phi) + \ddot{Y} \cos \theta \cos \phi + \ddot{\theta}(-b_z) + \dot{\theta}^2(-b_y) \\ &+ \dot{\phi}^2(-R \cos \theta + b_z \sin \theta \cos \theta - b_y \cos^2 \theta), \end{aligned} \quad (5.11)$$

$$\begin{aligned} \frac{d\mathbf{v}_c}{dt} \cdot \hat{\mathbf{e}}_z &= \ddot{X}(\sin \theta \sin \phi) + \ddot{Y}(-\sin \theta \cos \phi) + \ddot{\theta}(b_y) + \dot{\theta}^2(-b_z) \\ &+ \dot{\phi}^2(-b_z \sin^2 \theta + b_y \sin \theta \cos \theta + R \sin \theta). \end{aligned} \quad (5.12)$$

Applying the conservation law of linear momentum, we obtain the equation of motion.

In  $\hat{\mathbf{e}}_x$ :

$$\begin{aligned} \ddot{\phi}(mb_z \sin \theta - mb_y \cos \theta - mR) + \ddot{X}(m \cos \phi) + \ddot{Y}(m \sin \phi) + \dot{\phi}\dot{R}(-m) \\ + \dot{\theta}\dot{\phi}(2mb_z \cos \theta + 2mb_y \sin \theta) + \dot{\phi}^2(-mb_x) = f_{\parallel} + f_x; \end{aligned} \quad (5.13)$$

in  $\hat{\mathbf{e}}_y$ :

$$\begin{aligned} \ddot{\theta}(-mb_z) + \ddot{\phi}(mb_x \cos \theta) + \ddot{X}(-m \cos \theta \sin \phi) + \ddot{Y}(m \cos \theta \cos \phi) + \dot{\theta}^2(-mb_y) \\ + \dot{\phi}^2(mb_z \sin \theta \cos \theta - mb_y \cos^2 \theta - mR \cos \theta) \\ = (N_1 + N_2) \sin \theta - mg \sin \theta - f_{\perp} \cos \theta + f_y; \end{aligned} \quad (5.14)$$

and in  $\hat{\mathbf{e}}_z$ :

$$\begin{aligned} \ddot{\theta}(mb_y) + \ddot{\phi}(-mb_x \sin \theta) + \ddot{X}(m \sin \theta \sin \phi) + \ddot{Y}(-m \sin \theta \cos \theta) + \dot{\theta}^2(-mb_z) \\ + \dot{\phi}^2(-mb_z \sin^2 \theta + mb_y \sin \theta \cos \theta + mR \sin \theta) \\ = (N_1 + N_2) \cos \theta - mg \cos \theta + f_{\perp} \cos \theta + f_z, \end{aligned} \quad (5.15)$$

where  $f_{\perp}$  and  $f_{\parallel}$  are the frictional forces, the directions of which are perpendicular and parallel to the direction of the skate blades,  $f_x$ ,  $f_y$  and  $f_z$  are external forces exerted on the sled in  $x$ -,  $y$ - and  $z$ -directions. We apply the conservation of angular

momentum with respect to point A. Since point A has a moving velocity of  $\mathbf{v}_A$ , the conservation law can be expressed as:

$$\boldsymbol{\tau}_A = \frac{d\mathbf{H}_c}{dt} + \mathbf{r}_{AC} \times \frac{d\mathbf{P}}{dt}, \quad (5.16)$$

where  $\boldsymbol{\tau}_A$  is the external torque exerted on the hockey sled with respect to point A,  $\mathbf{H}_c$  is the angular momentum of the sled,  $\mathbf{r}_{AC}$  is the vector from the contact point A to the center of mass C and  $\mathbf{P}$  is the linear momentum of the rigid body, we obtain the equations of motion. In  $\hat{\mathbf{e}}_x$ :

$$\begin{aligned} & \ddot{\theta}[I_{xx} + m(b_y^2 + b_z^2)] + \ddot{\phi}[-mb_x b_y \sin \theta - mb_x b_z \cos \theta] + \ddot{X}[mb_y \sin \theta \sin \phi + mb_z \cos \theta \sin \phi] \\ & + \dot{\phi}^2[mb_y b_z \cos(2\theta) + m(b_y^2 - b_z^2) \sin \theta \cos \theta + mRb_z \cos \theta + (I_{zz} - I_{yy}) \sin \theta \cos \theta + mRb_y \sin \theta] \\ & + \ddot{Y}[-mb_y \sin \theta \cos \phi - mb_z \cos \theta \cos \phi] = mg(b_z \sin \theta - b_y \cos \theta) + \tau_x, \end{aligned} \quad (5.17)$$

in  $\hat{\mathbf{e}}_y$ :

$$\begin{aligned} & \ddot{\theta}[-mb_x b_y] + \ddot{\phi}[-mb_z R + m(b_x^2 + b_z^2) \sin \theta - mb_y b_z \cos \theta + I_{yy} \sin \theta] \\ & + \ddot{X}[mb_z \cos \phi - mb_x \sin \theta \sin \phi] + \ddot{Y}[mb_x \sin \theta \cos \phi + mb_z \sin \phi] + \dot{\theta}^2[mb_x b_z] \\ & + \dot{\phi}^2[mb_x b_z (\sin^2 \theta - 1) - mb_x b_y \sin(\theta) \cos(\theta) + mRb_x \sin \theta] + \dot{\phi} \dot{R}(-mb_z) \\ & + \dot{\phi} \dot{\theta}[(I_{xx} + I_{yy} - I_{zz}) \cos \theta + 2mb_z^2 \cos \theta + 2mb_y b_z \sin \theta] \\ & = (N_1 b_{x'} + N_2 b_x) \cos \theta + \tau_y, \end{aligned} \quad (5.18)$$

and in  $\hat{\mathbf{e}}_z$ :

$$\begin{aligned} & \ddot{\theta}[-mb_x b_z] + \ddot{\phi}[mb_y R + m(b_x^2 + b_y^2) \cos \theta - mb_y b_z \sin \theta + I_{zz} \cos \theta] \\ & + \ddot{X}[-mb_x \cos \theta \sin \phi - mb_y \cos \phi] + \ddot{Y}[mb_x \cos \theta \cos \phi - mb_y \sin \phi] \\ & + \dot{\theta}^2[-mb_x b_y] + \dot{\phi}^2[-mb_x R \cos \theta + mb_x b_z \sin \theta \cos \theta - mb_x b_y (\cos^2 \theta + 1)] \\ & + \dot{\phi} \dot{\theta}[-2mb_y b_z \cos \theta - 2mb_y^2 \sin \theta + (I_{yy} - I_{xx} - I_{zz}) \sin \theta] \\ & = -(N_1 b_{x'} + N_2 b_x) \sin \theta + \tau_z, \end{aligned} \quad (5.19)$$

where  $\tau_x$ ,  $\tau_y$  and  $\tau_z$  are the components of  $\boldsymbol{\tau}_A$  in  $x$ -,  $y$ -, and  $z$ -directions.

### 5.1.2 Method 2: State-Space-Based Modelling

In this section, we develop a state-space-based dynamic model for the hockey sled, as a counterpart for autos and flights, in the field of ice hockey. We borrow the terminology *state space*, typically utilized in control and estimation theory [90, 91, 92]. The *state space* is the Euclidean space, in which the variables of the axis represent the state variables. The values of state variables evolve through time, depending on the initial conditions and the external inputs [93, 94]. Correspondingly, a state-space representation describes the dynamics of a physical system, usually in the form of a system of differential equations [90, 95]. This method supplements the trajectory-based dynamical modelling method, to which the research findings can be easily transferred from the field of autos and flights [96, 97].

We incorporate two reference frames - a local frame and an inertial frame to obtain the governing equations of the dynamics. In the local frame fixed on the sled, the variables  $x$ ,  $y$  and  $z$  represent local coordinates. The origin of the frame  $xyz$  locates at the center of mass of the sled, the directions of which are aligned with the directions of the principal axis of hockey sled. The  $x$ -axis lies in the symmetry plane of the sled and points toward the forward-direction of the sled. The  $z$ -axis also lies in the plane of symmetry, perpendicular to the  $x$ -axis, and pointing down to the ground. The  $y$ -axis completes a right-handed orthogonal system.  $F_x$ ,  $F_y$  and  $F_z$  are equivalent net forces exerted on the sled in  $x$ ,  $y$  and  $z$  directions, respectively;  $T_x$ ,  $T_y$  and  $T_z$  are equivalent net torques exerted on the sled with respect to the center of the mass of the sled in  $x$ ,  $y$  and  $z$  directions, respectively. The Euler angles  $\psi$ ,  $\theta$  and  $\phi$  are correspondingly defined as the *yaw* angle, *pitch* angle and *roll* angle, rotated about  $z$ -axis,  $y$ -axis and  $x$ -axis, respectively.

To obtain the equations of motion of the hockey sled, the final orientation of the sled can be achieved by a virtual procedure of rotating through the heading angle  $\psi$ , the pitching angle  $\theta$  and the rolling angle  $\phi$  in sequence. Since there are commonly at least two contact points between the hockey sled and the ice ground, the motion of

the pitch angle  $\theta$  is constrained. We consider  $\theta \equiv 0$  for a regular motion of the hockey sled; thus, the angular velocity  $\dot{\theta} \equiv 0$  and the acceleration  $\ddot{\theta} \equiv 0$ . The transformation of the state space variables around the heading angle  $\psi$ , the pitching angle  $\theta$  and the rolling angle  $\phi$  can be expressed in the matrix form as  $\mathbb{R}(\psi)$ ,  $\mathbb{R}(\theta)$  and  $\mathbb{R}(\phi)$ . The rotation matrix  $\mathbb{R}$  from the inertial frame to the body frame through  $\phi$  is given by:

$$\mathbb{R}(\phi) = \begin{bmatrix} 1 & 0 & 0 \\ 0 & \cos \phi & -\sin \phi \\ 0 & \sin \phi & \cos \phi \end{bmatrix}, \quad (5.20)$$

through the rolling angle  $\theta$ :

$$\mathbb{R}(\theta) = \begin{bmatrix} \cos \theta & 0 & \sin \theta \\ 0 & 1 & 0 \\ -\sin \theta & 0 & \cos \theta \end{bmatrix}, \quad (5.21)$$

through the heading angle  $\psi$ :

$$\mathbb{R}(\psi) = \begin{bmatrix} \cos \psi & -\sin \psi & 0 \\ \sin \psi & \cos \psi & 0 \\ 0 & 0 & 1 \end{bmatrix}. \quad (5.22)$$

Thus, the rotation matrix achieved by the sequence of rotations aforementioned

can be expressed by a matrix transformation  $\mathbb{R}$ :

$$\begin{aligned}
\mathbb{R} &= (\mathbb{R}_\phi \mathbb{R}_\theta \mathbb{R}_\psi)^{-1} \\
&= \mathbb{R}_\psi^{-1} \mathbb{R}_\theta^{-1} \mathbb{R}_\phi^{-1} \\
&= \begin{bmatrix} \cos \theta \cos \psi & \sin \phi \sin \theta \cos \psi - \cos \phi \sin \psi & \cos \phi \sin \theta \cos \psi + \sin \phi \sin \psi \\ \cos \theta \sin \psi & \sin \phi \sin \theta \sin \psi + \cos \phi \cos \psi & \cos \phi \sin \theta \sin \psi - \sin \phi \cos \psi \\ -\sin \theta & \sin \phi \cos \theta & \cos \phi \cos \theta \end{bmatrix}, \\
&\stackrel{\theta=0}{=} \begin{bmatrix} \cos \psi & -\cos \phi \sin \psi & \sin \phi \sin \psi \\ \sin \psi & \cos \phi \cos \psi & -\sin \phi \cos \psi \\ 0 & \sin \phi & \cos \phi \end{bmatrix},
\end{aligned} \tag{5.23}$$

We can obtain the system of equations of motion by applying the conservation law of linear momentum:

$$\sum \mathbf{F} = \frac{d\mathbf{P}}{dt}, \tag{5.24}$$

where  $\mathbf{F}$  is the external force exerted on the hockey sled and  $\mathbf{P}$  is the linear momentum of the hockey sled.

The force vector  $\mathbf{F}$  includes the gravitational force and the reaction force from the ice ground on the hockey blades and the hockey sticks. The reaction force in the local frame is  $[F_x, F_y, F_z]^T = \mathbf{F}_{XYZ} \mathbb{R}$  and the gravitational force in the local frame is  $m\mathbf{g} \mathbb{R}$ . Applying the conservation law of linear momentum to the rigid body, we have:

$$\begin{bmatrix} F_x \\ F_y \\ F_z \end{bmatrix} + mg \begin{bmatrix} 0 \\ \sin \phi \\ \cos \phi \end{bmatrix} = \begin{bmatrix} \ddot{x} + (-\dot{\psi}\dot{y}) \\ \ddot{y} + (\dot{\psi}\dot{x} - \dot{\phi}\dot{z}) \\ \ddot{z} + (\dot{\phi}\dot{y}) \end{bmatrix}. \tag{5.25}$$

We further obtain the system of equations of motion applying the conservation law of angular momentum:

$$\sum \mathbf{T} = \frac{d\mathbf{H}_C}{dt}, \tag{5.26}$$

where  $\mathbf{T}$  is the external torque exerted on the hockey sled and  $\mathbf{H}$  is the angular



momentum of the hockey sled with respect to the center of mass  $C$ . Applying the conservation law of angular momentum to the rigid body, we have:

$$\begin{bmatrix} T_x \\ T_y \\ T_z \end{bmatrix} = \begin{bmatrix} \mathbf{I}_{xx}\ddot{\phi} + (-\mathbf{I}_{xz}\ddot{\psi}) \\ (\mathbf{I}_{xx} - \mathbf{I}_{zz})\dot{\psi}\dot{\phi} + \mathbf{I}_{xz}(\dot{\phi}^2 - \dot{\psi}^2) \\ \mathbf{I}_{zz}\ddot{\psi} - \mathbf{I}_{xz}\ddot{\phi} \end{bmatrix}, \quad (5.27)$$

where the second moment of inertia is given by:

$$\begin{aligned} \mathbf{I}_{xx} &= \int_m (y^2 + z^2) dm, \\ \mathbf{I}_{yy} &= \int_m (x^2 + z^2) dm, \\ \mathbf{I}_{zz} &= \int_m (x^2 + y^2) dm, \end{aligned} \quad (5.28)$$

and the product of inertia is given by:

$$\begin{aligned} \mathbf{I}_{xy} &= \mathbf{I}_{yx} = 0, \\ \mathbf{I}_{yz} &= \mathbf{I}_{zy} = 0, \\ \mathbf{I}_{xz} &= \mathbf{I}_{zx} \approx 0. \end{aligned} \quad (5.29)$$

The product of inertia  $\mathbf{I}_{xy}$  and  $\mathbf{I}_{yz}$  are zero due to the symmetry of the hockey sled, and  $\mathbf{I}_{xz}$  is approximately zero given our empirical assumption of the hockey sled with one sled hockey player.

The regular motion of the hockey sled requires that the contact point A on one of the two blades always keep contact with ice. Thus, the velocity at point A on the sled in  $\hat{e}_Z$  remains zero, i.e.  $\mathbf{v}_A \hat{e}_Z = 0$ . This equation acts as a constraint to the dynamics of the rigid body:

$$\mathbf{v}_A \hat{e}_Z = (\dot{y}_c + L_x \dot{\psi} - L_z \dot{\phi}) \sin \phi + (\dot{z}_c + L_y \dot{\phi} - L_x \dot{\theta}) \cos \phi = 0 \quad (5.30)$$

## 5.2 Propulsion for Linear Motion

### 5.2.1 Kinematics and Dynamics of Propulsion

Propulsion applied by sled hockey sticks is prevalent in the game of sled hockey, acting as the exclusive driving approach. Unlike the stand-up ice hockey, the driving mechanism in sled hockey is governed and constrained by the sled and sled hockey sticks. In competitive games, propulsion is of crucial importance for sled hockey players to navigate in the ice rink, to reach out for a puck, to maneuver a puck and to shoot a puck. In this section, we propose dynamical models to investigate the motion of sled driven by propulsion using sled hockey sticks. We further present an optimization problem to explore the strategy of propulsion and to probe the design space of structural parameters of the hockey sled and stick.

A sled hockey player drives the sled via the linkages of the upper arm, forearm, and hockey stick (see Fig. 5-4). The hockey stick end is anchored with a ratchet, used for exerting a force on the ice surface without any slip. The kinematics of the sled motion can be described by the angular velocity of the linkages, denoted by  $\dot{\theta}_1$ ,  $\dot{\theta}_2$  and  $\dot{\theta}_3$ ; the dynamics of the sled motion can be derived from the conservation of the linear momentum, where the input force is constrained by the muscle force that a player can produce on the hockey stick.

To generalize the study, we apply a dimensional analysis on the objective functions and constraints for the following three reasons: (a) Human body comes at a ratio for each age group; (b) For designers, the dimensionless form can be applied to generalize the structural design; (c) For players, the dimensionless form provides clearer guidance when they select the sled to optimize the performance of propulsion. To non-dimensionlize the equation of motion, we select the characteristic length  $L_0(= L_p)$  and the characteristic time  $1/\theta_M$ . Thus, we have dimensionless length scales and time scales:

$$\beta_1 = \frac{L_1}{L_0}, \beta_2 = \frac{L_2}{L_0}, \beta_3 = \frac{L_3}{L_0}, \beta_s = \frac{L_s}{L_0}, T = t\theta_M. \quad (5.31)$$

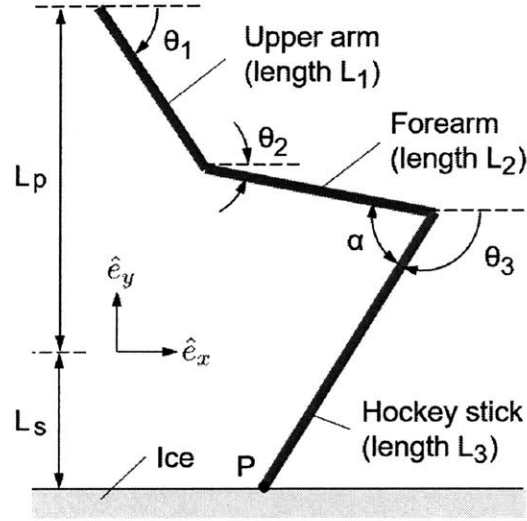


Figure 5-4: Schematic of the back view of hockey sled and free body diagram.  $L_1$  is the length of the player's upper arm,  $L_2$  is the length of the player's forearm,  $L_3$  is the effective length of the hockey stick, i.e. the distance from the position where a player holds the stick to the end of the stick,  $L_s$  is the distance from the ground to the bottom of the sled bucket, and  $L_p$  is the distance from the bottom of the bucket to the player's shoulder. Point P is the contact point between a hockey stick and the ice surface.

$\beta_1$  and  $\beta_2$  are constants determined by the body ratio of the sled hockey player, while  $\beta_s$  and  $\beta_3$  are variables based on the design of the hockey sled and hockey stick, respectively. The ratchet anchored at the end of sled hockey sticks imposes a non-slip condition at the contact point P between the stick end and the ice surface, as shown in Fig. 5-4. The non-slip condition can be described as  $\mathbf{v}_p \cdot \hat{e}_x = 0$  and  $\mathbf{v}_p \cdot \hat{e}_y = 0$ , providing us with the velocity  $\mathbf{v}$  of the sled and a motion constraint, respectively. The dimensionless velocity magnitude of the hockey sled is:

$$V = \frac{v}{L_0 \theta_M} = \sum_i \beta_i \dot{\Theta}_i \sin \Theta_i, \quad (i = 1, 2, 3). \quad (5.32)$$

The other two constraints are: (1)  $\Theta_2 - \Theta_3 + \pi = \alpha$ , where  $\alpha$  is the acute angle between the forearm and the hockey stick at the hockey player's wrist; (2) the equation of motion applying the linear momentum conservation in  $x$ -direction. Thus, the magnitude of the sled velocity  $V$  subjects to:

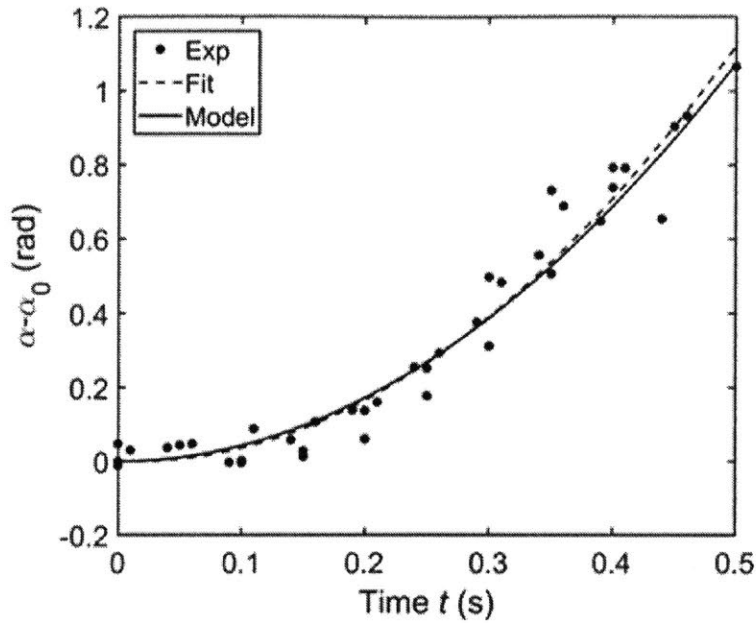


Figure 5-5: Experimental results for  $\alpha(t) - \alpha_0$  as a function of time  $t$ .  $\alpha_0$  is the initial angle at time  $t_0$  between the hockey stick and the forearm. A parabolic model, indicated in the dashed line, was fit for the experimental results compared with our hypothesis model.

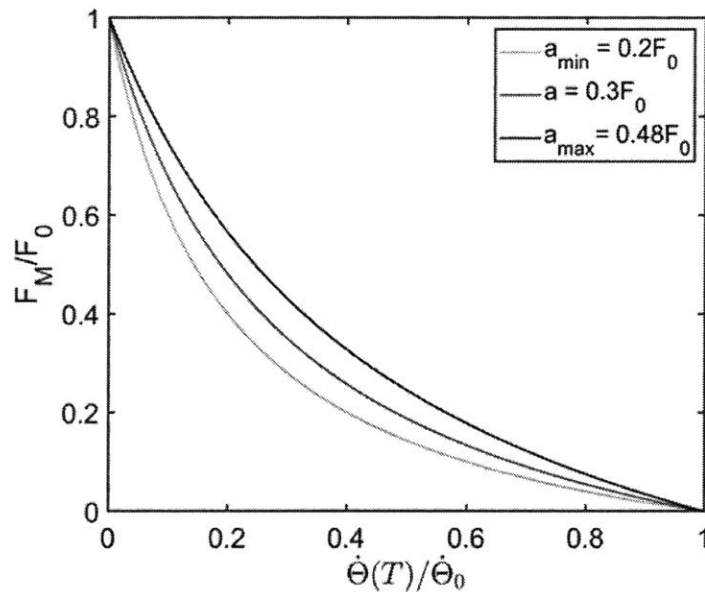


Figure 5-6: Simulation results for the ratio of  $F_M/F_0$  as a function of  $\dot{\Phi}(T)/\dot{\Phi}_0$ . The coefficient of shortening heat  $a_{min} = 0.2F_0$ ,  $a_{max} = 0.3F_0$  and  $a = 0.48F_0$  are illustrated in the figure.

$$\begin{aligned}
\ddot{\Theta}_2 - \ddot{\Theta}_3 &= \ddot{\alpha}, \\
\sum_i \beta_i \sin \Theta_i &= \beta_h + \beta_s, (i = 1, 2, 3), \\
\frac{2F}{(M+m)L_0\theta_M^2} \sin(\Theta_3 - \frac{\pi}{2}) &= -C_f^{\parallel} \frac{g}{L_0\theta_M^2} + \sum_i \beta_i \ddot{\Theta}_i \sin \Theta_i, (i = 1, 2, 3),
\end{aligned} \tag{5.33}$$

where  $M$  and  $m$  are the masses of the hockey sled and the hockey player respectively.  $C_f^{\parallel}$  is the frictional coefficient, the direction of which is parallel to the longitudinal direction of the skate blades. We select  $\ddot{\alpha}$ , which is a function of dimensionless time, to optimize the performance. In addition, we have the biological constraints:

$$\begin{aligned}
\Theta_2 &\leq \Theta_1, \\
\Theta_1 &\leq \pi/2, \\
\alpha &\leq \pi/2.
\end{aligned} \tag{5.34}$$

The force  $F$  exerted on the sled hockey stick is governed by the power from the hockey player. We apply the Hill's muscle model to approximate the force exerted on the hockey sticks,  $F \leq (bF_M - a\dot{\Theta}_2)/(b + \Theta_2)$ , in which  $F_M$  is the largest force that a player can perform,  $a$  is the coefficient of shortening heat and  $b = a\theta_M/F_0$  [98, 99]. The range of  $a$  is found to be from  $0.2F_0$  to  $0.48F_0$  [98]. Fig. 5-6 shows the ratio of  $F_M/F_0$  as a function of  $\dot{\Phi}(T)/\dot{\Phi}_0$  using different  $a$  values. The upper bound of error when using  $a = 0.3F_0$  is less than 5% compared with those using  $a = 0.2F_0$  and  $a = 0.48F_0$ . The Hill's muscle model can be reformulated in a dimensionless form:

$$\frac{F_M}{F_0} = \frac{a/F_0(1 - \dot{\Theta}/\dot{\Theta}_0)}{a/F_0 + \dot{\Theta}/\dot{\Theta}_0}, \tag{5.35}$$

$$F \leq F_M. \tag{5.36}$$

In this model, our assumption is that  $\alpha(t)$  takes a parabolic form, which characterizes the constraint between  $\Phi_2$  and  $\Phi_3$ . To verify our assumption, we conducted a simple experiment to record a hockey player's propulsion and extracted the motion of his arms and the hockey stick. Fig. 5-5 shows that the our assumption of using a parabolic model for  $\alpha(t)$  agrees very well with our experimental results.

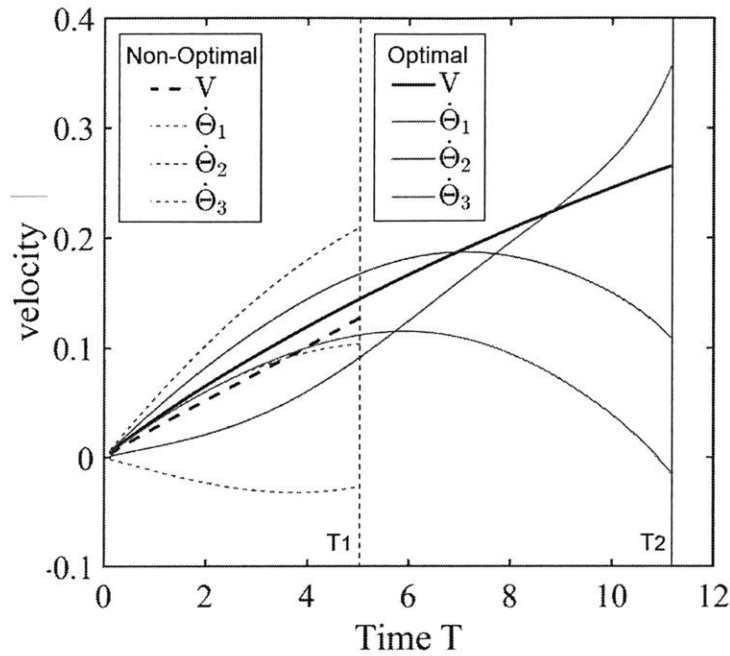


Figure 5-7: Simulation results of the angular velocity  $\dot{\Phi}_1$ ,  $\dot{\Phi}_2$ ,  $\dot{\Phi}_3$  and  $V$  for a non-optimal condition and an optimal condition. The  $T_1$  and  $T_2$  cycle indicate the non-optimal and optimal condition, respectively.

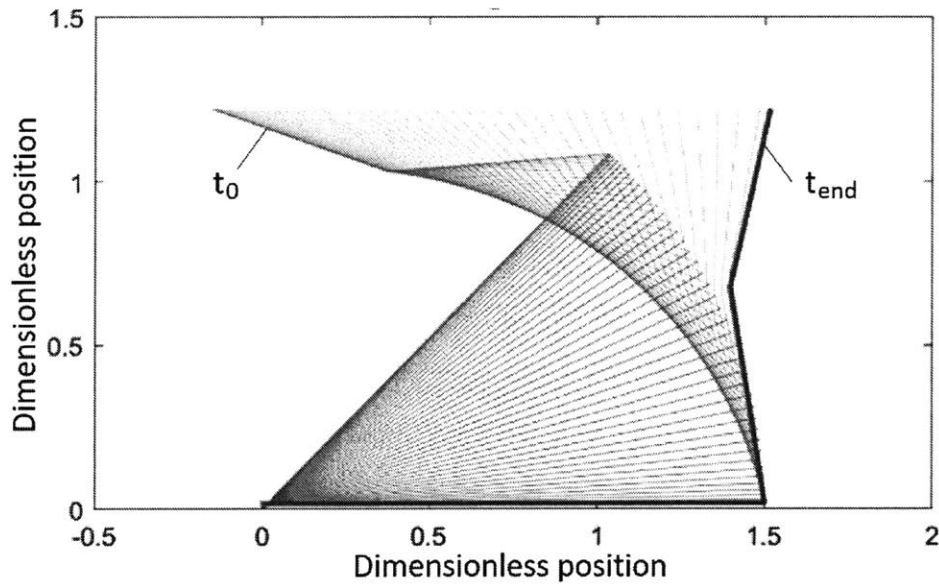


Figure 5-8: Simulation results for the upper arm (blue), the forearm (blue) and hockey stick (brown) during the first cycle of propulsion. At  $t_0$ , the hockey player places arms and the hockey stick at the optimal position. At  $t_{end}$ , the first propulsion ends due to the violation of at least one of the constraints. During this first cycle, the player attempts his/her best effort which is governed by the muscle's Hill model.

## 5.2.2 Parametric Optimization

In one scenario, the objective function is proposed as the average speed of the sled  $\bar{V}^{(i)}$  for the  $i$ th-cycle propulsion to be maximized. The motion of the upper arm, forearm and wrist are given by the column vector  $\Theta = [\Theta_1, \Theta_2, \Theta_3]^T$ . The start position and the end position of  $\Theta_s = [\Theta_{1s}, \Theta_{2s}, \Theta_{3s}]^T$  and  $\Theta_e = [\Theta_{1e}, \Theta_{2e}, \Theta_{3e}]^T$  also remains to be optimized. Thus,

$$(\Theta^*, \Theta_s^*, \Theta_e^*) = \arg \max_{(\Theta, \Theta_s, \Theta_e)} \bar{V}^{(i)} \quad (5.37)$$

One of the constraints comes from the power limit governed by the muscle Hill model, which tells us the maximum force  $F_M$ . Given the decoupled independence of this power constraint, we suggest the parameters remain to be optimized at the base condition of  $(\alpha, F) = \arg \max \dot{V}^{(i)}$ . In our hypothesis, to achieve the optimal performance by maximizing the average speed as defined in each cycle, the local acceleration should be optimized:

$$\begin{aligned} (\Theta^*, \Theta_s^*, \Theta_e^*) &= \arg \max_{(\Theta, \Theta_s, \Theta_e)} \bar{V}^{(i)} \\ &= \arg \max_{(\Theta, \Theta_s, \Theta_e)} \bar{V}^{(i)} \Big|_{(\alpha, F) = \arg \max \dot{V}^{(i)}} \end{aligned} \quad (5.38)$$

In the course of a linear motion, a sled hockey player performs multiple propulsion using the hockey sticks. One stroke of a propulsion process includes two stages: a propelling stage and a sliding stage. During the propelling stage, the player uses hockey sticks to propel, and the sled accelerates; during the sliding stage, the player retracts the hockey sticks to the start position for the next propelling stage, and the sled decelerates due to the friction between the skate blades and the ice surface. For the first stroke, there is no sliding stage from the previous stroke. Starting from the second stroke, we need to consider both stages because the sliding stage significantly affects the optimization results of the start position; we also take into account the deceleration due to the sliding friction. Thus,

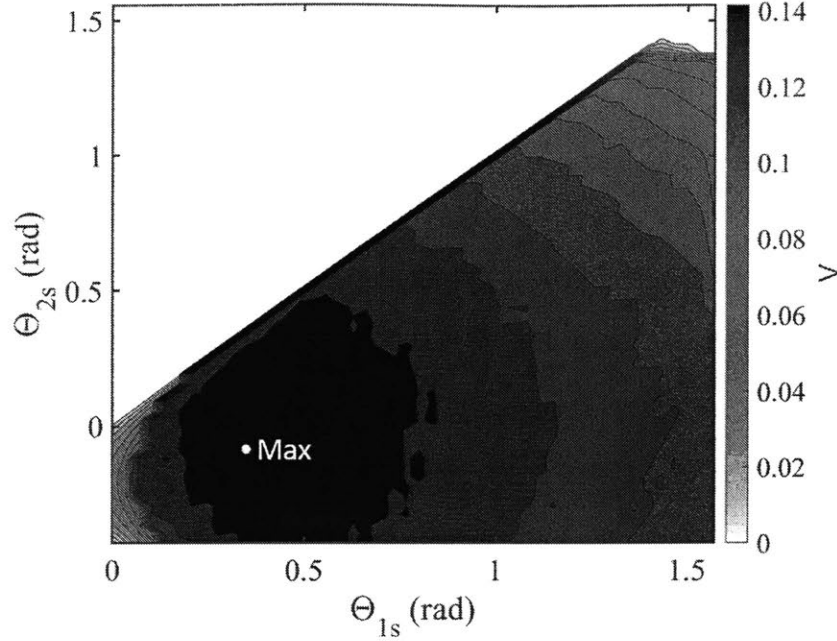


Figure 5-9: Simulation results for the dimensionless average velocity  $V$  during the first cycle of propulsion for  $\Phi_s$  ranging from 0 rad to 1.5 rad and  $\Phi_{2s}$  ranging from -0.5 rad to 1.5 rad. The upper-left white triangle area indicates no results from simulation due to the constraint  $\Phi_{1s} > \Phi_{2s}$ .

$$\begin{aligned} \bar{V}^{(i)} &= \frac{\int_{T_{ip}} V dt}{T_{ip}}, \quad i = 1; \\ \bar{V}^{(i)} &= \frac{\int_{T_{ip}} V dt + \int_{T_{is}} V|_{T=\sum_1^{i-1}(T_{ip}+T_{is})} dt - \int_{T_{is}} C_f^{\parallel} g t / (L_0 v_M^2) dt}{T_{ip} + T_{is}}, \quad i \geq 2, \end{aligned} \quad (5.39)$$

where  $T_{ip}$  and  $T_{is}$  are the duration during the propulsion and sliding of the sled respectively,  $C_f^{\parallel}$  is the friction coefficient when the direction of the frictional reaction force is parallel to the longitudinal direction of the skate blade.

The overall average velocity  $V$ , intuitively, is roughly set by the integration of the local acceleration over the duration of propulsion. As shown in Fig. 5-7, with the optimal parameters, the duration of propulsion is longer than that under the non-optimal condition and the local acceleration is slightly larger than the counterpart. The overall average velocity under the optimal condition is approximately as twice as large of that under non-optimal condition. Fig. 5-8 shows the simulation results for the motion of upper arm, lower arm and hockey stick with the optimal conditions for the first stroke of propulsion. In the simulation, the sled hockey players starts and



ends at the optimized position  $\Theta_s^*$  and  $\Theta_e^*$ , respectively, and the propulsion process follows the corresponding optimal dynamics during the first cycle of propulsion.

Furthermore,  $\beta_3$  is set by the design of the sled, which can be utilized to optimize the performance of propulsion. In addition, sled hockey players have much more freedom to determine  $\beta_s$  by varying the holding position of the hockey stick. Therefore, we propose another optimization problem to customize the sled design with the optimal propelling strategy:

$$\begin{aligned} (\beta_s^*, \beta_3^*) &= \arg \max_{(\beta_s, \beta_3)} \bar{V}^{(i)} \\ &= \arg \max_{(\Theta, \Theta_s, \Theta_e)} \bar{V}^{(i)} \Big|_{(\Theta = \Theta^*, \Theta_s^*, \Theta_e^*)} \end{aligned} \tag{5.40}$$

### 5.3 Tip-Over and Reset

Tip-Overs occur very often in the game of sled hockey. The lose of control of sled stability may result in a tip-over, especially during the process of reaching out for a puck or making a sharp turn in the ice rink. In addition, a tip-over can be utilized as a strategy to manipulate the puck control. In any circumstances, the process of reset, after a tip-over occurs, is of importance. A slow or struggling process of reset will undermine the performance of the sled hockey player. Understanding the dynamics in the process of tip-over and reset may shed light on the optimization of sled designs and sled driving strategy.

#### 5.3.1 Dynamical Modelling of Tip-Over and Reset

We consider the sled together with the sled hockey player approximately as one rigid body. To obtain the equation of motion to describe the process of reset after a tip-over of the hockey sled occurs, we first apply the conservation law of linear momentum:

$$\frac{d\mathbf{P}}{dt} = \sum \mathbf{F}, \tag{5.41}$$

where  $\mathbf{P}$  is the linear momentum of the rigid body and  $\mathbf{F}$  is the force exerted on the rigid body. Then, we apply the conservation law of angular momentum:

$$\frac{d\mathbf{H}_c}{dt} + \mathbf{r}_{AC} \times \frac{d\mathbf{P}}{dt} = \sum \mathbf{T}_A, \quad (5.42)$$

where  $\mathbf{H}_c$  is the angular momentum of the rigid body with respect to the center of mass  $C$  and  $\mathbf{T}_A$  is the torque exerted on the rigid body with respect to point A. The explicitly full form of the above system of equations is given in Section 5.1.1. To obtain the dynamics of the hockey sled during the process of reset, we may apply the constraints to the derived system of equations. For a successful reset, the motion should be constrained in the  $xz$ -plane and the contact point A between ice and skate blade should be fixed. Thus, the constraints are:

$$\begin{aligned} \ddot{\phi} &= \ddot{X} = \ddot{Y} = 0, \\ \dot{\phi} &= \dot{X} = \dot{Y} = \dot{R} = 0, \\ \phi &= \forall, X = \forall, Y = \forall, R = \forall. \end{aligned} \quad (5.43)$$

The reduced system of equations of motion applying the linear momentum conservation is given by:

$$\begin{aligned} 0 &= f_{\parallel} + f_x, \\ \ddot{\theta}(-mb_z) + \dot{\theta}^2(-mb_y) &= (N_1 + N_2) \sin \theta - mg \sin \theta - f_{\perp} \cos \theta + f_y, \\ \ddot{\theta}(mb_y) + \dot{\theta}^2(-mb_z) &= (N_1 + N_2) \cos \theta - mg \cos \theta + f_{\perp} \cos \theta + f_z, \end{aligned} \quad (5.44)$$

where  $f_{\parallel}$  and  $f_{\perp}$  are frictional forces, the directions of which are parallel and perpendicular to the longitudinal direction of the skate blade, respectively. The reduced system of equations of motion applying the angular momentum conservation is given

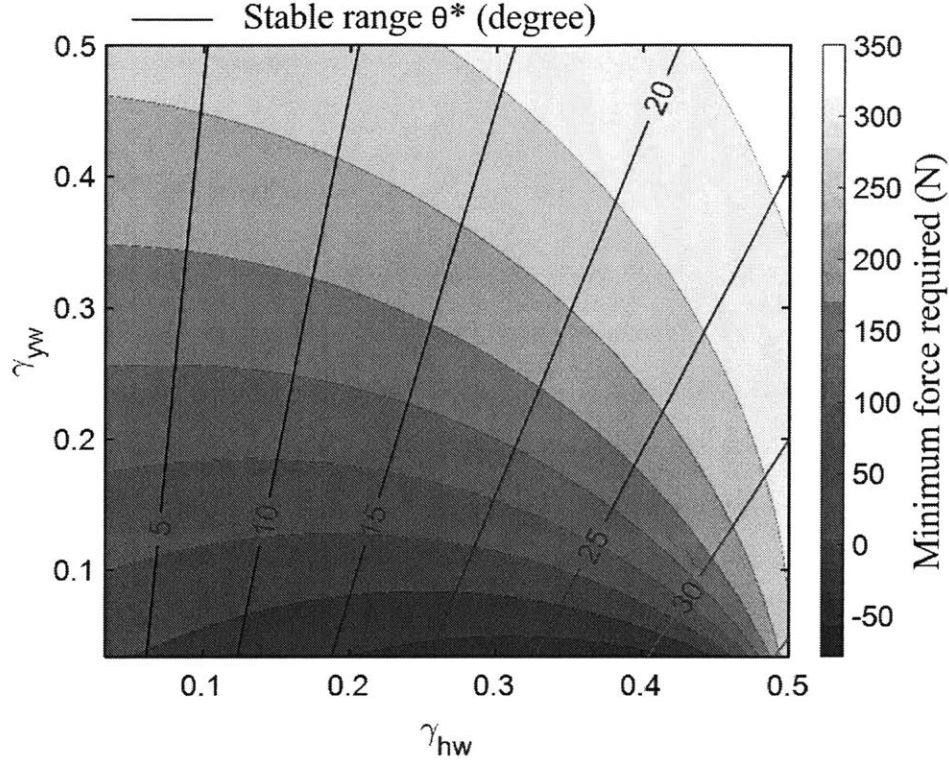


Figure 5-10: Minimum required force  $F_{req}^{min}$  to reset after a tip-over occurs and stable range  $\theta^*$  as a function of  $\gamma_{yw}$  and  $\gamma_{hw}$ .  $\gamma_{yw}$  and  $\gamma_{hw}$  both range from 0.01 to 0.5.

by:

$$\begin{aligned}
 \ddot{\theta}[I_{xx} + m(b_y^2 + b_z^2)] &= mg(b_z \sin \theta - b_y \cos \theta) + \tau_x, \\
 \ddot{\theta}(-mb_x b_y) + \dot{\theta}^2(mb_x b_z) &= (N_1 b_{x'} + N_2 b_x) \cos \theta + \tau_y, \\
 \ddot{\theta}(-mb_x b_z) + \dot{\theta}^2(-mb_x b_y) &= -(N_1 b_{x'} + N_2 b_x) \sin \theta + \tau_z.
 \end{aligned} \tag{5.45}$$

### 5.3.2 Parametric Optimization

The force required during the process of reset, exerted by the sled hockey player, manifests the efficiency and effectiveness of the reset. The design of sled, in return, affects the range of required forces, determining the performance of a hockey player given a tip-over occurs. In this section, we derive the range of the required force and optimize the parameters of sled design based on the dynamics during reset.

If the lower bound of the range for the required force,  $F_{req}^{min}$ , exceeds the maximum force that the hockey player could produce, in particular for junior players, a reset

will be unfeasible. A successful reset requires both of the acceleration and the angular velocity of the sled smaller than zero, in terms of the coordinate  $\theta$  as shown in Fig. 5-3, and both of the normal forces larger than zero. To obtain  $F_{req}^{min}$ , we have the conditions:

$$\begin{aligned}\ddot{\theta} &\leq 0, \\ \dot{\theta} &\leq 0, \\ N_1 &\geq 0, \\ N_2 &\geq 0.\end{aligned}\tag{5.46}$$

Plugging the above conditions into the system of equations - Eqn. 5.44 and Eqn. 5.45, we solve for  $F_{req}^{min}$  when the critical condition holds:

$$\begin{aligned}F_{zreq}^{min} &= \frac{mg(b_z \sin \theta - b_y \cos \theta)}{L_{tot} \sin \theta_0}, \\ F_{req}^{min} &= F_{zreq}^{min} / \cos \alpha.\end{aligned}\tag{5.47}$$

where  $F_{zreq}^{min}$  is the minimum force required in  $z$ -direction,  $\alpha = \tan^{-1}(\sin \theta_0 - \sin \theta) / \cos \theta$ ;  $\theta_0 = \pi/2 - \tan^{-1}(w_s - b_y) / (h - h_b)$ , which is the value of  $\theta$  at the position of tip-over.  $w_s$  is the width of the sled bucket and  $h$  is the height of the skate blades.

We further explore the design space to investigate the minimum required force,  $F_{req}^{min}$ , from the perspective of structural parameters. We first define the ratio  $\gamma_{yw} = y_b / w_s$ , where  $y_b$  is the distance between the skate blade to the center of mass as shown in Fig. 5-3, and  $w_s$  is the sled bucket width. We also define the ratio  $\gamma_{hw} = h_b / w_s$ , where  $h_b$  is the skate blade height. In addition, during the process of reset from a tip-over position, the sled hockey player needs to exert a reset force by pushing the ice surface until the center of mass of the sled passes over the pivot point A (see Fig. 5-3), the angle of which is defined as the stable angle  $\theta^*$ . Fig. 5-10 shows the minimum required force force  $F_{req}^{min}$  to reset after a tip-over occurs and stable range  $\theta^*$  as a function of  $\gamma_{yw}$  and  $\gamma_{hw}$ . As  $\gamma_{yw}$  increases,  $F_{req}^{min}$  increases drastically due to a higher potential energy required for reset. The regime where  $F_{req}^{min} < 0$  indicates

that no external force is required to reset, because the center of mass of the sled lies within the stable range  $\theta^*$  when tip-over occurs.

If the upper bound of the range for the required force,  $F_{req}^{max}$ , exceeds the maximum frictional reaction force between the skate blade and ice, the sled will slide on ice in place of reset, remaining the state of tip-over. The required force  $F_{req}$  is upper-bounded by the maximum static frictional force, the direction of which is perpendicular to the longitudinal direction of the skate blade:

$$F_y = F_z \tan \alpha \leq C_f^\perp N_2 = C_f^\perp \gamma (mg - F_z), \quad (5.48)$$

where  $\alpha = \tan^{-1}(\sin \theta_0 - \sin \theta) / \cos \theta$ , and  $C_f^\perp$  is the frictional coefficient when the direction of the frictional force is perpendicular to the longitudinal direction of the skate blades. Thus,

$$F_{zreq}^{max} = \frac{C_f^\perp \gamma mg}{C_f^\perp \gamma + \tan \alpha}, \quad (5.49)$$

$$F_{req}^{max} = F_{zreq}^{max} / \cos \alpha.$$

where  $F_{zreq}^{max}$  is the maximum required force in  $z$ -direction.

The process of an effective reset requires the force exerted by the sled hockey player in the range from  $F_{req}^{min}$  and  $F_{req}^{max}$ . If the force, provided by the sled hockey player, is smaller than  $F_{req}^{min}$ , the magnitude of the force is too small to reset the hockey player back to his/her initial upright position; if the force is larger than  $F_{req}^{max}$ , the required perpendicular frictional reaction force is larger than the maximum static frictional force, resulting in the sled sliding on ice. This range depends on the design parameters of hockey sled. We take two examples,  $\gamma_{yw} = \gamma_{hw} = 0.5$  and  $\gamma_{yw} = \gamma_{hw} = 1$ , to analyze the effective range of required force. As shown in Fig. 5-11, for  $\gamma_{yw} = \gamma_{hw} = 0.5$ , the effective range is from 120 N to 260 N; for  $\gamma_{yw} = \gamma_{hw} = 1$ , there is no valid effective force, i.e.  $F_{req}^{min} > F_{req}^{max}$ , meaning that if the design of parameters is  $\gamma_{yw} = \gamma_{hw} = 1$ , it is impossible for the sled hockey player to reset.

We further explore the entire space of design parameters to investigate the effective

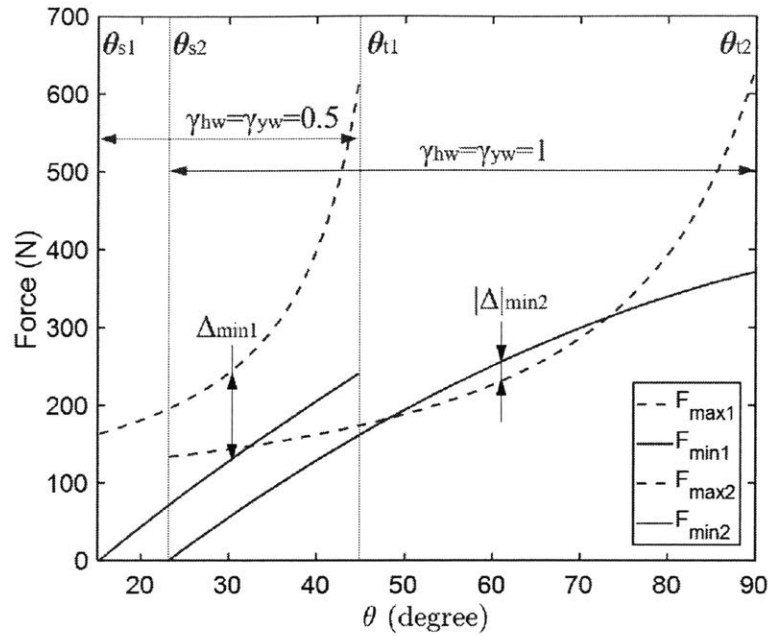


Figure 5-11: Maximum and minimum of the required force for reset as a function of the lean angle  $\theta$  for  $\gamma_{yw} = \gamma_{hw} = 0.5$  and  $\gamma_{yw} = \gamma_{hw} = 1$ .  $|\Delta_{min}|$  represents the minimum range of the required force during the process of reset.

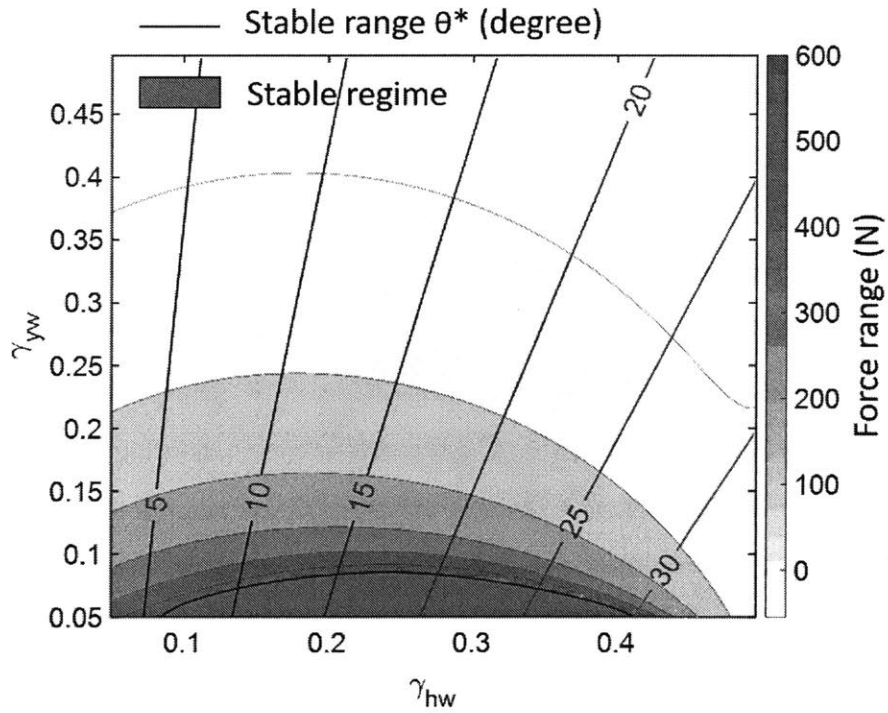


Figure 5-12: Effective ranges of required force for parameters of hockey sled, for  $\gamma_{yw}$  and  $\gamma_{hw}$  both ranging from 0.05 to 0.5. The stable range  $\theta^*$  is overlaid. The grey area indicates the stable range where no force is required to reset.

range of force (see Fig. 5-12). The smaller the effective range gets, the harder it is for the sled hockey player to reset. To maximize the feasibility of reset,  $\gamma_{hw} \approx 0.2$  and  $\gamma_{yw} < 0.2$  are preferable. We conclude that Fig. 5-10 and Fig. 5-12 can provide the guidance for designers to customize the hockey sleds for sled hockey players to help them achieve better performance.

# Chapter 6

## Tribology in Ice-Metal Contact

Tribology, studying friction, wear and lubrication of interacting surfaces in relative motion, sheds light on the field of bearings, metal-forming and transportation [100, 101]. Its history can be dated back to the record of documentation hundreds of years ago [102, 103]. Tribology is a highly interdisciplinary subject, including physics, chemistry, material science and mathematics [100, 101, 104].

Sled hockey is a competitive sport taking place in the ice rink. The friction between ice surface and skate blades varies the performance of the hockey stop, the hockey turn, the propulsion for linear motion and the process of reset after tip-over, which are discussed in previous chapters.

In this chapter, we investigate the tribology in the game of sled ice hockey. The conclusions of the study drawn on the physics of ice friction is still under debate in previous research [28]. We design an experimental system to mimic the ice rink environment and to expand the experimental study of the friction coefficient in an extensive range of Hersey number from  $10^{-13}$  to  $10^{-4}$ . To build the understanding of the physics of friction, we perform a dimensional analysis and an asymptotic analysis for three regimes of friction - boundary friction regime, mixed friction regime, and hydrodynamic lubrication regime. In addition, we provide a parametric model - multi-linear regression and a non-parametric model - random forest regression for the friction coefficient, to present a modified Stribeck curve.



## 6.1 Background and Introduction

In this section, we start by introducing tribology and its application in ice hockey, followed by a brief description of three hypothesis to explain the physics of ice friction. We further discuss Stribeck curve describing the relationship between the friction coefficient and Hersey number. In the last, we review the current prevailing models for the friction coefficient.

### 6.1.1 What is Tribology in Ice Friction

Tribology, studying friction, wear and lubrication of interacting surfaces in relative motion, sheds light on the field of bearings, metal-forming and transportation [100, 101]. Its history can be dated back to the record of documentation hundreds of years ago [102, 103]. Tribology is a highly interdisciplinary subject, including physics, chemistry, material science and mathematics [100, 101, 104].

The study of ice friction, as a sub-field of tribology, dates back only to the 19th century [105]. Studies find a liquid-like layer on the surface of ice [105]. Utilizing different measuring techniques at temperatures ranging from -25 Celsius Degree to 0 Celsius Degree, the thickness of the liquid-like layer varies from 1 nm to 100 nm [105, 106], with the measurement of ice at reset. At high relative velocity of two contact surfaces, the thickness of the liquid-like layer is measured up to 50,000 nm [105]. The dependence on the measurement technique for the thickness of the liquid-like layer brings different conclusions for researchers, unsurprisingly. In particular, the origin of the liquid-like layer is still under controversy. Currently, there are three dominating hypothesis - surface melting, pressure melting and frictional heating.

In 1859, Faraday suggests that the existence of a liquid-like layer is an inherent property of ice [107]. Followed by further investigations, theoretical investigations using electrostatic interaction, subsurface pressure melting, free surface energy minimization, highly-disordered surface and experimental studies using low-energy electron diffraction (LEED) are applied to explain the presence of the liquid-like layer on the surface of ice [108, 109, 110, 111, 112, 113].

Early studies suggest that, in ice skating, the pressure is large enough to reduce the melting point of the ice, primarily contributing to the thickness of the liquid-like layer [114, 115, 116, 117]. Colbeck shows that only 0.005% of an ice skate blade is in contact with the ice surface, resulting in a very high pressure on the local surface of ice [114]. The pressure melting molecular dynamics simulations show that the melting point was found to drop significantly at high pressures [115, 117, 116]. For example, the dropped pressure is about 23 Celsius Degree at 2k bars compared with that at standard ambient pressure [116]. However, there are some facts which cannot be explained by the theory of pressure melting. For example, the friction coefficient between ice and slider on its surface remains small at low temperature ( $< -30$  Celsius Degree). Studies illustrate that the pressure required to reach the melting temperature is usually larger than the compressive failure stress in these small friction situations, which is not physically realizable [114].

Frictional heating is currently predominant in explaining the physics of ice friction [118, 119]. The friction between the ice surface and slider generates heat, which in return increases the temperature of local asperities. If up to the melting point, the local surface of ice melts to form the liquid-like layer. Studies on the modelling of friction coefficient using frictional heating as the dominating mechanism achieve very consistent agreement between the theoretical model and experimental results [118, 119]. We make a simple estimation of the heat generated by friction. The heat generating power is given by:

$$\dot{q}_A = \frac{F_f u}{A} = \frac{C_f F_n u}{A}, \quad (6.1)$$

where  $\dot{q}_A$  is the heat generating power per area,  $F_f$  is the frictional force,  $u$  is the velocity of the slider and  $A$  is the contact area between the slider and the ice surface. Assuming in the regime of hydrodynamic lubrication regime when the speed of the skate is high enough ( $> 3$  m/s), the heat generated can be shown as:

$$\dot{q}_v = \mu \left( \frac{du}{dh} \right)^2, \quad (6.2)$$

where  $\dot{q}_v$  is the heat generating power per volume,  $\mu$  is the viscosity of water,  $u$  is the velocity of the slider,  $h$  is the local thickness of the lubrication liquid-like layer. Under an over-simplified assumption that all of the heat is used to melt the ice surface into water, a 500  $\mu m$  liquid-like layer could be formed due to the frictional heating, indicating a sufficient heating power for the agreement of the results as observed in experiments.

### 6.1.2 Stribeck Curve

Stribeck curve is a fundamental concept in the field of tribology, to characterize the friction coefficient as a function of Hersey number [120, 121]. Hersey number is a dimensionless lubrication parameter, defined as [122]:

$$\text{Hr} = \frac{\mu v}{F_n/L}, \quad (6.3)$$

where  $\mu$  is the dynamic viscosity of the fluid as the lubricant,  $v$  is the speed of the fluid,  $F_n$  is the normal load and  $L$  is the length of the slider in the longitudinal direction.

Based on the physics of the friction mechanisms, the Stribeck curve can be decomposed into several regimes, which are still controversial. In one proposal, three regimes can be identified: boundary friction regime, mixed friction regime and hydrodynamic regime [120, 123]. In the regime of boundary friction, the two solid surfaces come into full asperity contact in absence of any liquid lubricating layer [120, 123]. The friction coefficient is very large due to the fact that the load is supported mainly by surface asperities [120, 123]. In the regime of hydrodynamic lubrication, the thickness of the lubricating layer between the two contact surfaces are larger than the height of asperities [120, 123]. The asperity contact is negligible, with the normal load fully supported by the hydrodynamic pressure. In the regime of mixed lubrication, the friction mechanism incorporates both mechanisms in the regimes of boundary friction and hydrodynamic friction [120, 123]. The normal load is supported by both asperities and the liquid lubricant with partial contact between two solid surfaces.

In the other proposal, the boundary friction regime is further decomposed into two regimes: a dry-friction regime and a boundary-friction regime [124]. Dry friction is defined to be the friction when the sliding contact of two surfaces is in the absence of any kind of lubricating layer and boundary is redefined as when the lubrication layer is few molecular layers [124].

Study shows that no dry friction exists for the contact between ice and other metal surfaces for a wide range of Hersey number [28]. In our study on the friction between skate blades and ice, we adopt the first proposal, where three regimes are identified in the Stribeck curve - boundary friction regime, mixed friction regime, and hydrodynamic lubrication regime.

### 6.1.3 Kinetic Friction of Ice

The friction coefficient depends mildly on the temperature within a range of  $\pm 20\%$  [125, 126, 127, 128]. Over the temperature ranging from -25 Celsius Degree to 0 Celsius Degree, the friction coefficient obtains its minimum between -7 and -2 Celsius Degree depending on the normal load, the relative speed and the slider material [125, 126, 127, 128]. As the temperature increases, the friction coefficient is experimentally measured to decrease gradually before it reaches the minimum and then to arise abruptly from the minimum point [125, 126, 127, 128].

The relationship between friction coefficient  $C_f$  and the relative velocity  $v$  varies in different regimes defined by the Stribeck curve. In the mixed friction regime, the friction coefficient  $C_f$  scales roughly as  $C_f \sim v^{-1/2}$  [129, 127, 130]; in the hydrodynamic regime, the friction coefficient  $C_f$  scales roughly as  $C_f \sim v^{1/2}$ , based on the regression results from all the experiments in prior arts [130, 131, 132]. The magnitude of friction coefficient may vary one order away from each other based on the experimental setup.

Experimental results show no clear tendency for the friction coefficient on the apparent area of contact. Experimental results from Bowden shows little dependency on the contact area [133], while experimental results from Bourle suggest that the friction coefficient increases exponentially as the apparent contact area increases [130,

134]. The difference in their conclusions may result from their difference in samples and the experimental setups.

We find two predominant models for the friction coefficient. The first theoretical model was developed by Evans considering the ice friction governed by the frictional heating [135]. The total frictional heat  $Q_{tot}$  can be described as three components:

$$Q_{tot} = Q_s + Q_I + Q_M, \quad (6.4)$$

where  $Q_s$  is the heat conducted away from the slider,  $Q_I$  is the heat diffusing into ice and  $Q_M$  is the heat used for melting the ice surface. Evans further derives the friction coefficient  $C_f$  based on Eqn. 6.4:

$$C_f = \frac{C_A \lambda_s (T_m - T_0)}{F_n v} + \frac{C'_A \lambda_s (T_m - T_0)}{F_n v^{1/2}} + C_{fm}, \quad (6.5)$$

where  $T_m$  and  $T_0$  are the melting and ambient temperature respectively,  $\lambda_s$  is the thermal conductivity of the slider,  $C_A$  is a constant based on the apparent contact area between the slider and the ice surface,  $C'_A$  is an another constant based on the actual contact area between the slider and the ice surface,  $F_n$  is the normal force exerted on the slider,  $v$  is the relative velocity of the slider,  $C_{fm}$  is the friction coefficient resulting from melting [135].

The second theoretical model was developed by Oksanen accounting for the hydrodynamic friction based on Evans's model [136]. In the regime of hydrodynamic friction [136]:

$$C_f = \frac{n^{1/4} C_A^{3/4}}{F_n} \left( \frac{1}{2} \frac{1}{(2v)^{1/2}} [\Delta T_I (\lambda_I c_I \rho_I)^{1/2} + \Delta T_S (\lambda_S c_S \rho_S)^{1/2}] \right) + \frac{n^{1/4} C_A^{3/4}}{F_n} \left( \frac{1}{8v} [\Delta T_I (\lambda_I c_I \rho_I)^{1/2} + \Delta T_S (\lambda_S c_S \rho_S)^{1/2}]^2 + \eta_0 v h \rho_0 \right)^{1/2}, \quad (6.6)$$

where  $n$  is the number of discrete contacting points,  $C_A$  is a constant based on the actual contact area between the slider and the ice surface,  $\lambda_I$  and  $\lambda_S$  are thermal conductivity,  $c_I$  and  $c_S$  are the specific heat capacity and  $\rho_I$  and  $\rho_S$  are density, for

ice and the material of the skate blade, respectively [136].

## 6.2 Dimensional Analysis

We perform a dimensional analysis to further investigate the relationship between the friction coefficient, skate geometries, ice properties and motion parameters. The solution variable is selected to be the frictional force  $F_f$ . Our ultimate goal is to study the dimensionless friction coefficient  $C_f = F_f/F_n$ . Additional parameters are: the length of the blade  $L$ , the thickness of the blade  $W$ , the viscosity of water  $\mu$ , the Young's modulus of ice  $E$ , the relative velocity of blade with respect to ice  $v$ , and the normal force exerted on ice by the blade  $F_n$ . The resulting functional dependence between these seven parameters can be stated as:

$$f(F_f, L, W, \mu, E, v, F_n) = 0. \quad (6.7)$$

There are three independent dimensions in the selected variables. Based on the Buckingham's theorem, these seven variables can always be combined to form exactly four independent dimensionless parameter groups. Each dimensionless parameter group is commonly called a  $\Pi$ -group or a dimensionless group. Following a routine procedure of creating the dimensional matrix, determining the rank of the dimensional matrix, determining the number of dimensionless groups, we construct the dimensionless groups:

$$\begin{aligned} \Pi_1 &= C_f = F_f/F_n, \\ \Pi_2 &= L/W, \\ \Pi_3 &= \frac{\mu v}{F_n/L}, \\ \Pi_4 &= \frac{F/LW}{E}, \end{aligned} \quad (6.8)$$

where  $\Pi_1 = C_f$  is the friction coefficient,  $\Pi_2$  is the aspect ratio of skate blades,  $\Pi_3$  is the Hersey number, and  $\Pi_4$  quantifies the ratio of pressure on ice to the Young's

modulus of ice. The dimensionless relationship can be expressed as:

$$\frac{F_f}{F_n} = \phi \left( \frac{L}{W}, \frac{\mu v}{F_n/L}, \frac{F/LW}{E} \right), \quad (6.9)$$

where  $\phi$  is an undertermined function. Seven variables are reduced to four dimensionless groups, which significantly reduces the experimental effort.

### 6.3 Experimental System

Based on the dimensional analysis, we designed an experimental system to measure the friction coefficient  $C_f$  to quantify the relationship between the friction coefficient, skate geometries, ice properties and motion parameters.

We are particularly interested in the friction coefficient during the hockey slide and the hockey stop. Hockey slides and hockey stops are characterized by the direction of the skate blades and the direction of their motion. We, therefore, designed two geometries for the skate blades. As shown in Fig. 6-1, one geometry is a rectangular plate used to measure the friction coefficient  $C_f^\perp$ , where the frictional force  $F_f$  is perpendicular to the moving direction of the geometry; the other geometry is a thin-walled circular cylinder used to measure the friction coefficient  $C_f^\parallel$ , where the frictional force  $F_f$  is parallel to the moving direction of the geometry.

Our experimental system is designed to mimic the environment of an ice rink. As shown in Fig. 6-1, a sheet of ice is made by a Peltier plate, exposed to the ambient room temperature. We used a commercial stress-controlled shear rheometer (ARG2, TA Instruments) to precisely control the angular speed of the geometry and to measure the required torque. Rheometer is typically used for the measurement of fluid rheological property. We used rheometer in our experiments for the aim of high precision of angular speed control and of high precision of torque measurement instead. This experimental system is a scaled prototype for the scenario where the hockey skate blades are used in an ice rink by hockey players or sled hockey players.

We vary the dimensions of each type of geometries: for the rectangular plate, we

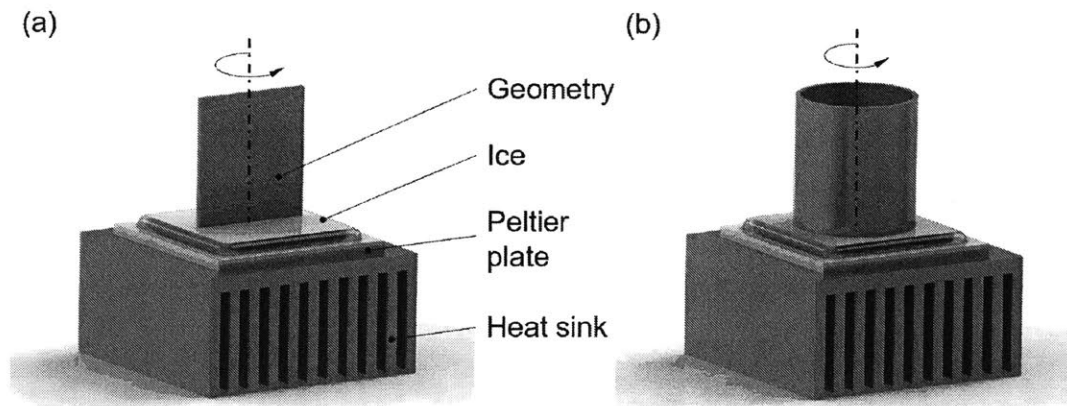


Figure 6-1: Experimental setup used to measure the friction coefficient  $C_f$ . (a) The geometry is a rectangular plate used to measure the friction coefficient  $C_f^\perp$ , where the frictional force  $F_f$  is perpendicular to the moving direction of the geometry. (b) The geometry is a thin-walled circular cylinder used to measure the friction coefficient  $C_f^\parallel$ , where the frictional force  $F_f$  is parallel to the moving direction of the geometry.

varied two thicknesses (0.2032 mm and 0.4064 mm) and three lengths (5 mm, 10 mm and 20 mm); for the thin-walled circular cylinder, we varied three diameters ( $\varnothing 5$  mm,  $\varnothing 10$  mm and  $\varnothing 20$  mm). In addition, we vary the angular velocities of the geometries: for the rectangular plate, we varied the angular velocity ranging from 0.5 rad/s to 5 rad/s; for the thin-walled circular cylinder, we varied the angular velocity ranging from 0.1 rad/s to 300 rad/s.

For a regular hockey stop, the Hersey number is around  $\mu v L / F_N \approx 10^{-11}$ ; for a regular hockey slide, the Hersey number is around  $\mu v L / F_N \approx 10^{-7}$ . Thus, our experiments should be designed to cover the range of Hersey number from  $10^{-12}$  to  $10^{-6}$ . The pressure on ice exerted by the skate of a hockey player is around  $F_N / LW \approx 10^6$  Pa. The parameters in our experiments are selected to cover the range around  $10^6$  Pa.

In the experiment, the angular velocity is controlled by the shear rheometer (ARG2), in the range of 0 to 300 rad/s. The normal force is passively measured, in the range from 0 N to 50 N; the torque is measured, in the range from 0 to 200 mN · m with a resolution of 1 nN · m.



## 6.4 Asymptotic Analysis

We perform an asymptotic analysis to investigate the frictional coefficient in a large range of Hersey number ranging from  $10^{-12}$  to  $10^{-4}$  and compare the theoretical results with the experimental results.

In section 6.4.1, we discuss the asymptotic analysis for elastohydrodynamic (EHD) contacts, where Hersey number ranges from  $10^{-7}$  to  $10^{-4}$ . In this regime, the direction of the motion of skate blades is parallel to the longitudinal direction of the blades. The friction coefficient  $C_f^{\parallel}$  is governed by the Reynolds equation. In section 6.4.2, we discuss two limit conditions of the asymptotic analysis for boundary contacts, where Hersey number ranges from  $10^{-9}$  to  $10^{-7}$ . In this regime, the direction of the motion of skate blades is parallel to the longitudinal direction of the blades. The friction coefficient  $C_f^{\parallel}$  is governed by the energy dissipation. In section 6.4.3, we discuss the dependency of the friction coefficient  $C_f^{\perp}$  on the contact area, the normal force and the relative velocity, where Hersey number ranges from  $10^{-13}$  to  $10^{-9}$ . In this regime, the direction of the motion of skate blades is the perpendicular to the longitudinal direction of the blades.

### 6.4.1 Asymptotic Analysis for Elastohydrodynamic Contacts

Elastohydrodynamic (EHD) lubrication develops the hydrodynamic lubrication for a pair of elastic contacts, which are prevalent in the field of tribology engineering, such as bearings and gears [137, 138, 139]. In our study, the regime of EHD contacts is bounded by Hersey number ranging from  $10^{-7}$  to  $10^{-4}$ . In this regime, the direction of the motion of skate blades is parallel to the longitudinal direction of the blades.

In 1886, Reynolds proposed a PDE as the first governing equation for the lubrication of EHD contacts, well-known as the Reynolds equation [140, 141]. Reynolds equation for an isothermal, incompressible lubricant in elastohydrodynamic (EHD) contacts can be expressed as [140, 141]:

$$\frac{\partial}{\partial x} \left( \frac{h^3}{12\mu} \frac{\partial P}{\partial x} \right) + \frac{\partial}{\partial y} \left( \frac{h^3}{12\mu} \frac{\partial P}{\partial x} \right) = \frac{U}{2} \frac{\partial h}{\partial x} + \frac{\partial h}{\partial t}, \quad (6.10)$$

where  $h$  is the local lubrication film thickness,  $P$  is the local pressure,  $U$  is the velocity of the upper boundary and  $\mu$  is the viscosity of Newtonian lubricant.

We adopt the Reynolds equation Eqn. 6.10 as the governing equation to study the friction coefficient between the ice surface and the skate blade. As a first-order approximation, we scale the terms in the equation, yielding the local thickness  $h$ :

$$h \sim (\mu LU/P)^{\frac{1}{2}}. \quad (6.11)$$

The friction coefficient  $C_f$  is defined as the ratio of the friction force  $F_f$  to the normal force  $F_n$ . In the limit of EHD, the friction force arises from the viscous force given by the product of shear stress and contact area  $\mu UWL/h$ . Thus,

$$C_f = \frac{F_f}{F_n} = \frac{\mu UWL/h}{PWL} \sim \frac{\mu U}{Ph} \quad (6.12)$$

By plugging in  $h$  into  $C_f$ , in the limit of elastohydrodynamic (EHD) contacts, the friction coefficient  $C_f$  follows:

$$C_f \sim \mu^{\frac{1}{2}} L^{-\frac{1}{2}} U^{\frac{1}{2}} P^{-\frac{1}{2}}. \quad (6.13)$$

Fig. ?? relates the friction coefficient  $C_f$  with the pressure  $P$ . The slope of the linear regression for our experimental results in log-log scale lies between -0.57 and -0.35, which reasonably agrees with the theoretical result -0.50. As the velocity of the slider in our experiments increases, the contact approaches the limit of EHD contacts; as a result, the experimental results increasingly agree with the theory.

## 6.4.2 Asymptotic Analysis for Mixed Contacts

In the regime of mixed friction, we consider the heat dissipation as the governing physics. The energy dissipation rate per unit volume with the friction as the heat source is given by:

$$\dot{E}_{dissp} = \kappa \nabla^2 T + \rho c \frac{\partial T}{\partial t} + \rho c_l \frac{\partial h}{\partial t}, \quad (6.14)$$

where  $h$  is the local lubrication film thickness,  $c$  is the specific heat,  $c_l$  is the specific latent heat,  $\kappa$  is the thermal conductivity and  $T$  is the temperature.

The friction coefficient  $C_f$  can be derived as [127]:

$$C_f = 1.88 \frac{T_f - T_a}{P^{0.75}} \left( \frac{\kappa \rho c}{U} \right)^{\frac{1}{2}} \left( \frac{n}{LW\bar{P}} \right)^{\frac{1}{4}}, \quad (6.15)$$

where  $T_f$  is the characteristic frictional temperature,  $T_a$  are temperature of approaching track,  $P$  is the local pressure,  $U$  is the velocity of the upper boundary,  $L$  is the length of the slider,  $W$  is the width of the slider,  $n$  is the number of discrete asperities. Therefore, in the regime of mixed friction,  $C_f \sim \bar{P}^{-\frac{1}{4}}$  in the situation of partial contact, and  $C_f \sim \bar{P}^{-1}$  in the situation of full contact. As shown in Fig. ??, the slope of the linear regression for our experimental results in log-log scale lies between -0.55 and -0.35, which are reasonably bounded by the theoretical results -1 and -0.25 respectively.

### 6.4.3 Asymptotic Analysis for Boundary Contacts

In the boundary friction regime, the friction coefficient is a constant, which is independent of the normal force, the contact area and the relative velocity of the two surfaces.

To measure the friction coefficient in lab environment, we scale down the size of the skate blade. The thickness of the blade is less than 2 mm; the length is larger than 200 mm. Thus, the aspect ratio of the skate blade  $W/L \approx 2\text{mm}/200\text{mm} \ll 1$ . The blades scratches the ice surface during a turn. The amount of ice it scratches may depend on the penetration depth. We, therefore, propose a hypothesis:

$$F_f = (C_f^\perp(\bar{P})\bar{P})^\gamma, \quad (6.16)$$

where  $F_f$  is the friction force,  $C_f^\perp(\bar{P})$  is the friction coefficient when the moving direction is perpendicular to the longitudinal direction of the blade,  $\bar{P}$  is the average pressure exerted on ice and  $\gamma$  is the power. In our hypothesis,  $C_f^\perp(\bar{P})$  depends on the

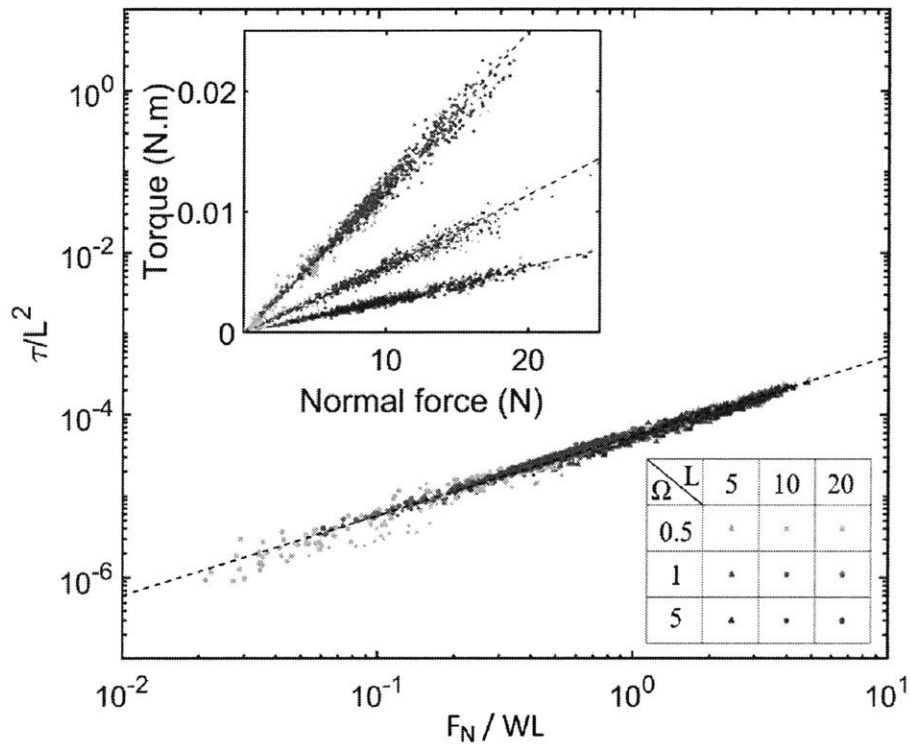


Figure 6-2:  $\tau/L^2$  versus  $F_N/WL$  for thickness  $W = 0.2032\text{mm}$ . (Inset) Torque (N·m) as a function of normal force (N) for three lengths,  $L$  (mm) and for three angular velocities,  $\Omega$  (rad/s). Dashed lines are linear regression lines. The slope of the linear regression line is 0.96.

average pressure  $\bar{P}$  and the unit of  $C_f^\perp$  should be adapted based on the value of  $\gamma$ . In the scenario of our experimental system, under the condition of our hypothesis, the torque  $\tau_f$  need to satisfy:

$$\tau_f = 2 \int_0^{L/2} \left( C_f^\perp(\bar{P}) \frac{F_N}{LW} \right)^\gamma x \, dx. \quad (6.17)$$

Alternatively, the above equation 6.17 can be reorganized as:

$$\frac{\tau_f}{L^2} \sim \left( \frac{F_N}{LW} \right)^\gamma. \quad (6.18)$$

Fig. 6-2 (Inset) shows the original experimental results using three lengths of the scaled blades with angular velocity ranging from 0.5 rad/s to 5 rad/s. To further examine the power  $\gamma$  in our hypothesis, we plotted  $\tau/L^2$  versus  $F_N/WL$  in log-log scale in Fig. 6-2. The linear regression in log-log scale informs us that the slope of the regression line is 0.96, which is very close to 1. Therefore, we propose that  $\tau/L^2$  and  $F_N/WL$  follows a linear relationship rather than a power-law relationship. Thus, the friction coefficient  $C_f$  can be expressed as:

$$C_f^\perp = \frac{4\tau_f W}{L F_N}. \quad (6.19)$$

Furthermore, we plotted  $4\tau/L$  versus  $F_N$  with thickness  $W = 0.2032\text{mm}$  for three lengths ( $L$ ) and for three angular velocities ( $\Omega$ ), and find that data collapse to one single line for a wide range of angular velocities, length scales and normal forces (see Fig. 6-3). We conclude that the friction coefficient  $C_f^\perp$  is independent of angular velocities, length scale and normal force within the scope of our experiments. Thus, the friction coefficient  $C_f^\perp$  can be redefined simply as  $C_f^\perp = F_f/F_N$ , where  $F_f$  and  $F_N$  are the frictional force and normal force respectively. The friction coefficient  $C_f^\perp$  using the linear regression is  $0.22 \pm 0.02$ .

We repeated all the experiments using another scaled skate blade with a thickness  $W = 0.4064\text{mm}$ , which is as twice thick as that in the previous experiments. All

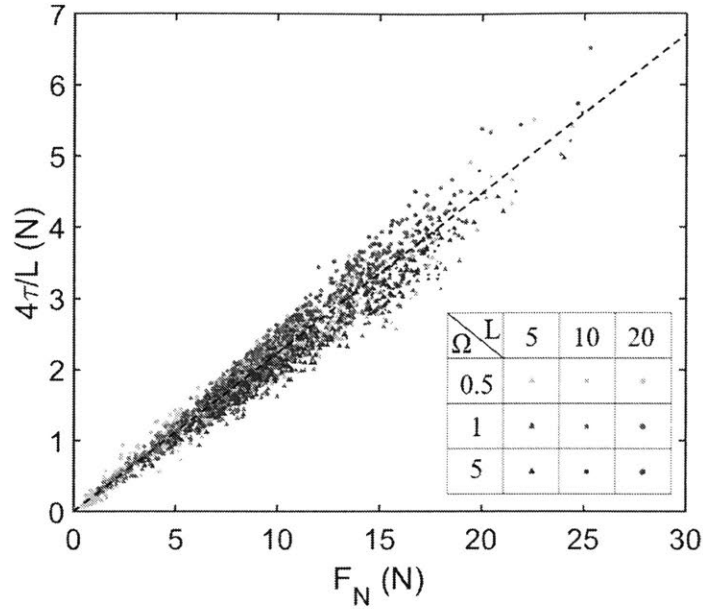


Figure 6-3:  $4\tau/L(N)$  versus  $F_N(N)$  for thickness  $W = 0.2032\text{mm}$  for three lengths,  $L$  (mm) and for three angular velocities,  $\Omega$  (rad/s). Dashed lines are linear regression lines. The slope of the linear regression line is  $0.22 \pm 0.02$ .

the conclusions stay true. The friction coefficient  $C_f^\perp$  using the linear regression is  $0.22 \pm 0.03$ , which is also consistent with the results in previous experiments. (see Appendix for the figures of the experimental results)

## 6.5 Modified Stribeck Curve for Friction Coefficient

In the field of tribology, Stribeck curve is widely used to characterize the friction coefficient as a function of Hersey number  $\text{Hr} = \mu v L / F_n$ . Based on the results from the dimensional analysis, asymptotic analysis and the experiments, we find that in the regime of boundary friction, the friction coefficient  $C_f^\perp$  is a constant about 0.22, independent of the dimensionless groups of Hersey number and pressure ratio. In the mixed regime, the friction coefficient  $C_f \sim U^{-\frac{1}{2}} P^{[-\frac{1}{4}, -1]}$ . In the regime of  $C_f \sim U^{\frac{1}{2}} P^{-\frac{1}{2}}$ . Fig. ?? shows the Stribeck curve for pressure ratio  $\gamma_p = P/E$  ranging from  $10^{-5}$  to  $10^{-2}$ , where  $E$  is the Young's modulus of ice, with our model using a

multi-linear regression in the logarithmic scale.

In ice hockey, the schemes of frequent intermittent skating can be categorized as hockey slide and hockey stop, the directions of which are parallel and perpendicular to the longitudinal direction of the skate blade, respectively. The corresponding Hersey number  $Hr$  for a hockey slide and a hockey stop are  $10^{-7}$  and  $10^{-11}$ , which locates at the transition from the mixed friction regime to the hydrodynamic lubrication regime and the boundary friction regime, respectively. The resultant friction coefficient in the different regimes varies one order in magnitude, in return, further verifying the adaptation of skating schemes to the physics of nature.

In addition, we compare this modified Stribeck curve to the Moody diagram and find their interesting analogy. Moody diagram relates the Darcy-Weisbach friction factor  $C_f$  to the Reynolds number  $Re$  [142, 143]. In the laminar flow regime, the friction factor  $C_f = 64/Re$ ; in the turbulent flow regime, friction factor depends on both Reynolds number  $Re$  and the roughness  $\epsilon$ . Our modified Stribeck curve relates the friction coefficient  $C_f$  to the Hersey number  $Hr$ . In the boundary friction regime,  $C_f = 0.22$ ; in the mixed friction regime and hydrodynamic regime, the friction coefficient depends on both  $Hr$  and pressure ratio  $P/E$ , where  $E$  is the Young's modulus of ice.

# Chapter 7

## Algorithms of Clustering for Physical Inference in Tribology

The physics of tribology of ice friction depends on the dimensionless groups (Hersey number  $Hr$ , pressure ratio  $\bar{P}$  and aspect ratio  $\psi$ ) discovered in Chapter 6. We found three regimes - elastohydrodynamic (EHD) contacts regime, mixed contacts regime and boundary contacts regime. To infer the physical regime with respect to the modified Stribeck curve, we developed a pipeline using clustering methodologies adapted from the field of data science.

This chapter starts with the restate of the results from dimensional analysis and asymptotic analysis. We present the algorithms for clustering models using K-means clustering and Gaussian mixture clustering, followed by the clustering results based on our experimental data.

### 7.1 Feature Extraction and Feature Selection

Our dimensional analysis and asymptotic analysis shows that in the regime of elastohydrodynamic (EHD) contacts, the friction coefficient  $C_f$  follows:

$$C_f^{\parallel} \sim \mu^{\frac{1}{2}} L^{-\frac{1}{2}} U^{\frac{1}{2}} P^{-\frac{1}{2}}, \quad (7.1)$$



where  $h$  is the local lubrication film thickness,  $P$  is the local pressure,  $U$  is the velocity of the upper boundary and  $\mu$  is the viscosity of Newtonian lubricant. In the regime of mixed contacts [127]:

$$C_f^{\parallel} = 1.88 \frac{T_f - T_a}{P^{0.75}} \left( \frac{\kappa \rho c}{U} \right)^{\frac{1}{2}} \left( \frac{n}{LW\bar{P}} \right)^{\frac{1}{4}}, \quad (7.2)$$

where  $T_f$  is the characteristic frictional temperature,  $T_a$  are temperature of approaching track,  $P$  is the local pressure,  $U$  is the velocity of the upper boundary,  $L$  is the length of the slider,  $W$  is the width of the slider,  $n$  is the number of discrete asperities. Therefore, in the regime of mixed friction,  $C_f \sim \bar{P}^{-\frac{1}{4}}$  in the situation of partial contact, and  $C_f \sim \bar{P}^{-1}$  in the situation of full contact. As shown in Fig. ??, the slope of the linear regression for our experimental results in log-log scale lies between -0.55 and -0.35, which are reasonably bounded by the theoretical results -1 and -0.25 respectively. In the regime of boundary contacts,

$$C_f^{\perp} = \frac{4\tau_f W}{LF_N} \approx 0.22 \pm 0.02, \quad (7.3)$$

indicating that  $C_f$  is independent of the Hersey number and pressure ratio.

The primary differences in physics that distinguish the three regimes of the modified Stribeck curve, therefore, is manifested by the power-law dependency of the friction factor  $C_f$  on the dimensionless groups, i.e. Hersey number  $Hr$  and pressure ratio  $\bar{P}$ . The experimental results are scattered data with features  $(C_f, Hr, \bar{P})$ . We aim for the partial derivatives  $\partial C_f / \partial Hr$  and  $\partial C_f / \partial \bar{P}$  as indispensable features. These partial derivatives are unfeasible to be estimated from the scattered data, because in the experimental scenario, neither  $Hr$  nor  $\bar{P}$  are kept as constants for the experiments or even the subgroup of the experiments. Empirical trials with sliced data to estimate the partial derivatives result in substantial noise.

We perform regression on the entire data set, followed by a small neighbourhood perturbation with respect to  $Hr$  and  $\bar{P}$ , to estimate the partial derivatives  $\partial C_f / \partial Hr$  and  $\partial C_f / \partial \bar{P}$ , respectively, serving as two new features in the following clustering.

## 7.2 Algorithms for Clustering Model

Clustering is a process of grouping subsets of elements in the available space, widely used in many engineering and science context [144, 145, 146]. In prior arts, a large amount of clustering algorithms have been developed and implemented with their own pros and cons[147, 148]. In this chapter, we will only cover two clustering algorithms that outperform the others with our experimental data.

### 7.2.1 K-Means Clustering

Given a set of observations (input)  $(\mathbf{x}_1, \mathbf{x}_2, \dots, \mathbf{x}_n)$ , where  $\mathbf{x} \in \mathcal{R}^d$ ,  $k$ -means clustering method is applied to partition the observations (input) into  $k$  ( $\leq n$ ) clusters (sets)  $\mathbf{C} = \{C_1, C_2, \dots, C_k\}$  with the minimal error WCSS (within-cluster sum of squares), i.e.

$$\mathbf{C} = \arg \min_{\mathbf{C}} E = \arg \min_{\mathbf{C}} \sum_{i=0}^k \sum_{\mathbf{x}_j \in C_i} \|\mathbf{x} - \boldsymbol{\mu}_i\|_2^2, \quad (7.4)$$

where  $E$  is the error function and  $\boldsymbol{\mu}_i$  is the mean for the points in  $C_i$ , also known as the *prototype* in  $C_i$ .

The algorithm of the  $k$ -means clustering algorithm is:

---

**Algorithm 3** Pseudocode for  $k$ -means clustering algorithm

---

```
1: procedure  $k$ -MEANS( $\mathcal{D}$ ,  $k$ )
2:   Initialize prototypes  $\boldsymbol{\mu} = \{\mu_1, \mu_2, \dots, \mu_k\}$ .
3:   for iteration  $t = 1$  to  $T$  do
4:     for each observation  $\mathbf{x}_j$ ,  $j \in \{0, 1, \dots, n\}$  do
5:       Assign  $\mathbf{x}_j$  to cluster  $C_i$  with nearest prototype  $\mu_i$ 
6:     for each cluster  $C_i$  do
7:       Update prototype  $\mu_i \leftarrow \sum_{\mathbf{x}_j \in C_i} \mathbf{x}_j / \text{card}(C_i)$ 
8:     Compute error  $E \leftarrow \sum_{i=0}^k \sum_{\mathbf{x}_j \in C_i} \|\mathbf{x}_j - \boldsymbol{\mu}_i\|_2^2$ 
```

---

This time complexity for the first inner *for*-loop, in Algorithm. 3, is  $\mathcal{O}(nkd)$ , for the second inner *for*-loop is  $\mathcal{O}(nd)$ , for the error computation is  $\mathcal{O}(nd)$ . The algorithm may terminates when the iteration reaches its maximum, or when the elements in each cluster remains, or when the error  $E$  does not change significantly.

## 7.2.2 Gaussian Mixture Clustering

A random variable  $\mathbf{X} \in \mathcal{R}^d$  following the multivariate Gaussian distribution can be denoted as:

$$\mathbf{X} \sim \mathcal{N}_d(\boldsymbol{\mu}, \boldsymbol{\Sigma}_{d \times d}), \quad (7.5)$$

where  $\boldsymbol{\mu} \in \mathcal{R}^d$  is a  $d$ -dimensional mean vector  $\boldsymbol{\mu} = \mathbb{E}(\mathbf{X})$  and  $\boldsymbol{\Sigma}$  is a  $d$ -by- $d$  covariance matrix  $\boldsymbol{\Sigma} = \text{Cov}(\mathbf{X}_i, \mathbf{X}_j)$ . The probability density function is:

$$f_{\mathbf{X}}(x_1, \dots, x_d) = \frac{1}{(2\pi)^{k/2} \|\boldsymbol{\Sigma}\|_2^{k/2}} \exp\left(-\frac{1}{2}(\mathbf{x} - \boldsymbol{\mu})^T \boldsymbol{\Sigma}^{-1}(\mathbf{x} - \boldsymbol{\mu})\right). \quad (7.6)$$

In the context with clustering, for each input vector, i.e. observation  $\mathbf{X}_i$  conditioned on cluster  $j$ , follows:

$$\mathbf{X}_i | (C_i = j) \sim \mathcal{N}_d(\boldsymbol{\mu}_j, \boldsymbol{\Sigma}_j), \quad j \in \{1, 2, \dots, k\} \quad (7.7)$$

In the Gaussian mixture model, the probability density function

$$p(\mathbf{x}|\boldsymbol{\theta}) = \sum_{j=1}^k \phi_j \mathcal{N}(\mathbf{x}|\boldsymbol{\mu}_j, \boldsymbol{\Sigma}_j), \quad j \sim \text{Multinomial}(p_1, \dots, p_k), \quad (7.8)$$

where  $\boldsymbol{\theta}$  is the latent variable  $\boldsymbol{\theta} = (\boldsymbol{\phi}, \boldsymbol{\mu}_1, \dots, \boldsymbol{\mu}_k, \boldsymbol{\Sigma}_1, \dots, \boldsymbol{\Sigma}_k)$ ,  $\boldsymbol{\phi}$  is the mixture weights for each cluster.

Before taking the assignment of clustering into account, the *incomplete-data* loss function is defined as the conditional log-likelihood:

$$L(\boldsymbol{\theta}; \mathbf{x}) = \log \prod_{i=1}^n \sum_{j=1}^k \phi_j f_{\mathbf{X}_i}(\mathbf{x}_i; \boldsymbol{\mu}_j, \boldsymbol{\Sigma}_j), \quad (7.9)$$

After taking the assignment of clustering into account, the *complete-data* loss function is defined as the conditional log-likelihood:

$$L(\boldsymbol{\theta}; \mathbf{x}, \mathbf{C}) = \log \prod_{i=1}^n \prod_{j=1}^k [\phi_j f_{\mathbf{X}_i}(\mathbf{x}_i; \boldsymbol{\mu}_j, \boldsymbol{\Sigma}_j)]^{\mathbb{I}(C_j=j)}, \quad (7.10)$$

where  $\theta$  is the latent variable  $\theta = (\phi, \mu_1, \dots, \mu_k, \Sigma_1, \dots, \Sigma_k)$ , is an indicator function.

### 7.3 Clustering for Physical Inference in Tribology

Based on the results of asymptotic analysis, we propose a piece-wise multi-linear model to predict the friction coefficient. A more detailed discussion will be presented in Chapter 8. In order to perform the piece-wise multi-linear model, the regime that each data belong to needs to be determined ahead. The clustering algorithm is applied to cluster the data into three regimes based on the three dimensionless groups and their partial derivatives with respect to Hersey number  $H_r$ .

Results in Chapter 8 are duplicatedly shown as the following for readers convenience. We take the logarithmic form of the three dimensionless groups as our features due to the power-law relationship derived from the asymptotic analysis. For Hersey number from  $10^{-12}$  to  $10^{-9}$ , the contact between the skate blade and ice lies in the regime of boundary friction. The friction coefficient  $C_f^\perp$  is independent of all the three dimensionless groups  $\Pi_1$ ,  $\Pi_2$  and  $\Pi_3$ . For Hersey number from  $10^{-9}$  to  $10^{-7}$ , the contact between the skate blade and ice lies in the regime of mixed lubrication. The friction coefficient  $C_f^\parallel$  highly depends on Hersey number  $\Pi_2$  and the pressure ratio  $\Pi_3$ ; For Hersey number from  $10^{-7}$  to  $10^{-4}$ , the contact between the skate blade and ice lies in the regime of hydrodynamic lubrication. The friction coefficient  $C_f^\parallel$  primarily depends on Hersey number  $\Pi_2$ .

The results of the piece-wise multi-linear regression for the test set are shown in Fig. 8-2. The regression are performed for Hersey number in the ranges from  $10^{-12}$  to  $10^{-9}$  and from  $10^{-7}$  to  $10^{-4}$ . The  $R^2$  of both models are 0.97, with standard deviations less than 0.1. The prediction using this model achieves a very small prediction error for the test set. We only take the three dimensionless groups in logarithmic scale based on the conclusions from the asymptotic analysis. It suggests that using the three dimensionless groups achieves a slightly better (0.5%) test accuracy than using the original four features.

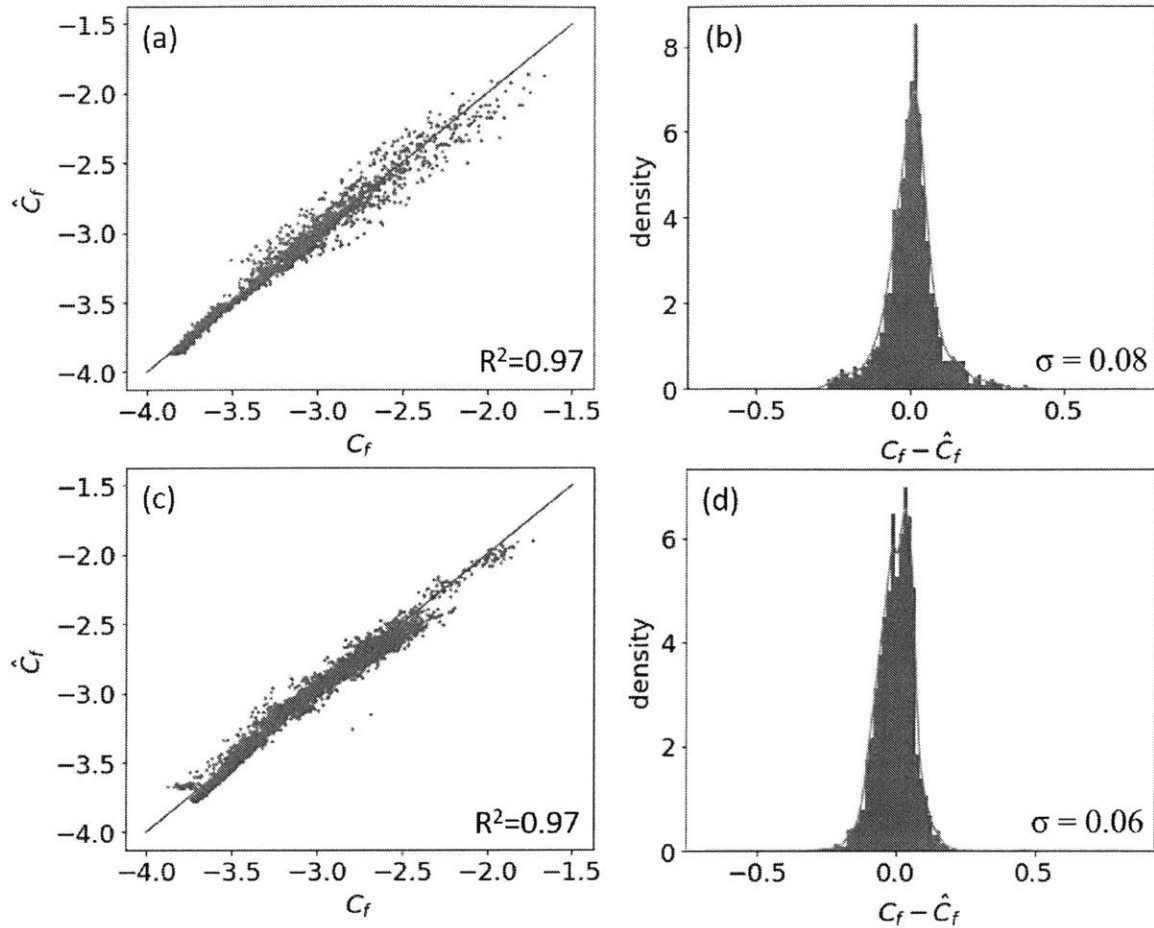


Figure 7-1: (a) Predicted friction coefficient  $\ln \hat{C}_f^{\parallel}$  versus experimental friction coefficient  $\ln C_f^{\parallel}$  using linear regression for Hersey number ranging from  $10^{-9}$  to  $10^{-7}$ . Three dimensionless groups are taken into account:  $\mathbf{X} = [\ln \Pi_1, \ln \Pi_2, \ln \Pi_3]$ . The diagonal blue line indicates the perfect prediction of  $\ln C_f^{\parallel}$ . The  $R^2$  of this model is 0.97. (b) Probability density as a function of the residual between the prediction and experimental results of friction coefficient  $\ln C_f^{\parallel} - \ln \hat{C}_f^{\parallel}$  using linear regression for Hersey number ranging from  $10^{-9}$  to  $10^{-7}$ . The orange line indicates a kernel density estimation (KDE). The standard deviation  $\sigma = 0.08$ . (c) Predicted friction coefficient  $\ln \hat{C}_f^{\parallel}$  versus experimental friction coefficient  $\ln C_f^{\parallel}$  using linear regression for Hersey number ranging from  $10^{-7}$  to  $10^{-4}$ . Three dimensionless groups are taken into account:  $\mathbf{X} = [\ln \Pi_1, \ln \Pi_2, \ln \Pi_3]$ . The diagonal blue line indicates the perfect prediction of  $\ln C_f^{\parallel}$ . The  $R^2$  of this model is 0.97. (d) Probability density as a function of the residual between the prediction and experimental results of friction coefficient  $\ln C_f^{\parallel} - \ln \hat{C}_f^{\parallel}$  using linear regression for Hersey number ranging from  $10^{-7}$  to  $10^{-4}$ . The orange line indicates a kernel density estimation (KDE). The standard deviation  $\sigma = 0.06$ .

# Chapter 8

## Algorithms of Regression for Stribeck Curve in Tribology

### 8.1 Background and Introduction

To the best of our knowledge, there does not exist any analytical or numerical models for the friction coefficient between ice and skate blades. Our experiments measuring the friction coefficient using rheometers are designed to mimic the real environment of ice rink, where the ice is made by a Peltier plate exposed to an ambient room temperature. Based on our experimental data, we propose a set of parametric and non-parametric models for the friction coefficient using machine learning techniques in an extensive range of Hersey number from  $10^{-12}$  to  $10^{-5}$ .

For each regression technique, we propose two models for the friction coefficient  $C_f (= \Pi_1)$ . The first one uses the original set of parameters, i.e. the blade length  $L$ , the blade thickness  $W$ , the water viscosity  $\mu$ , the Young's modulus of ice  $E$ , the relative velocity of blade with respect to ice  $v$ , and the normal force exerted on ice by the blade  $F_n$ ; the second one uses the dimensionless groups, i.e. the aspect ratio of skate blades  $\Pi_2 = L/W$ , the Hersey number  $\Pi_3 = \mu v L / F_n$ , and the ratio of pressure on ice to the Young's modulus of ice  $\Pi_4 = F / ELW$ . The first model applies all of the four experimental variables as features; the second model applies three dimensionless groups as features in the reduced form.

## 8.2 Algorithms for Statistical Model

### 8.2.1 Multi-Linear Regression

In this section 8.2.1, we first introduce the general derivation of multi-linear regression model based on high-dimensional data to predict a single dependent variable to minimize the sum squared error. We then fit and discuss a set of multi-linear regression models with the experimental results in a wide range of Hersey number from  $10^{-12}$  to  $10^{-5}$ .

Linear regression is the very simplest regression method. Despite of its limitation, we perform and compare the results of multi-linear regression using the original four features and using the reduced three dimensionless features with the physical insight drawn from dimensional analysis and asymptotic analysis.

To set up the problem of a multi-linear regression in general, we may consider  $p$  independent variables  $x_1, \dots, x_p$  and one dependent variable  $y$ . Suppose we have  $n$  ( $n > p$ ) observations,

$$y_i = \beta_0 + \beta_1 x_{i1} + \dots + \beta_p x_{ip} + \epsilon_i, \quad i = 1, \dots, n, \quad (8.1)$$

where  $\beta_i$  are the coefficients of the  $i$ -th dependent variable  $x_i$ . Our goal is to minimize the sum of squared residuals (errors)  $\epsilon_i$ . Thus, the cost function is:

$$\sum_{i=1}^n \epsilon_i^2 = \sum_{i=1}^n \left( y_i - \beta_0 - \sum_{j=1}^p \beta_j x_{ij} \right)^2, \quad (8.2)$$

In the vector and matrix representation, the dependent variable can be expressed in a more compact form:

$$\mathbf{y} = \mathbf{X}\boldsymbol{\beta} + \boldsymbol{\epsilon}, \quad (8.3)$$

where

$$\mathbf{y} = \begin{bmatrix} y_1 \\ \vdots \\ y_n \end{bmatrix}, \quad \mathbf{X} = \begin{bmatrix} 1 & x_{11} & \dots & x_{1p} \\ \vdots & \vdots & \ddots & \vdots \\ 1 & x_{n1} & \dots & x_{np} \end{bmatrix}, \quad \boldsymbol{\beta} = \begin{bmatrix} \beta_1 \\ \vdots \\ \beta_p \end{bmatrix}, \quad \boldsymbol{\epsilon} = \begin{bmatrix} \epsilon_1 \\ \vdots \\ \epsilon_n \end{bmatrix}. \quad (8.4)$$

Our goal is to find a  $\hat{\boldsymbol{\beta}}$  that minimizes the  $\|\boldsymbol{\epsilon}\|_2^2$  where  $\boldsymbol{\epsilon} = \mathbf{y} - \mathbf{X}\hat{\boldsymbol{\beta}}$ . Based on the orthogonality principle,  $\langle \mathbf{y} - \mathbf{X}\hat{\boldsymbol{\beta}}, \mathbf{X} \rangle = \mathbf{0}$ . Thus,

$$\mathbf{X}^T(\mathbf{y} - \mathbf{X}\hat{\boldsymbol{\beta}}) = 0. \quad (8.5)$$

Solving the above equation yields  $\hat{\boldsymbol{\beta}} = (\mathbf{X}^T \mathbf{X})^{-1} \mathbf{X}^T \mathbf{y}$  with the corresponding  $\hat{\mathbf{y}} = \mathbf{X}(\mathbf{X}^T \mathbf{X})^{-1} \mathbf{X}^T \mathbf{y}$ .

Alternatively, we may solve the over-constrained problem from the probabilistic perspective applying statistical theories. We formulate the problem, with a vector of output random variables  $\mathbf{Y}$ :  $\mathbf{Y} = [\mathbf{y}_1, \dots, \mathbf{y}_q]$ , where random variable  $\mathbf{y}_1 = [y_1^{(1)}, \dots, y_q^{(n)}]$ , with a vector of input random variables  $\mathbf{X}$ :  $\mathbf{X} = [\mathbf{x}_1, \dots, \mathbf{x}_p]$ , where random variable  $\mathbf{x}_1 = [x_1^{(1)}, \dots, x_1^{(n)}]$ . Our goal is to find a multi-linear estimator  $\hat{\mathbf{Y}}$ :

$$\hat{\mathbf{Y}} = \arg \min_{\hat{\mathbf{Y}}} \left\| \hat{\mathbf{Y}} - \mathbf{Y} \right\|_2^2. \quad (8.6)$$

We require the estimator unbiased,  $\mathbb{E}[\hat{\mathbf{Y}}] = \mathbb{E}[\mathbf{Y}]$ . Eqn. 8.6 can be achieved by the orthogonality condition,  $\mathbb{E}[(\hat{\mathbf{Y}} - \mathbf{Y})\mathbf{X}^T] = 0$ . Thus, the estimator  $\hat{\mathbf{Y}}$ :

$$\hat{\mathbf{Y}} = \mathbb{E}[\mathbf{Y}] + \frac{\text{Cov}(\mathbf{X}, \mathbf{Y})}{\text{Var}(\mathbf{X})}(\mathbf{X} - \mathbb{E}[\mathbf{X}]). \quad (8.7)$$

The two methods are essentially equivalent. In our application, the dependent variable is the friction coefficient  $\mathbf{y} = \mathbf{C}_f$ , and there are two choices of the independent variables  $\mathbf{X}$ . For features using original experimental variables,  $\mathbf{X} = [\mathbf{L}, \mathbf{W}, \mathbf{U}, \mathbf{F}]$ ; and for features using dimensionless groups,  $\mathbf{X} = [\ln \Pi_1, \ln \Pi_2, \ln \Pi_3]$ . Based on our asymptotic analysis, the dimensionless groups follow power-law relationships; we, thus, take the logarithmic of each dimensionless group.

We use Python Scikit-Learn package to apply the multi-linear regression and propose two sets of models - a multi-linear regression model and a piece-wise multi-linear regression model. In the first model, we perform a multi-linear regression model for the friction coefficient between ice and skate blade in a wide range of Hersey number from  $10^{-9}$  to  $10^{-5}$ . As shown in Fig. 8-1, the error of prediction for the friction



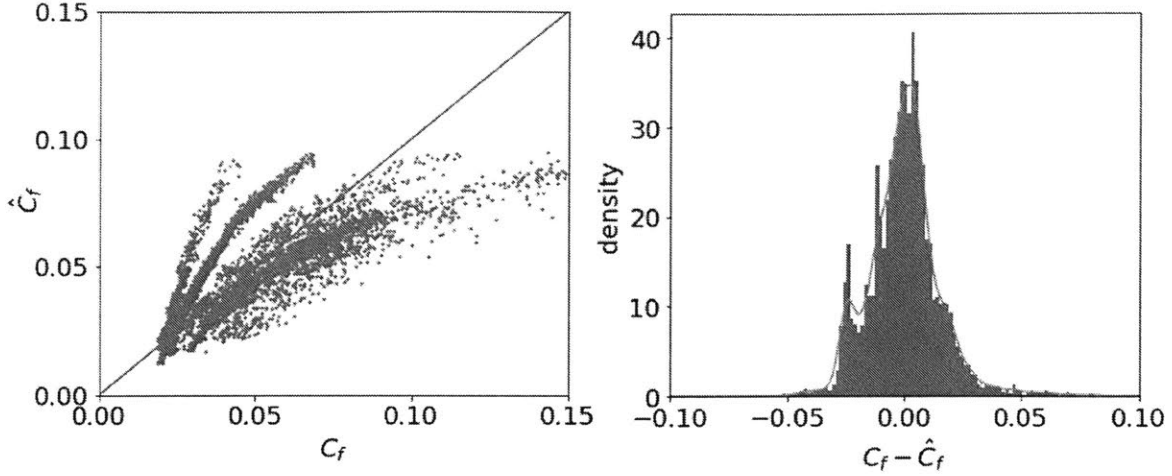


Figure 8-1: (a) Predicted friction coefficient  $\hat{C}_f^{\parallel}$  versus experimental friction coefficient  $C_f^{\parallel}$  using linear regression for Hersey number ranging from  $10^{-9}$  to  $10^{-5}$ . All the seven variables are taken into account:  $\mathbf{X} = [\mathbf{L}, \mathbf{W}, \mathbf{U}, \mathbf{F}, \mathbf{\Pi}_1, \mathbf{\Pi}_2, \mathbf{\Pi}_3]$ . The diagonal blue line indicates the perfect prediction of  $C_f$ . The  $R^2$  of the model is 0.57. (b) Probability density as a function of the residual between the prediction and experimental results of friction coefficient  $C_f^{\parallel} - \hat{C}_f^{\parallel}$  using linear regression for Hersey number ranging from  $10^{-9}$  to  $10^{-5}$ . The orange line indicates a kernel density estimation (KDE). The standard deviation of the residual is 0.015.

coefficient  $C_f$  is very large. The  $R^2$  of the model is 0.57 and the standard deviation of the residual is 0.015. The error of the model is unacceptably large. In this model, we take into account all the seven variables:  $\mathbf{X} = [\mathbf{L}, \mathbf{W}, \mathbf{U}, \mathbf{F}, \mathbf{\Pi}_1, \mathbf{\Pi}_2, \mathbf{\Pi}_3]$ . We also perform multi-linear regressions considering other sets of features:

$$\begin{aligned}
 \mathbf{X}_1 &= [\mathbf{L}, \mathbf{W}, \mathbf{U}, \mathbf{F}], \\
 \mathbf{X}_2 &= [\mathbf{\Pi}_1, \mathbf{\Pi}_2, \mathbf{\Pi}_3], \\
 \mathbf{X}_3 &= [\ln \mathbf{L}, \ln \mathbf{W}, \ln \mathbf{U}, \ln \mathbf{F}], \\
 \mathbf{X}_4 &= [\ln \mathbf{\Pi}_1, \ln \mathbf{\Pi}_2, \ln \mathbf{\Pi}_3], \\
 \mathbf{X}_5 &= [\ln \mathbf{L}, \ln \mathbf{W}, \ln \mathbf{U}, \ln \mathbf{F}, \ln \mathbf{\Pi}_1, \ln \mathbf{\Pi}_2, \ln \mathbf{\Pi}_3].
 \end{aligned} \tag{8.8}$$

The errors of multi-linear regression using any of the feature sets can not achieve acceptable predictions. (see Appendix to see the results using the rest of the feature sets) The errors primarily result from the nonlinear relationship between the friction coefficient and the accounted features. The Stribeck curve for the friction coefficient

in general can be referred to for understanding the nonlinearity.

Based on the results of asymptotic analysis, we propose a piece-wise multi-linear model to predict the friction coefficient. We take the logarithmic form of the three dimensionless groups as our features due to the power-law relationship derived from the asymptotic analysis. For Hersey number from  $10^{-12}$  to  $10^{-9}$ , the contact between the skate blade and ice lies in the regime of boundary friction. The friction coefficient  $C_f^\perp$  is independent of all the three dimensionless groups  $\Pi_1$ ,  $\Pi_2$  and  $\Pi_3$ . For Hersey number from  $10^{-9}$  to  $10^{-7}$ , the contact between the skate blade and ice lies in the regime of mixed lubrication. The friction coefficient  $C_f^\parallel$  highly depends on Hersey number  $\Pi_2$  and the pressure ratio  $\Pi_3$ ; For Hersey number from  $10^{-7}$  to  $10^{-4}$ , the contact between the skate blade and ice lies in the regime of hydrodynamic lubrication. The friction coefficient  $C_f^\parallel$  primarily depends on Hersey number  $\Pi_2$ .

The results of the piece-wise multi-linear regression for the test set are shown in Fig. 8-2. The regression are performed for Hersey number in the ranges from  $10^{-12}$  to  $10^{-9}$  and from  $10^{-7}$  to  $10^{-4}$ . The  $R^2$  of both models are 0.97, with standard deviations less than 0.1. The prediction using this model achieves a very small prediction error for the test set. We only take the three dimensionless groups in logarithmic scale based on the conclusions from the asymptotic analysis. It suggests that using the three dimensionless groups achieves a slightly better (0.5%) test accuracy than using the original four features.

## 8.3 Algorithms for Machine Learning Model

### 8.3.1 Random Forest Regression

We apply another non-parametric model for the regression of the friction coefficient, where the complexity of our hypothesis  $\mathcal{H}$  depends on our experimental data. In this section, we introduce the methodology of tree modelling and ensemble methods followed by an application of Random Forest to our experimental results for regression.

The scenario of tree method is to recursively partition the input space  $\mathcal{X}$  and fit

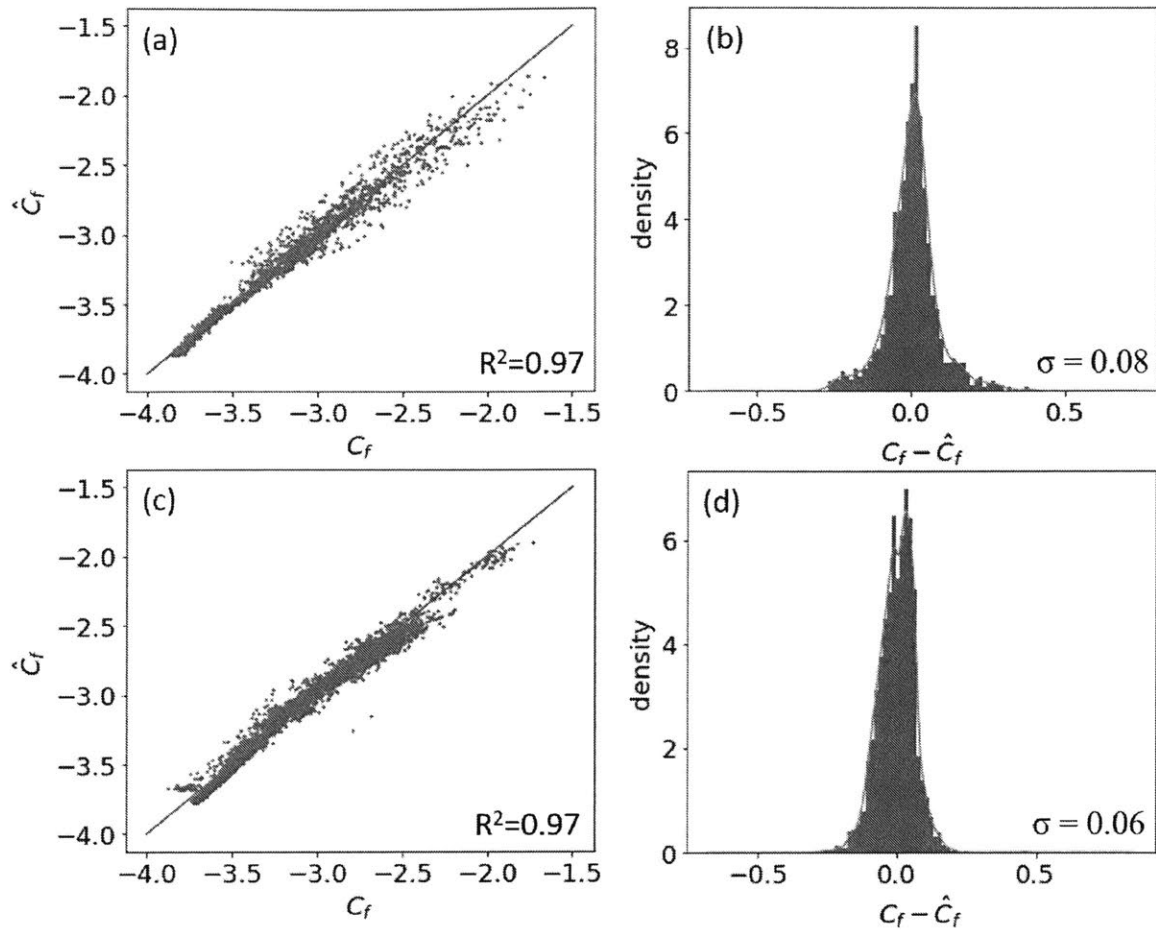


Figure 8-2: (a) Predicted friction coefficient  $\ln \hat{C}_f^{\parallel}$  versus experimental friction coefficient  $\ln C_f^{\parallel}$  using linear regression for Hersey number ranging from  $10^{-9}$  to  $10^{-7}$ . Three dimensionless groups are taken into account:  $\mathbf{X} = [\ln \Pi_1, \ln \Pi_2, \ln \Pi_3]$ . The diagonal blue line indicates the perfect prediction of  $\ln C_f^{\parallel}$ . The  $R^2$  of this model is 0.97. (b) Probability density as a function of the residual between the prediction and experimental results of friction coefficient  $\ln C_f^{\parallel} - \ln \hat{C}_f^{\parallel}$  using linear regression for Hersey number ranging from  $10^{-9}$  to  $10^{-7}$ . The orange line indicates a kernel density estimation (KDE). The standard deviation  $\sigma = 0.08$ . (c) Predicted friction coefficient  $\ln \hat{C}_f^{\parallel}$  versus experimental friction coefficient  $\ln C_f^{\parallel}$  using linear regression for Hersey number ranging from  $10^{-7}$  to  $10^{-4}$ . Three dimensionless groups are taken into account:  $\mathbf{X} = [\ln \Pi_1, \ln \Pi_2, \ln \Pi_3]$ . The diagonal blue line indicates the perfect prediction of  $\ln C_f^{\parallel}$ . The  $R^2$  of this model is 0.97. (d) Probability density as a function of the residual between the prediction and experimental results of friction coefficient  $\ln C_f^{\parallel} - \ln \hat{C}_f^{\parallel}$  using linear regression for Hersey number ranging from  $10^{-7}$  to  $10^{-4}$ . The orange line indicates a kernel density estimation (KDE). The standard deviation  $\sigma = 0.06$ .

simple hypothesis  $h$  in each region. The problem for regression tree method can be formulated: Given  $M$  regions  $R_1, \dots, R_M$  and the output values  $O_1, \dots, O_M$ . We may assume for each partition we fit a piecewise constant. Thus, our hypothesis  $\mathcal{H}$  is:  $\hat{y}(x) = O_m$  when  $x \in R_m$ . The squared error in each partition  $E_m$ :

$$E_m = \sum_{\{i|x^{(i)} \in R_m\}} (y^{(i)} - O_m)^2, \quad (8.9)$$

The cost function we minimize is the sum squared error with regularization:

$$E_{tot} = \sum_{m=1}^M E_m + \lambda M. \quad (8.10)$$

This optimization problem brings challenge for the differentiation of the cost function. Alternatively, a greedy algorithm is applied by starting with  $M = 1$ , then recursively and greedily dividing the input space  $\mathcal{X}$ . We define:

$$\begin{aligned} R_{j,s}^+(\mathbf{D}) &= \{x \in \mathbf{D} | x_j \geq s\}, \\ R_{j,s}^-(\mathbf{D}) &= \{x \in \mathbf{D} | x_j < s\}, \end{aligned} \quad (8.11)$$

where  $\mathbf{D}$  is the data set, and

$$\begin{aligned} \hat{y}_{j,s}^+(\mathbf{D}) &= \frac{1}{N_{j,s}} \sum_{\{i|x^{(i)} \in R_{j,s}^+(\mathbf{D})\}} y^{(i)}, \\ \hat{y}_{j,s}^-(\mathbf{D}) &= \frac{1}{N_{j,s}} \sum_{\{i|x^{(i)} \in R_{j,s}^-(\mathbf{D})\}} y^{(i)} \end{aligned} \quad (8.12)$$

The algorithm of the regression tree is:

---

**Algorithm 4** Pseudocode for Regression Trees

---

```

1: procedure BUILDTREE( $\mathbf{D}$ )
2:   if  $|\mathbf{D}| < k$  then
3:     return Leaf( $\mathbf{D}$ )
4:   else
5:     find  $(j, s) = \arg \min_{(j,s)} E_{R_{j,s}^+(\mathbf{D})} + E_{R_{j,s}^-(\mathbf{D})}$ 
6:     return Node( $j, s$ , BuildTree( $R_{j,s}^-(\mathbf{D})$ ), BuildTree( $R_{j,s}^+(\mathbf{D})$ ))

```

---

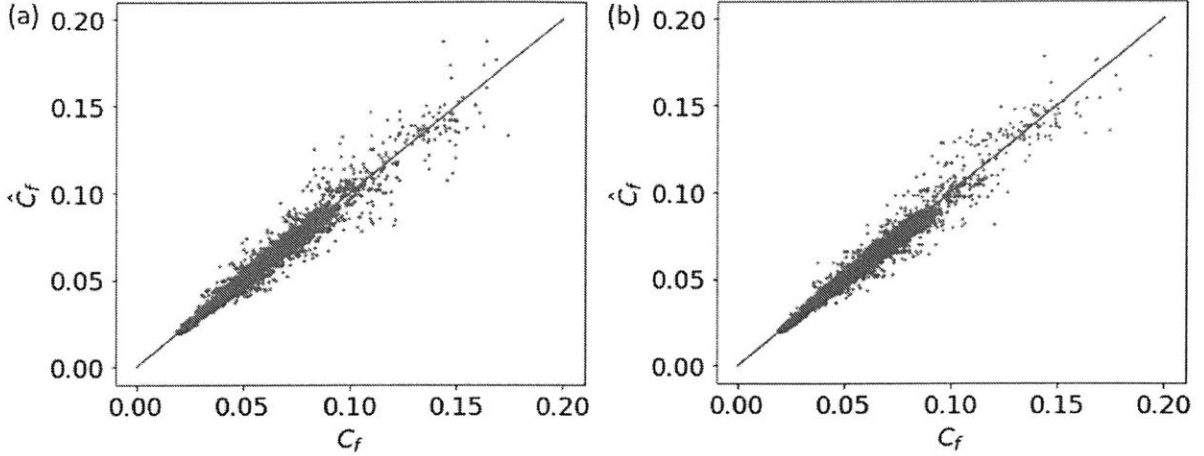


Figure 8-3: Predicted friction coefficient  $\hat{C}_f^{\parallel}$  versus experimental friction coefficient  $C_f^{\parallel}$  using Random Forest regression. (a) Regression results using original experimental variables, where  $\mathbf{X} = [\mathbf{L}, \mathbf{W}, \mathbf{U}, \mathbf{F}]$ . The diagonal blue line indicates the perfect prediction of  $C_f$ . The  $R^2$  of the model is 0.972. (b) Regression results using dimensionless groups, where  $\mathbf{X} = [\ln \Pi_1, \ln \Pi_2, \ln \Pi_3]$ . The diagonal blue line indicates the perfect prediction of  $C_f$ . The  $R^2$  of the model is 0.976.

Regression tree method can achieve high prediction accuracy on training data, while is difficult to generalize to other data sets due to the high variance [149, 150]. To compensate for this drawback, ensemble methods for regression tree are utilized to reduce the high variance [150, 151].

Random forests apply the bootstrapping aggregation ensemble (also known as bagging ensemble) on the regression trees. In the algorithm of random forests, we construct a subset  $\mathbf{B}$  of size  $n$  by sampling with replacement from dataset  $\mathbf{D}$ , and train a regression tree with each of the subset  $\mathbf{B}$  to obtain  $\hat{f}_b$ . The estimator of the random forest is the average response from all regression trees:

$$\hat{f}_{bag}(x) = \frac{1}{N_B} \sum_b \hat{f}_b(x), \quad (8.13)$$

where  $N_B$  is the number of the subsets or regression trees, and  $\hat{f}_b(x)$  is the regression trees estimator for each subset of the data.

We apply a random forests regression to predict the friction coefficient  $C_f$  between ice and skate blades. The results of the random forest regression are shown in Fig. 8-3

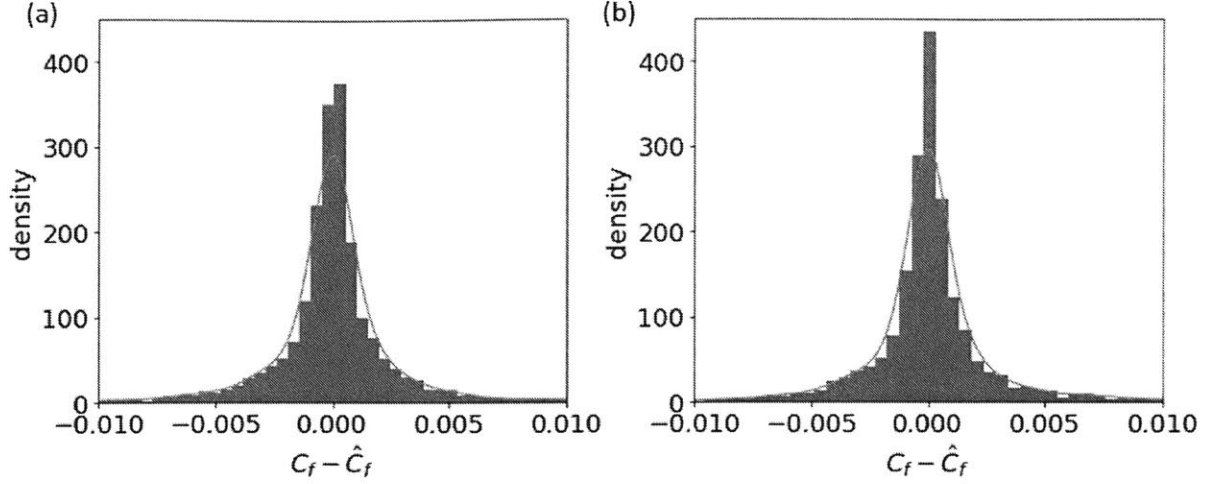


Figure 8-4: Probability density as a function of  $C_f - \hat{C}_f$  using Random Forest regression. (a) Regression results using original experimental variables, where  $\mathbf{X} = [\mathbf{L}, \mathbf{W}, \mathbf{U}, \mathbf{F}]$ ; (b) Probability density as a function of the residual between the prediction and experimental results of friction coefficient  $C_f^{\parallel} - \hat{C}_f^{\parallel}$  using dimensionless groups, where  $\mathbf{X} = [\ln \Pi_1, \ln \Pi_2, \ln \Pi_3]$ .

and Fig. 8-4. Using features  $\mathbf{X}_1 = [\mathbf{L}, \mathbf{W}, \mathbf{U}, \mathbf{F}]$  and  $\mathbf{X}_2 = [\ln \Pi_1, \ln \Pi_2, \ln \Pi_3]$  both achieve a high accuracy of prediction with  $R^2$  around 0.97. The features  $\mathbf{X}_2$  are obtained based on the results from dimensional analysis, which are essentially the dimensionless groups. The asymptotic analysis unveils the power-law relationship between the friction coefficient  $C_f$  and the Hersey number, suggesting to construct features  $\mathbf{X}_2$  in logarithmic scale. The results using three features in logarithmic scale  $\mathbf{X}_2$  shows a slightly higher accuracy than that using four features  $\mathbf{X}_1$ , which further verifies the conclusions from the dimensional analysis and the asymptotic analysis. In addition, we apply a random forests regression using alternative features:

$$\begin{aligned}
 \mathbf{X}_1 &= [\mathbf{L}, \mathbf{W}, \mathbf{U}, \mathbf{F}], \\
 \mathbf{X}_2 &= [\Pi_1, \Pi_2, \Pi_3], \\
 \mathbf{X}_3 &= [\ln \mathbf{L}, \ln \mathbf{W}, \ln \mathbf{U}, \ln \mathbf{F}], \\
 \mathbf{X}_4 &= [\ln \Pi_1, \ln \Pi_2, \ln \Pi_3], \\
 \mathbf{X}_5 &= [\ln \mathbf{L}, \ln \mathbf{W}, \ln \mathbf{U}, \ln \mathbf{F}, \ln \Pi_1, \ln \Pi_2, \ln \Pi_3].
 \end{aligned} \tag{8.14}$$

Using the metric of  $R^2$  of the models, in general, the accuracy of the prediction using dimensionless groups in logarithmic scale is higher than that using the original variables. (see Appendix for the regression results for  $\hat{C}_f$  versus  $C_f$  and their residual)

### 8.3.2 Neural Network Regression

The fundamental idea of neural network can be dated back to 1943, proposed by McCulloch and Pitts [152].

A *neuron*, also known as *node* or *unit*, is the basic element of a neural network, usually representing a non-linear function  $a = f(z) = f(\sum_{i=1}^m x_i w_i + w_0) = f(\mathbf{w}^T + \mathbf{w}_0)$ , where  $a \in \mathcal{R}$  is a single output scalar,  $f$  is an activation function,  $z$  is the pre-activation output,  $\mathbf{x} \in \mathcal{R}^m$  is an input vector,  $\mathbf{w} = [w_1, \dots, w_m]$  is a weight vector and  $w_0$  is an offset (threshold).

A *layer* consists of a set of *neurons*, also usually representing a non-linear function  $\mathbf{A} = f(\mathbf{z}) = f(\mathbb{W}^T \mathbf{X} + \mathbf{W}_0)$ , where  $\mathbf{A} \in \mathcal{R}^n$  is an output vector,  $f$  is an activation function applied element-wise,  $\mathbf{x} \in \mathcal{R}^m$  is an input vector,  $\mathbb{W} = [\mathbf{W}_1, \dots, \mathbf{W}_m]$  is a weight matrix and  $\mathbf{W}_0$  is an offset (threshold) vector.

A feed-forward *neural network* consists of a set of *layers*.  $\mathbf{A}^{(l)} = f^{(l)}(\mathbf{Z}^{(l)}) = f^{(l)}(\mathbb{W}^{(l)T} \mathbf{A}^{(l-1)} + \mathbf{W}_0^{(l)})$ , where the superscript  $l$  indicates that the corresponding variable is in  $l$ -th layer. The element-wise activation function  $f$  is usually a non-linear function (otherwise the *neural network* will be simplified as one single linear function of  $\mathbf{X}$ ), which can take many representations including the step function, rectified linear unit (known as *ReLU*), sigmoid function, hyperbolic tangent function and softmax function.

This parametric model for regression using feed-forward *neural network* with an associated loss function  $f_{loss}$  defines an optimization problem to explore the optimal weight matrix  $\mathbb{W}$  for each *neuron*. We opt to use gradient descent methods - batch gradient descent or stochastic gradient descent (SGD), train the *neural network*. We take SGD for instance to calculate  $\nabla_{\mathbb{W}} Loss(NN(x^{(i)}, \mathbb{W}), y^{(i)})$  by considering one single data point  $(x^{(i)}, y^{(i)})$ , where  $NN$  represents the overall function applying the *neural network* and  $Loss(\cdot, \cdot)$  is a scalar calculated by  $f_{loss}(\cdot, \cdot)$ . This gradient can be

obtained simply through a general process *error back-propagation*:

$$\frac{\partial Loss}{\partial \mathbb{W}^{(l)}} = \mathbf{A}^{(l-1)} \frac{\partial \mathbf{A}^{(l)}}{\partial \mathbf{Z}^{(l)}} \frac{\partial Loss}{\partial \mathbf{A}^{(L)}} \prod_{i=l+1}^L \mathbb{W}^{(i)} \frac{\partial \mathbf{A}^{(i)}}{\partial \mathbf{Z}^{(i)}}. \quad (8.15)$$

The algorithm of a fully-connected feed-forward *neural network* for regression is:

---

**Algorithm 5** Pseudocode for Feed-Forward Neural Network with SGD

---

```

1: procedure NN-SGD( $\mathcal{D}$ , T, L,  $\mathbf{m}$ ,  $\mathbf{f}$ )
2:   for layer  $l = 1$  to L do
3:      $W_{i,j}^{(l)} \sim \mathcal{N}(0, 1/m^l)$ 
4:      $W_0^{(l)} \sim \mathcal{N}(0, 1)$ 
5:   for  $t = 1$  to T do
6:      $i = \text{rand}\{1, \dots, n\}$ 
7:     for layer  $l = 1$  to L do
8:        $\mathbf{Z}^{(l)} = \mathbb{W}_{(l)}^T \mathbf{A}^{(l-1)} + \mathbb{W}_0^l$ 
9:        $\mathbf{A}^{(l)} = f^{(l)}(\mathbf{Z}^{(l)})$ 
10:     $Loss = f_{loss}(\mathbf{A}^{(L)}, \mathbf{y}^{(i)})$ 
11:    for layer  $l = L$  to 1: do
12:       $\frac{\partial Loss}{\partial \mathbb{W}^{(l)}} = \mathbf{A}^{(l-1)} \frac{\partial \mathbf{A}^{(l)}}{\partial \mathbf{Z}^{(l)}} \frac{\partial Loss}{\partial \mathbf{A}^{(L)}} \prod_{i=l+1}^L \mathbb{W}^{(i)} \frac{\partial \mathbf{A}^{(i)}}{\partial \mathbf{Z}^{(i)}}$ 
13:       $\mathbb{W}^{(l)} \leftarrow \mathbb{W}^{(l)} - \eta(t) \frac{\partial Loss}{\partial \mathbb{W}^{(l)}}$ 

```

---

We apply the fully-connected feed-forward *neural network* for regression for the Stribeck curve. The regression results and the residue distribution are shown in Fig. 8-5. They suggest a comparable performance as achieved by piece-wise multi-linear regression and random forest regression.

## 8.4 Regression for Stribeck Curve

In the field of tribology, Stribeck curve is widely used to characterize the friction coefficient as a function of Hersey number  $\text{Hr} = \mu v L / F_n$ . Based on the results from the dimensional analysis, asymptotic analysis and the experiments, we find that in the regime of boundary friction, the friction coefficient  $C_f^\perp$  is a constant about 0.22, independent of the dimensionless groups of Hersey number and pressure ratio. In the mixed regime, the friction coefficient  $C_f \sim U^{-\frac{1}{2}} P^{[-\frac{1}{4}, -1]}$ . In the regime of  $C_f \sim U^{\frac{1}{2}} P^{-\frac{1}{2}}$ . Fig. ?? shows the Stribeck curve for pressure ratio  $\gamma_p = P/E$  ranging



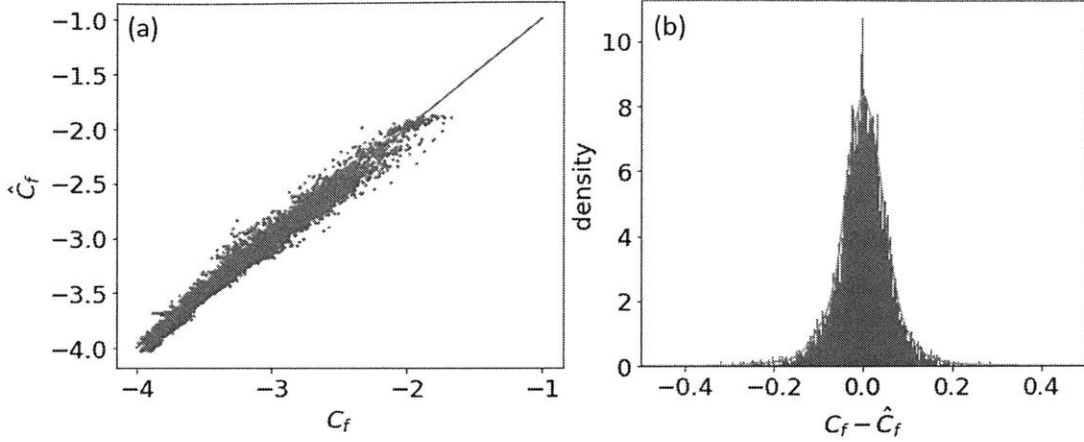


Figure 8-5: (a) Predicted friction coefficient  $\ln \hat{C}_f^{\parallel}$  versus experimental friction coefficient  $\ln C_f^{\parallel}$  using neural network regression for Hersey number ranging from  $10^{-9}$  to  $10^{-7}$ . Three dimensionless groups are taken into account:  $\mathbf{X} = [\ln \Pi_1, \ln \Pi_2, \ln \Pi_3]$ . The diagonal blue line indicates the perfect prediction of  $\ln C_f^{\parallel}$ . The  $R^2$  of this model is 0.97. (b) Probability density as a function of the residual between the prediction and experimental results of friction coefficient  $\ln C_f^{\parallel} - \ln \hat{C}_f^{\parallel}$  using linear regression for Hersey number ranging from  $10^{-9}$  to  $10^{-7}$ . The orange line indicates a kernel density estimation (KDE).

from  $10^{-5}$  to  $10^{-2}$ , where  $E$  is the Young's modulus of ice, with our model using a multi-linear regression in the logarithmic scale.

In ice hockey, the schemes of frequent intermittent skating can be categorized as hockey slide and hockey stop, the directions of which are parallel and perpendicular to the longitudinal direction of the skate blade, respectively. The corresponding Hersey number  $Hr$  for a hockey slide and a hockey stop are  $10^{-7}$  and  $10^{-11}$ , which locates at the transition from the mixed friction regime to the hydrodynamic lubrication regime and the boundary friction regime, respectively. The resultant friction coefficient in the different regimes varies one order in magnitude, in return, further verifying the adaptation of skating schemes to the physics of nature.

In addition, we compare this modified Stribeck curve to the Moody diagram and find their interesting analogy. Moody diagram relates the Darcy-Weisbach friction factor  $C_f$  to the Reynolds number  $Re$  [142, 143]. In the laminar flow regime, the friction factor  $C_f = 64/Re$ ; in the turbulent flow regime, friction factor depends on both Reynolds number  $Re$  and the roughness  $\epsilon$ . Our modified Stribeck curve

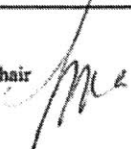
relates the friction coefficient  $C_f$  to the Hersey number  $\text{Hr}$ . In the boundary friction regime,  $C_f = 0.22$ ; in the mixed friction regime and hydrodynamic regime, the friction coefficient depends on both  $\text{Hr}$  and pressure ratio  $P/E$ , where  $E$  is the Young's modulus of ice.



## Appendix A

# Approval Letters from the MIT Committee on the Use of Humans as Experimental Subjects (COUHES)

---

**To:** Youzhi Liang  
**From:** Leigh Finn, Chair  
COUHES   
**Date:** 08/30/2017  
**Committee Action:** Exemption Granted  
**Committee Action Date:** 08/30/2017  
**COUHES Protocol #:** 1707018658  
**Study Title:** Customer Needs Identification of Sled Hockey Players

The above-referenced protocol is considered exempt after review by the Committee on the Use of Humans as Experimental Subjects pursuant to Federal regulations, 45 CFR Part 46.101(b)(2) .

This part of the federal regulations requires that the information be recorded by investigators in such a manner that subjects cannot be identified, directly or through identifiers linked to the subjects. It is necessary that the information obtained not be such that if disclosed outside the research, it could reasonably place the subjects at risk of criminal or civil liability, or be damaging to the subjects' financial standing, employability, or reputation.

If the research involves collaboration with another institution, then the research cannot commence until COUHES receives written notification of approval from the collaborating institution's IRB.

Unless informed consent is waived by the IRB, use only the most recent, IRB approved and stamped copies of the consent form(s).

**Adverse Events:** Any serious or unexpected adverse event must be reported to COUHES within 48 hours. All other adverse events should be reported in writing within 10 working days.

**Amendments:** Any changes to the protocol, including changes in experimental design, equipment, personnel or funding, must be approved by COUHES before they can be initiated, except when necessary to eliminate apparent immediate hazards to the subject.

Human subjects training is required for all study personnel and must be updated every 3 years.

You must maintain a research file for at least 3 years after completion of the study. This file should include all correspondence with COUHES, original signed consent forms, and study data.

Figure A-1: Approval letter for the study titled Customer Needs Identification of Sled Hockey Players. Exemption granted on 30-August-2017.

**MIT** Committee On the Use of Humans as  
Experimental Subjects

MASSACHUSETTS INSTITUTE OF TECHNOLOGY  
77 Massachusetts Avenue  
Cambridge, Massachusetts 02139  
Building E 25-143B  
(617) 253-6787

---

February 20, 2018

Youzhi Liang  
PhD Candidate  
Mechanical Engineering

Dear Youzhi,

We received your inquiry regarding your project titled *Test of a More Flexible Sled Hockey Stick*. Since this research does not involve human subjects as defined in the Federal Regulations 45CFR46, COUHES review is not required.

Please contact us if you have any questions.

Sincerely yours,



Leigh Fim, MD  
Chair, Committee on the Use of Humans as Experimental Subjects (COUHES)

LF/mk

Figure A-2: Non HSR letter for the study titled Test of a More Flexible Sled Hockey Stick. Exemption granted on 20-Feb-2017.

**MIT** Committee On the Use of Humans as  
Experimental Subjects

MASSACHUSETTS INSTITUTE OF TECHNOLOGY  
77 Massachusetts Avenue  
Cambridge, Massachusetts 02139  
Building E 25-143B  
(617) 253-6787

---

March 22, 2018

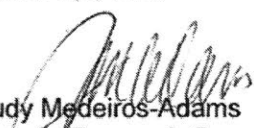
Youzhi Liang  
PhD Candidate  
Mechanical Engineering

Dear Youzhi,

We received your inquiry regarding your project titled Test of a more Flexible Sled Hockey Stick. Since this research does not involve human subjects as defined in the Federal Regulations 45CFR46, COUHES review is not required.

Please contact us if you have any questions.

Sincerely yours,

  
Judy Medeiros-Adams  
Human Research Compliance Administrator, Committee on the Use of Humans as  
Experimental Subjects (COUHES)

JM/mk

Figure A-3: Non HSR letter for the study titled Test of a More Flexible Sled Hockey Stick. Exemption granted on 22-March-2017.

# Appendix B

## Figures for Experimental Results in the Regime of Boundary Friction



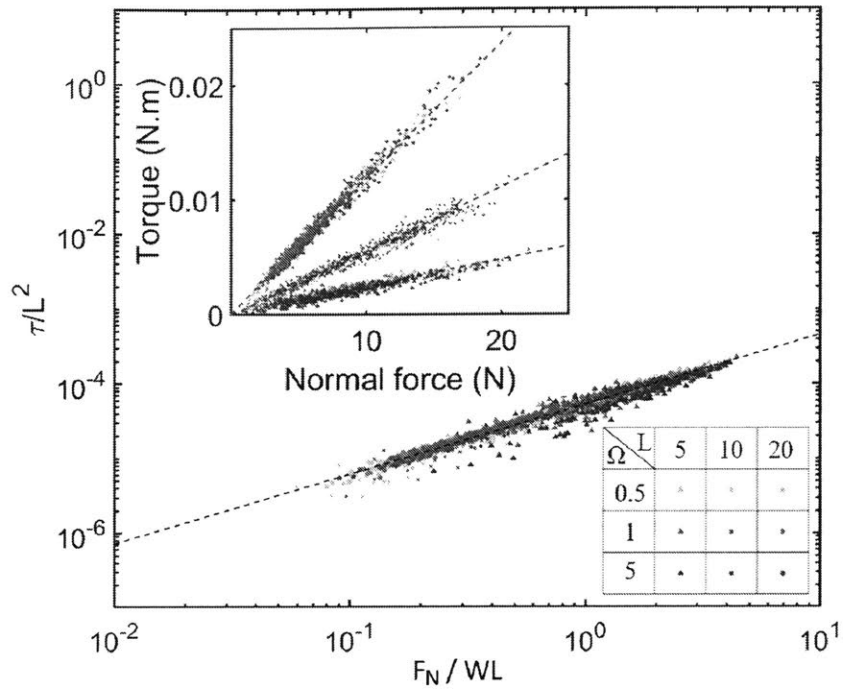


Figure B-1:  $\tau/L^2$  versus  $F_N/WL$  for thickness  $W = 0.4064\text{mm}$ . (Inset) Torque ( $\text{N}\cdot\text{m}$ ) as a function of normal force (N) for three lengths,  $L$  (mm) and for three angular velocities,  $\Omega$  (rad/s). Dashed lines are linear regression lines.

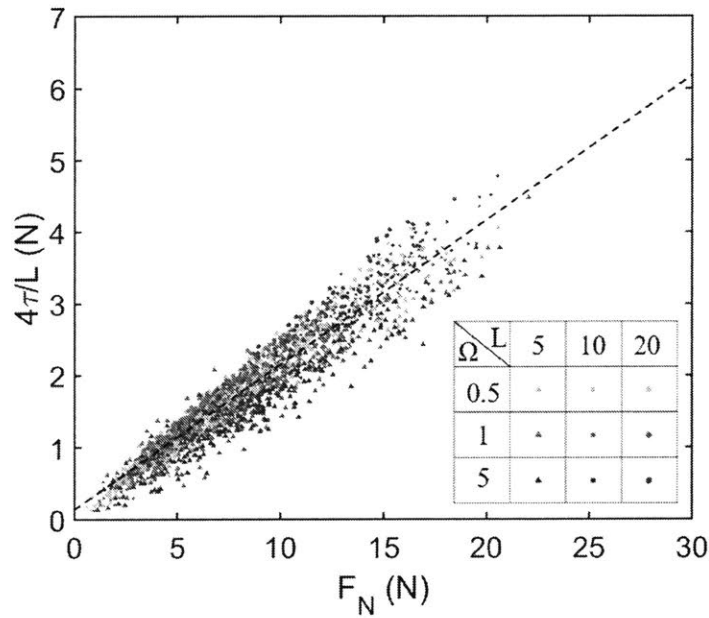


Figure B-2:  $4\tau/L(N)$  versus  $F_N(N)$  for thickness  $W = 0.4064\text{mm}$  for three lengths,  $L$  (mm) and for three angular velocities,  $\Omega$  (rad/s). Dashed lines are linear regression lines. The slope of the linear regression line is  $0.22 \pm 0.03$ .

## Appendix C

# Figures for Experimental Results and Models in the Regime of Mixed Friction and Hydrodynamic Lubrication

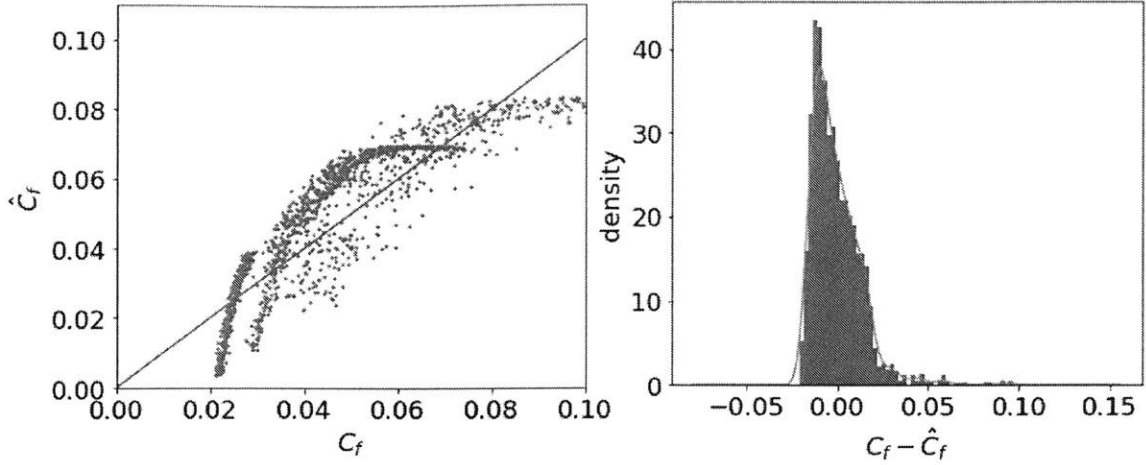


Figure C-1: (a) Predicted friction coefficient  $\hat{C}_f^{\parallel}$  versus experimental friction coefficient  $C_f^{\parallel}$  using multi-linear regression for Hersey number ranging from  $10^{-9}$  to  $10^{-7}$ .  $\mathbf{X} = [\mathbf{L}, \mathbf{W}, \mathbf{U}, \mathbf{F}, \mathbf{\Pi}_1, \mathbf{\Pi}_2, \mathbf{\Pi}_3]$ . The diagonal blue line indicates the perfect prediction of  $C_f$ . The  $R^2$  of the model is 0.68. (b) Probability density as a function of the residual between the prediction and experimental results of friction coefficient  $C_f^{\parallel} - \hat{C}_f^{\parallel}$  using linear regression for Hersey number ranging from  $10^{-9}$  to  $10^{-7}$ . The orange line indicates a kernel density estimation (KDE). The standard deviation of the residual is 0.015.

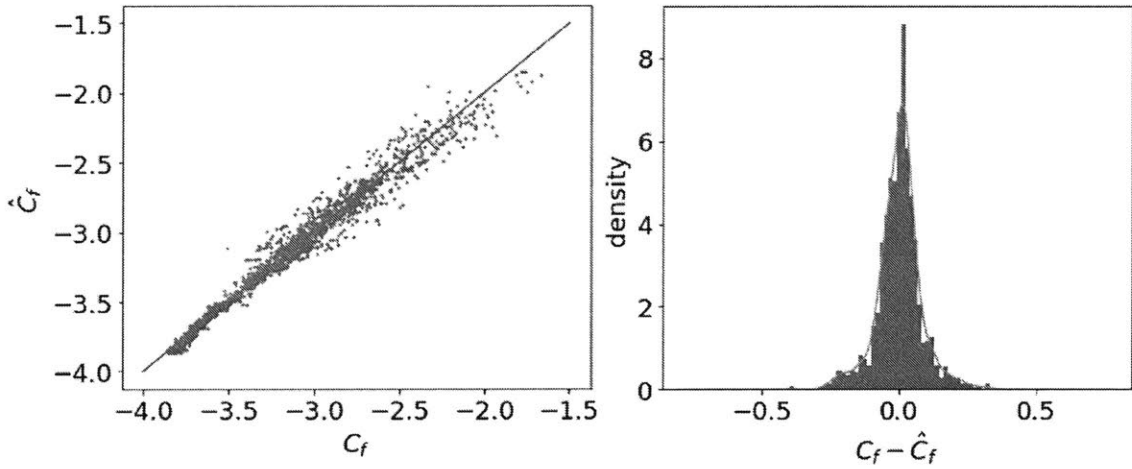


Figure C-2: (a) Predicted friction coefficient  $\hat{C}_f^{\parallel}$  versus experimental friction coefficient  $C_f^{\parallel}$  using multi-linear regression for Hersey number ranging from  $10^{-9}$  to  $10^{-7}$ .  $\mathbf{X} = [\ln \mathbf{L}, \ln \mathbf{W}, \ln \mathbf{U}, \ln \mathbf{F}, \ln \mathbf{\Pi}_1, \ln \mathbf{\Pi}_2, \ln \mathbf{\Pi}_3]$ . The diagonal blue line indicates the perfect prediction of  $C_f$ . The  $R^2$  of the model is 0.97. (b) Probability density as a function of the residual between the prediction and experimental results of friction coefficient  $C_f^{\parallel} - \hat{C}_f^{\parallel}$  using linear regression for Hersey number ranging from  $10^{-9}$  to  $10^{-7}$ . The orange line indicates a kernel density estimation (KDE). The standard deviation of the residual is 0.08.

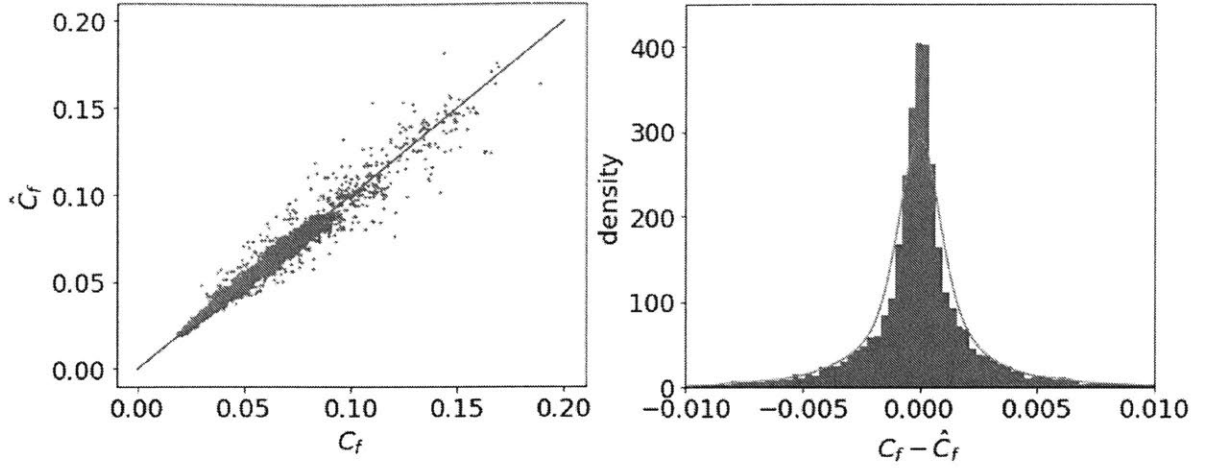


Figure C-3: (a) Predicted friction coefficient  $\hat{C}_f^{\parallel}$  versus experimental friction coefficient  $C_f^{\parallel}$  using random forest regression for Hersey number ranging from  $10^{-9}$  to  $10^{-7}$ .  $\mathbf{X} = [\mathbf{L}, \mathbf{W}, \mathbf{U}, \mathbf{F}, \mathbf{\Pi}_1, \mathbf{\Pi}_2, \mathbf{\Pi}_3]$ . The diagonal blue line indicates the perfect prediction of  $C_f$ . The  $R^2$  of the model is 0.975. (b) Probability density as a function of the residual between the prediction and experimental results of friction coefficient  $C_f^{\parallel} - \hat{C}_f^{\parallel}$  using linear regression for Hersey number ranging from  $10^{-9}$  to  $10^{-7}$ . The orange line indicates a kernel density estimation (KDE).

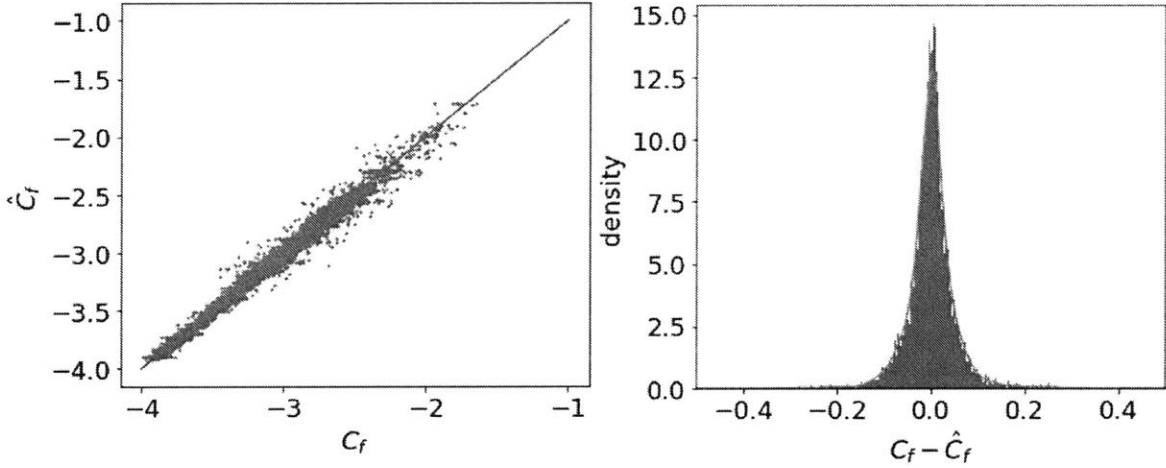


Figure C-4: (a) Predicted friction coefficient  $\hat{C}_f^{\parallel}$  versus experimental friction coefficient  $C_f^{\parallel}$  using random forest regression for Hersey number ranging from  $10^{-9}$  to  $10^{-7}$ .  $\mathbf{X} = [\ln \mathbf{L}, \ln \mathbf{W}, \ln \mathbf{U}, \ln \mathbf{F}, \ln \mathbf{\Pi}_1, \ln \mathbf{\Pi}_2, \ln \mathbf{\Pi}_3]$ . The diagonal blue line indicates the perfect prediction of  $C_f$ . The  $R^2$  of the model is 0.987. (b) Probability density as a function of the residual between the prediction and experimental results of friction coefficient  $C_f^{\parallel} - \hat{C}_f^{\parallel}$  using linear regression for Hersey number ranging from  $10^{-9}$  to  $10^{-7}$ . The orange line indicates a kernel density estimation (KDE).



# Bibliography

- [1] <http://www.wfsledrangers.org/>.
- [2] JT Worobets, JC Fairbairn, and DJ Stefanyshyn. The influence of shaft stiffness on potential energy and puck speed during wrist and slap shots in ice hockey. *Sports Engineering*, 9(4):191–200, 2006.
- [3] DJ Pearsall, DL Montgomery, N Rothsching, and RA Turcotte. The influence of stick stiffness on the performance of ice hockey slap shots. *Sports engineering*, 2(3):3–12, 1999.
- [4] Xianfeng Gu and Shing-Tung Yau. Global conformal surface parameterization. In *Proceedings of the 2003 Eurographics/ACM SIGGRAPH symposium on Geometry processing*, pages 127–137. Eurographics Association, 2003.
- [5] Jan Sokolowski and Jean-Paul Zolésio. Introduction to shape optimization. In *Introduction to Shape Optimization*, pages 5–12. Springer, 1992.
- [6] Mitchell M Tseng, Jianxin Jiao, and M Eugene Merchant. Design for mass customization. *CIRP annals*, 45(1):153–156, 1996.
- [7] George David Birkhoff. *Dynamical systems*, volume 9. American Mathematical Soc., 1927.
- [8] Rafal Goebel, Ricardo G Sanfelice, and Andrew R Teel. Hybrid dynamical systems. *IEEE control systems magazine*, 29(2):28–93, 2009.
- [9] Lawrence Perko. *Differential equations and dynamical systems*, volume 7. Springer Science & Business Media, 2013.
- [10] David L Montgomery. Physiology of ice hockey. *Sports medicine*, 5(2):99–126, 1988.
- [11] Peter Soberlak and Jean Cote. The developmental activities of elite ice hockey players. *Journal of applied sport psychology*, 15(1):41–49, 2003.
- [12] Michael H Cox, Daniel S Miles, Tony J Verde, and Edward C Rhodes. Applied physiology of ice hockey. *Sports medicine*, 19(3):184–201, 1995.

- [13] Kyle Flik, Stephen Lyman, and Robert G Marx. American collegiate men's ice hockey: an analysis of injuries. *The American journal of sports medicine*, 33(2):183–189, 2005.
- [14] HI Green, P Bishop, M Houston, R McKillop, R Norman, and P Stothart. Time-motion and physiological assessments of ice hockey performance. *Journal of Applied Physiology*, 40(2):159–163, 1976.
- [15] Ashley D Zapf and Joan P Joyce. Ice sled hockey (sledge hockey outside the united states). In *Adaptive Sports Medicine*, pages 245–249. Springer, 2018.
- [16] PETER RIMMER. 2014 paralympics. sled hockey: Thrills, spills, and excitement. *Palaestra*, 28(2), 2014.
- [17] Ashley D Zapf and Joan P Joyce. Ice sled hockey (sledge hockey. *Adaptive Sports Medicine: A Clinical Guide*, page 245, 2017.
- [18] Peter Rimmer. Sled hockey: thrills, spills, and excitement. *Palaestra*, 28(2):26–29, 2014.
- [19] Lauren C Miga. *Sled hockey as an occupation for children with mobility impairments: The meaning of participation from the perspectives of fathers*. PhD thesis, D'Youville College, 2009.
- [20] Sean Busse. Eligibility and classification in paralympic sports. *Palaestra*, 28(2):20–24, 2014.
- [21] Justin Bechstein. Evaluation and product design improvement of the adaptive sport of sled hockey, 2014.
- [22] Lai-Kow Chan and Ming-Lu Wu. Quality function deployment: A literature review. *European journal of operational research*, 143(3):463–497, 2002.
- [23] M Anthony and A Dirik. Simplified quality function deployment for high-technology product development. *Visions*, 4(2):9–12, 1995.
- [24] Ian D Bier and Robert Cornesky. Using qfd to construct a higher education curriculum. *Quality progress*, 34(4):64, 2001.
- [25] LJ Kwon and SW Han. Development of the economical reliability test method of using quality function deployment. In *Proceedings of the Electronic Circuits World Convention*, volume 8, pages 7–10, 1999.
- [26] William D Barnett and MK Raja. Application of qfd to the software development process. *International Journal of Quality & Reliability Management*, 12(6):24–42, 1995.
- [27] N Stubbs and M Diaz. Impact of qfd utilization in the development of a non-destructive damage detection system for aerospace structures. *International Journal of Materials and Product Technology*, 9(1-3):3–22, 1994.

- [28] Anne-Marie Kietzig, Savvas G Hatzikiriakos, and Peter Englezos. Physics of ice friction. *Journal of Applied Physics*, 107(8):4, 2010.
- [29] Kiran Singh, Sébastien Michelin, and Emmanuel De Langre. The effect of non-uniform damping on flutter in axial flow and energy-harvesting strategies. *Proceedings of the Royal Society A: Mathematical, Physical and Engineering Sciences*, 468(2147):3620–3635, 2012.
- [30] Carl T Kelley. *Solving nonlinear equations with Newton’s method*, volume 1. Siam, 2003.
- [31] Charles G Broyden. A class of methods for solving nonlinear simultaneous equations. *Mathematics of computation*, 19(92):577–593, 1965.
- [32] Dana A Knoll and David E Keyes. Jacobian-free newton–krylov methods: a survey of approaches and applications. *Journal of Computational Physics*, 193(2):357–397, 2004.
- [33] Ying Chen and Chen Shen. A jacobian-free newton-gmres (m) method with adaptive preconditioner and its application for power flow calculations. *IEEE Transactions on Power Systems*, 21(3):1096–1103, 2006.
- [34] Dana A Knoll, VA Mousseau, Luis Chacón, and J Reisner. Jacobian-free newton-krylov methods for the accurate time integration of stiff wave systems. *Journal of Scientific Computing*, 25(1-2):213–230, 2005.
- [35] David G Luenberger. The conjugate residual method for constrained minimization problems. *SIAM Journal on Numerical Analysis*, 7(3):390–398, 1970.
- [36] Luiz Mariano Carvalho, Serge Gratton, Rafael Lago, and Xavier Vasseur. A flexible generalized conjugate residual method with inner orthogonalization and deflated restarting. *SIAM Journal on Matrix Analysis and Applications*, 32(4):1212–1235, 2011.
- [37] William C Skamarock, Piotr K Smolarkiewicz, and Joseph B Klemp. Preconditioned conjugate-residual solvers for helmholtz equations in nonhydrostatic models. *Monthly weather review*, 125(4):587–599, 1997.
- [38] Michael G Safonov and RY Chiang. A schur method for balanced-truncation model reduction. *IEEE Transactions on Automatic Control*, 34(7):729–733, 1989.
- [39] Payam Rabiei and Massoud Pedram. Model order reduction of large circuits using balanced truncation. In *Proceedings of the ASP-DAC’99 Asia and South Pacific Design Automation Conference 1999 (Cat. No. 99EX198)*, pages 237–240. IEEE, 1999.



- [40] Joel R Phillips, Luca Daniel, and Luis Miguel Silveira. Guaranteed passive balancing transformations for model order reduction. *IEEE Transactions on Computer-Aided Design of Integrated Circuits and Systems*, 22(8):1027–1041, 2003.
- [41] Timo Reis and Tatjana Stykel. Balanced truncation model reduction of second-order systems. *Mathematical and Computer Modelling of Dynamical Systems*, 14(5):391–406, 2008.
- [42] Ulrike Baur, Peter Benner, and Lihong Feng. Model order reduction for linear and nonlinear systems: a system-theoretic perspective. *Archives of Computational Methods in Engineering*, 21(4):331–358, 2014.
- [43] Peter Benner and André Schneider. Balanced truncation model order reduction for lti systems with many inputs or outputs. In *Proceedings of the 19th international symposium on mathematical theory of networks and systems–MTNS*, volume 5, 2010.
- [44] Qingjian Yu, Janet Meiling L Wang, and Ernest S Kuh. Passive multipoint moment matching model order reduction algorithm on multiport distributed interconnect networks. *IEEE Transactions on Circuits and Systems I: Fundamental Theory and Applications*, 46(1):140–160, 1999.
- [45] Luca Daniel, Ong Chin Siong, Low Sok Chay, Kwok Hong Lee, and Jacob White. A multiparameter moment-matching model-reduction approach for generating geometrically parameterized interconnect performance models. *IEEE Transactions on Computer-Aided Design of Integrated Circuits and Systems*, 23(5):678–693, 2004.
- [46] Peter Benner and Lihong Feng. A robust algorithm for parametric model order reduction based on implicit moment matching. In *Reduced order methods for modeling and computational reduction*, pages 159–185. Springer, 2014.
- [47] Lihong Feng, Jan G Korvink, and Peter Benner. A fully adaptive scheme for model order reduction based on moment matching. *IEEE Transactions on Components, Packaging and Manufacturing Technology*, 5(12):1872–1884, 2015.
- [48] Zhenfei Song, Donglin Su, Fabrice Duval, and Anne Louis. Model order reduction for peec modeling based on moment matching. *Progress In Electromagnetics Research*, 114:285–299, 2011.
- [49] Janet Meiling Wang, Chia-Chi Chu, Qingjian Yu, and Ernest S Kuh. On projection-based algorithms for model-order reduction of interconnects. *IEEE Transactions on Circuits and Systems I: Fundamental Theory and Applications*, 49(11):1563–1585, 2002.

- [50] John F Alexander, James B Haddow, and Gerald A Schultz. Comparison of the ice hockey wrist and slap shots for speed and accuracy. *Research Quarterly. American Association for Health, Physical Education and Recreation*, 34(3):259–266, 1963.
- [51] T-C Wu, D Pearsall, A Hodges, R Turcotte, R Lefebvre, D Montgomery, and H Bateni. The performance of the ice hockey slap and wrist shots: the effects of stick construction and player skill. *Sports Engineering*, 6(1):31–39, 2003.
- [52] A Villaseñor, RA Turcotte, and DJ Pearsall. Recoil effect of the ice hockey stick during a slap shot. *Journal of applied biomechanics*, 22(3):202–211, 2006.
- [53] Etienne Simard, Eric Roy, Genevieve Martin, Hugo Cantin, and Rene Therrien. Static and dynamic characteristics of composite one-piece hockey sticks. In *ISBS-Conference Proceedings Archive*, number 4, 2004.
- [54] <http://www.nhl.com/>.
- [55] Justin Berthold, Brad E Dicianno, and Rory A Cooper. Pressure mapping to assess seated pressure distributions and the potential risk for skin ulceration in a population of sledge hockey players and control subjects. *Disability and Rehabilitation: Assistive Technology*, 8(5):387–391, 2013.
- [56] Timothy Woo, Jonathan Loh, Rene Turcotte, and David Pearsall. The ice hockey slap shot, elite versus recreational. In *ISBS-Conference Proceedings Archive*, number 11, 2004.
- [57] Ayhan Goktepe, Isil Ozfidan, Hakan Karabork, and Feza Korkusuz. Elbow but not knee joint kinematics can be assessed using photogrammetric methods during a non-stationary slap shot in ice hockey. *Scientific Research and Essays*, 5(3):339–342, 2010.
- [58] Ryan J Frayne, Rebecca B Dean, and Thomas R Jenkyn. Improving ice hockey slap shot analysis using three-dimensional optical motion capture: A pilot study determining the effects of a novel grip tape on slap shot performance. *Proceedings of the Institution of Mechanical Engineers, Part P: Journal of Sports Engineering and Technology*, 229(2):136–144, 2015.
- [59] Michael Hardegger, Benjamin Ledergerber, Severin Mutter, Christian Vogt, Julia Seiter, Alberto Calatroni, and Gerhard Tröster. Sensor technology for ice hockey and skating. In *2015 IEEE 12th International Conference on Wearable and Implantable Body Sensor Networks (BSN)*, number 14, pages 1–6. IEEE, 2015.
- [60] KV Lomond, RA Turcotte, and DJ Pearsall. Three-dimensional analysis of blade contact in an ice hockey slap shot, in relation to player skill. *Sports Engineering*, 10(2):87–100, 2007.

- [61] Earl F Hoerner. The dynamic role played by the ice hockey stick. In *Safety in ice hockey*, number 16. ASTM International, 1989.
- [62] RA Turcotte, P Renaud, and DJ Pearsall. Ice hockey skate, stick design and performance measures. In *The Engineering Approach to Winter Sports*, number 17, pages 311–326. Springer, 2016.
- [63] Ronny Lorentzon, Hans Wedrèn, and Tom Pietilä. Incidence, nature, and causes of ice hockey injuries: a three-year prospective study of a swedish elite ice hockey team. *The American Journal of Sports Medicine*, 16(4):392–396, 1988.
- [64] Brendan Kays and Lloyd Smith. Numerical simulation of the ice hockey slap shot. *Procedia Engineering*, 112(19):22–27, 2015.
- [65] Brendan T Kays and Lloyd V Smith. Effect of ice hockey stick stiffness on performance. *Sports Engineering*, 20(4):245–254, 2017.
- [66] Maxine Kwan, Michael Skipper Andersen, Mark de Zee, and John Rasmussen. Dynamic model of a badminton stroke (p254). In *The Engineering of Sport 7*, number 21, pages 563–571. Springer, 2009.
- [67] Michael Phomsoupha, Guillaume Laffaye, Caroline Cohen, and Christophe Clanet. How to use the elasticity of a badminton racket to increase its speed by 80%? *Computer methods in biomechanics and biomedical engineering*, 18(sup1):2028–2029, 2015.
- [68] Alan M Nathan. Dynamics of the baseball–bat collision. *American Journal of Physics*, 68(11):979–990, 2000.
- [69] LL Van Zandt. The dynamical theory of the baseball bat. *American Journal of Physics*, 60(2):172–181, 1992.
- [70] Howard Brody. Models of baseball bats. *American Journal of Physics*, 58(8):756–758, 1990.
- [71] Donald C Leigh and Wei-Yang Lu. Dynamics of the interactions between ball, strings, and racket in tennis. *Journal of Applied Biomechanics*, 8(3):181–206, 1992.
- [72] M Brannigan and S Adali. Mathematical modelling and simulation of a tennis racket. *Medicine and science in sports and exercise*, 13(1):44–53, 1981.
- [73] Howard Brody. Physics of the tennis racket. *American Journal of physics*, 47(6):482–487, 1979.
- [74] Howard Brody. Vibration damping of tennis rackets. *Journal of Applied Biomechanics*, 5(4):451–456, 1989.

- [75] Herbert Hatze. Impact probability distribution, sweet spot, and the concept of an effective power region in tennis rackets. *Journal of Applied Biomechanics*, 10(1):43–50, 1994.
- [76] Salah Faik and Holly Witteman. Modeling of impact dynamics: A literature survey. In *2000 International ADAMS User Conference*, volume 80. Citeseer, 2000.
- [77] Anindya Chatterjee. The short-time impulse response of euler-bernoulli beams. *Journal of applied mechanics*, 71(2):208–218, 2004.
- [78] Giuseppe Piccardo and Federica Tubino. Dynamic response of euler-bernoulli beams to resonant harmonic moving loads. *Structural Engineering and Mechanics*, 44(5):681–704, 2012.
- [79] JB Yang, LJ Jiang, and D Ch Chen. Dynamic modelling and control of a rotating euler-bernoulli beam. *Journal of sound and vibration*, 274(3-5):863–875, 2004.
- [80] S Hanagud and S Sarkar. Problem of the dynamics of a cantilevered beam attached to a moving base. *Journal of Guidance, Control, and Dynamics*, 12(3):438–441, 1989.
- [81] WD Zhu and CD Mote. Dynamic modeling and optimal control of rotating euler-bernoulli beams. In *Proceedings of the 1997 American Control Conference (Cat. No. 97CH36041)*, volume 5, pages 3110–3114. IEEE, 1997.
- [82] J Cl Simo and L Vu-Quoc. On the dynamics of flexible beams under large overall motions—the plane case: Part ii. *Journal of applied mechanics*, 53(4):855–863, 1986.
- [83] YA Khulief. Vibration frequencies of a rotating tapered beam with end mass. *Journal of Sound and Vibration*, 134(1):87–97, 1989.
- [84] JC Simo and L Vu-Quoc. The role of non-linear theories in transient dynamic analysis of flexible structures. *Journal of Sound and Vibration*, 119(3):487–508, 1987.
- [85] SV Hoa. Vibration of a rotating beam with tip mass. *Journal of sound and vibration*, 67(3):369–381, 1979.
- [86] S Putter and H Manor. Natural frequencies of radial rotating beams. *Journal of Sound and Vibration*, 56(2):175–185, 1978.
- [87] A Yigit, RA Scott, and A Galip Ulsoy. Flexural motion of a radially rotating beam attached to a rigid body. *Journal of Sound and Vibration*, 121(2):201–210, 1988.

- [88] Rod Cross. Impact of a ball with a bat or racket. *American Journal of Physics*, 67(8):692–702, 1999.
- [89] <https://www.paralympic.org/ice-hockey>.
- [90] Mikhail Goman and Alexander Khrabrov. State-space representation of aerodynamic characteristics of an aircraft at high angles of attack. *Journal of Aircraft*, 31(5):1109–1115, 1994.
- [91] Peter G Hamel and Ravindra V Jategaonkar. Evolution of flight vehicle system identification. *Journal of aircraft*, 33(1):9–28, 1996.
- [92] Jon H Davis. State space realizations. In *Foundations of Deterministic and Stochastic Control*, pages 1–69. Springer, 2002.
- [93] Michel Verhaegen and Patrick Dewilde. Subspace model identification part 2. analysis of the elementary output-error state-space model identification algorithm. *International journal of control*, 56(5):1211–1241, 1992.
- [94] Hong Zhao, John Guiver, and Guillermo Sentoni. An identification approach to nonlinear state space model for industrial multivariable model predictive control. In *Proceedings of the 1998 American Control Conference. ACC (IEEE Cat. No. 98CH36207)*, volume 2, pages 796–800. IEEE, 1998.
- [95] H-F Raynaud and A Zergainoh. State-space representation for fractional order controllers. *Automatica*, 36(7):1017–1021, 2000.
- [96] Mats Viberg. Subspace methods in system identification. *IFAC Proceedings Volumes*, 27(8):1–12, 1994.
- [97] Mordechai Karpel. Design for active flutter suppression and gust alleviation using state-space aeroelastic modeling. *Journal of Aircraft*, 19(3):221–227, 1982.
- [98] C Cohen, B Darbois Texier, G Laffaye, L Auvray, and C Clanet. Weightlifting and the actomyosin cycle. *Proceedings of the Royal Society A: Mathematical, Physical and Engineering Sciences*, 471(2184):20150473, 2015.
- [99] Ahmet Erdemir, Scott McLean, Walter Herzog, and Antonie J van den Bogert. Model-based estimation of muscle forces exerted during movements. *Clinical biomechanics*, 22(2):131–154, 2007.
- [100] John Halling. *Principles of tribology*. Macmillan International Higher Education, 1978.
- [101] John A Schey and MC Shaw. *Tribology in metalworking: friction, lubrication and wear*, 1984.
- [102] Gwidon Stachowiak and Andrew W Batchelor. *Engineering tribology*. Butterworth-Heinemann, 2013.

- [103] Bharat Bhushan. *Introduction to tribology*. John Wiley & Sons, 2013.
- [104] Irina Georgievna Goryacheva. *Contact mechanics in tribology*, volume 61. Springer Science & Business Media, 2013.
- [105] Robert Rosenberg. Why is ice slippery? *Physics Today*, 58(12):50, 2005.
- [106] Victor F Petrenko and Robert W Whitworth. *Physics of ice*. OUP Oxford, 1999.
- [107] M Faraday. Philos mag. *Philos Mag*, 17(113):162–169, 1859.
- [108] NH Fletcher. Surface structure of water and ice. *Philosophical Magazine*, 7(74):255–269, 1962.
- [109] T Kobayashi. The growth of snow crystals at low supersaturations. *Philosophical Magazine*, 6(71):1363–1370, 1961.
- [110] JG Dash, Haiying Fu, and JS Wettlaufer. The premelting of ice and its environmental consequences. *Reports on Progress in Physics*, 58(1):115, 1995.
- [111] Charles A Knight. Experiments on the contact angle of water on ice. *Philosophical magazine*, 23(181):153–165, 1971.
- [112] Lasse Makkonen. Surface melting of ice. *The Journal of Physical Chemistry B*, 101(32):6196–6200, 1997.
- [113] Geert-Jan Kroes. Surface melting of the (0001) face of tip4p ice. *Surface Science*, 275(3):365–382, 1992.
- [114] Samuel C Colbeck. Pressure melting and ice skating. *American Journal of Physics*, 63(10):888–890, 1995.
- [115] Eric Schwegler, Manu Sharma, François Gygi, and Giulia Galli. Melting of ice under pressure. *Proceedings of the National Academy of Sciences*, 105(39):14779–14783, 2008.
- [116] Thomas A Weber and Frank H Stillinger. Pressure melting of ice. *The Journal of chemical physics*, 80(1):438–443, 1984.
- [117] LD Drake and RL Shreve. Pressure melting and regelation of ice by round wires. *Proceedings of the Royal Society of London. A. Mathematical and Physical Sciences*, 332(1588):51–83, 1973.
- [118] Lasse Makkonen and Maria Tikanmäki. Modeling the friction of ice. *Cold Regions Science and Technology*, 102:84–93, 2014.
- [119] Allan Mills. The coefficient of friction, particularly of ice. *Physics Education*, 43(4):392, 2008.

- [120] Xiaobin Lu, MM Khonsari, and ERM Gelinck. The stribeck curve: experimental results and theoretical prediction. *Journal of tribology*, 128(4):789–794, 2006.
- [121] Yansong Wang, Q Jane Wang, Chih Lin, and Fanghui Shi. Development of a set of stribeck curves for conformal contacts of rough surfaces. *Tribology transactions*, 49(4):526–535, 2006.
- [122] Kristof Vanclooster, Stepan Vladimirovitch Lomov, and Ignace Verpoest. Simulation of multi-layered composites forming. *International Journal of Material Forming*, 3(1):695–698, 2010.
- [123] Dan Pavelescu and Andrei Tudor. The sliding friction coefficient—its evolution and usefulness. *Wear*, 120(3):321–336, 1987.
- [124] DP Hess and A Soom. Friction at a lubricated line contact operating at oscillating sliding velocities. *Journal of tribology*, 112(1):147–152, 1990.
- [125] AD Roberts and JC Richardson. Interface study of rubber-ice friction. *Wear*, 67(1):55–69, 1981.
- [126] Daniel D Higgins, Brett A Marmo, Christopher E Jeffree, Vasileios Koutsos, and Jane R Blackford. Morphology of ice wear from rubber–ice friction tests and its dependence on temperature and sliding velocity. *Wear*, 265(5-6):634–644, 2008.
- [127] M Akkok, CM Ettles, and SJ Calabrese. Parameters affecting the kinetic friction of ice. *Journal of Tribology*, 109(3):552–559, 1987.
- [128] B Pansu, R Dandoloﬀ, and E Dubois-Violette. The double twist connection and the s3 blue phase. *Journal de Physique*, 48(2):297–304, 1987.
- [129] Brett A Marmo, Jane R Blackford, and Chris E Jeffree. Ice friction, wear features and their dependence on sliding velocity and temperature. *Journal of Glaciology*, 51(174):391–398, 2005.
- [130] L Bäurle, D Szabó, M Fauve, H Rhyner, and ND Spencer. Sliding friction of polyethylene on ice: tribometer measurements. *Tribology Letters*, 24(1):77–84, 2006.
- [131] Jos J de Koning, JHP Houdijk, Gert de Groot, and Maarten F Bobbert. From biomechanical theory to application in top sports: the klapskate story. *Journal of Biomechanics*, 33:1225–1229, 2000.
- [132] Anne-Marie Kietzig, Savvas G Hatzikiriakos, and Peter Englezos. Ice friction: the effects of surface roughness, structure, and hydrophobicity. *Journal of Applied Physics*, 106(2):024303, 2009.
- [133] Frank Philip Bowden and TP Hughes. The mechanism of sliding on ice and snow. *Proceedings of the Royal Society of London. Series A. Mathematical and Physical Sciences*, 172(949):280–298, 1939.

- [134] L Bäurle, Th U Kaempfer, D Szabo, and ND Spencer. Sliding friction of polyethylene on snow and ice: contact area and modeling. *Cold Regions Science and Technology*, 47(3):276–289, 2007.
- [135] DCB Evans, John Frederick Nye, and KJ Cheeseman. The kinetic friction of ice. *Proceedings of the Royal Society of London. A. Mathematical and Physical Sciences*, 347(1651):493–512, 1976.
- [136] Pekka Oksanen and Juhani Keinonen. The mechanism of friction of ice. *Wear*, 78(3):315–324, 1982.
- [137] KL Johnson. Regimes of elastohydrodynamic lubrication. *Journal of Mechanical Engineering Science*, 12(1):9–16, 1970.
- [138] D Dowson. Elastohydrodynamic and micro-elastohydrodynamic lubrication. *Wear*, 190(2):125–138, 1995.
- [139] R Gohar and A Cameron. The mapping of elastohydrodynamic contacts. *ASLE TRANSACTIONS*, 10(3):215–225, 1967.
- [140] Osborne Reynolds. Iv. on the theory of lubrication and its application to mr. beauchamp tower’s experiments, including an experimental determination of the viscosity of olive oil. *Philosophical transactions of the Royal Society of London*, (177):157–234, 1886.
- [141] Yang Peiran and Wen Shizhu. A generalized reynolds equation for non-newtonian thermal elastohydrodynamic lubrication. *Journal of tribology*, 112(4):631–636, 1990.
- [142] DF Elger, BC Williams, CT Crowe, and JA Roberson. Engineering fluid mechanics. *Energy*, 2:03–01, 2013.
- [143] Marc LaViolette. On the history, science, and technology included in the moody diagram. *Journal of Fluids Engineering*, 139(3):030801, 2017.
- [144] Geoffrey J McLachlan and Kaye E Basford. *Mixture models: Inference and applications to clustering*, volume 38. M. Dekker New York, 1988.
- [145] Zeyu Bai, Ruizhi Yang, and Youzhi Liang. Mental task classification using electroencephalogram signal. *arXiv preprint arXiv:1910.03023*, 2019.
- [146] Arturo Chavez, Dimitris Koutentakis, Youzhi Liang, Sonali Tripathy, and Jie Yun. Identify statistical similarities and differences between the deadliest cancer types through gene expression. *arXiv preprint arXiv:1903.07847*, 2019.
- [147] Rui Xu and Don Wunsch. *Clustering*, volume 10. John Wiley & Sons, 2008.
- [148] Satu Elisa Schaeffer. Graph clustering. *Computer science review*, 1(1):27–64, 2007.



- [149] Yuk Lai Suen, Prem Melville, and Raymond J Mooney. Combining bias and variance reduction techniques for regression trees. In *European Conference on Machine Learning*, pages 741–749. Springer, 2005.
- [150] Yasser Ganjisaffar, Rich Caruana, and Cristina Videira Lopes. Bagging gradient-boosted trees for high precision, low variance ranking models. In *Proceedings of the 34th international ACM SIGIR conference on Research and development in Information Retrieval*, pages 85–94. ACM, 2011.
- [151] Thomas G Dietterich. Ensemble methods in machine learning. In *International workshop on multiple classifier systems*, pages 1–15. Springer, 2000.
- [152] Xavier Glorot and Yoshua Bengio. Understanding the difficulty of training deep feedforward neural networks. In *Proceedings of the thirteenth international conference on artificial intelligence and statistics*, pages 249–256, 2010.